Dynamic and static charging processes of single molecules

A scanning probe study

Dissertation
zur Erlangung des Doktorgrades
der Naturwissenschaften (Dr. rer. nat.)
der Fakultät für Physik
der Universität Regensburg

vorgelegt von

Nemanja Kocić

Februar 2017

Die Arbeit wurde von Prof. Dr. Jascha Repp angeleitet.
Das Promotionsgesuch wurde am 6. Juli 2016 eingereicht.

Prüfungsausschuss:	Vorsitzender:	PD Dr. Meinulf Göckeler
	1. Gutachter:	Prof. Dr. Jascha Repp
	2. Gutachter:	Prof. Dr. Christian Schüller
	weiterer Prüfer:	Prof. Dr. Sergey Ganichev

To Julijana

Contents

1 Theoretical background **1**
- 1.1 Scanning Tunneling Microscopy . . . 2
  - 1.1.1 Imaging modes . . . 6
- 1.2 Double barrier tunneling junction . . . 7
- 1.3 Coulomb blockade . . . 9
- 1.4 Atomic force microscopy . . . 10
  - 1.4.1 Dynamic AFM . . . 12
  - 1.4.2 Forces in AFM . . . 16
  - 1.4.3 Kelvin probe force microscopy . . . 19

2 Experimental setup and methods **23**
- 2.1 LT-UHV STM/AFM apparatus . . . 23
- 2.2 LT-SPM head . . . 24
- 2.3 qPlus sensor . . . 26
- 2.4 Metal substrates . . . 27
- 2.5 Ultrathin insulating films . . . 30
- 2.6 Manipulation of adsorbates . . . 32
- 2.7 Tip functionalization . . . 33

3 Apparent reversal of molecular orbitals reveals entanglement **35**
- 3.1 Introduction . . . 35
- 3.2 On the number of nodes of wave functions . . . 37
- 3.3 Methods . . . 39
- 3.4 Engineering electronic structure of a molecular wire . . . 40
- 3.5 Reversal of the molecular orbital sequence . . . 42
- 3.6 Failure of a single-particle picture description . . . 46

3.7 Basics of many-body theory 47
3.8 The entanglement of the two particle ground state . . 49
3.9 Assignment of the charge state by the shift of the resonance peaks 55
3.10 Conclusion 59

4 Periodic charging of molecules coupled to the motion of an AFM tip 61
4.1 Single-electron charging 62
4.2 Experimental details and sample preparation 63
4.3 Gating the charge state with electric field 66
4.4 Newns-Anderson model of adsorption 71
4.5 The smooth charge transition 73
4.6 Temperature-dependent experiment 76
4.7 The absence of dissipation 79
4.8 Charging rings in AFM 80
4.9 Difference image 80
4.10 Threshold voltage for charging 84
4.11 Conclusion 89

5 A functional cell for molecular quantum cellular automata 91
5.1 Introduction 91
5.2 Activation of the molecules by patterning the cell . . . 94
5.3 The charge state evolution: dimeric structures 97
5.4 Lateral-spectral and constant-height maps: trimeric structures 101
5.5 Bias dependent imaging: quadromers 104
5.6 Vertical manipulation 105
5.7 Conclusion 107

6 A rocker switch formed by anchoring a single molecule to insulating surface 109
6.1 Introduction 109
6.2 Methods 111

6.3 Adsorption sites on a bilayer NaCl/Cu(311) 112
6.4 Manipulation of the charge state and adsorption geometry 115
6.5 Reversible bidirectional actuation of a molecular rocker switch 119

7 Regioselective dehydrogenative aryl-aryl bond formation 123
7.1 Introduction to the concept of regioselectivity 124
7.2 Materials and methods 127
7.3 Sample preparation 128
7.4 A discrimination of a pyridine from a pyrazine unit . . 130
7.5 Simulation of AFM images 135
7.6 Hierarchy of dimer structures 138
7.7 A possible mechanism for selective bond formation . . 142
7.8 Conclusion 143
7.9 Contributors to this work 143

8 Summary 145

Bibliography 149

Acknowledgements 179

1 Theoretical background

The field of surface science was revolutionized by the invention of the scanning tunneling microscope (STM) by Gerd Binnig and Heinrich Rohrer in 1981 [1, 2]. For this achievement they were awarded the 1986 Nobel Prize in Physics [3]. The STM has become an important scientific research instrument in the emerging field of nanotechnology and diagnostic tool in industrial laboratories. It allows imaging and spectroscopy with atomic resolution in real space and is able to resolve electronic, vibrational and magnetic properties locally. In addition, the manipulation of matter on the atomic scale can be performed.

Because the STM detects the current, it is limited in sense it can be used to image surfaces of conductive materials [4]. To overcome this limitations, the atomic force microscope (AFM) was developed and introduced in 1986 [5]. It took only one year for the newly introduces technique to achieve atomic resolution in contact mode [6, 7]. The development of dynamic AFM allowed measurements without sample or tip being modified in the scanning process. The large amplitude operation required to run soft cantilevers was good to prevent the tip from crashing but was insensitive to short-range interactions. The use of stiff cantilevers allowed for small-amplitude operation with high sensitivity to short-range forces: the invention of tuning forks [8] reduced the relative frequency shift signal allowing for sub-Ångström amplitudes to be used as well as to combine AFM with STM in the same experimental setup by fixing the conductive tip to one end of the force sensors.

The working principle of STM is explained in many books and review articles [3, 9, 10]. Nevertheless, in this chapter we will shortly introduce the basics of STM and the main data acquisition modes. The aspects of a double barrier tunneling junction and the Coulomb blockade will be described next because of their high relevance for the results shown in this thesis. Finally, we will discuss the fundamental properties of AFM, which will be followed by a description of the Kelvin probe force microscopy.

1.1 Scanning Tunneling Microscopy

Imaging with STM involves moving an atomically sharp tip over a conductive sample at a few-Ångström distance to obtain topographic information about the surface, while a bias voltage is applied between the two electrodes. This is somewhat similar to Braille reading, where the reader's finger sense the arrangement of raised dots in characters. In principle, STM is based on the effect of quantum tunneling. An electron is a quantum mechanical particle and as such has a finite probability to tunnel through the potential barrier that classically would never overpass [11]. The potential barrier is the vacuum gap between tip and sample. If we assume that both electrodes are made of the same material and are in electronic equilibrium, that is, no bias is applied, the tunneling current will be equal to zero. If the positive bias is applied to the sample, electrons will tunnel from the tip into the sample (Figure 1.1). For a negative bias applied the current has the opposite direction.

The tunneling process can be most easily understood by considering the transmission through a one-dimensional rectangular potential barrier. If the barrier has height ϕ_0 and width Δz, $\phi(z) = \phi_0\Theta(\Delta z/2-|z|)$ where Θ is the Heaviside function, the transmission probability [12] is

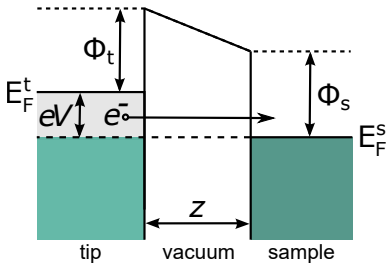

Figure 1.1: Energy diagram of the tunneling through the potential barrier. Applying positive bias voltage V to the sample with respect to the tip allows electrons to tunnel from occupied states in the tip to unoccupied states of the sample. $E_{\mathrm{F}}^{\mathrm{s,t}}$ are the Fermi levels of surface and tip, $\Phi_{\mathrm{s,t}}$ the work functions and z is the distance between tip and sample. The barrier height is determined by the respective work function and the bias voltage V.

given as

$$T(E) \approx \exp(-\frac{2}{\hbar}\int_{-\Delta z/2}^{\Delta z/2}\sqrt{2m(\phi(z')-E)}\mathrm{d}z'), \tag{1.1}$$

where $\hbar$ is the reduced Planck's constant. From quantum mechanics stems a finite probability for the electron to tunnel through the barrier, increasing with decreasing the width Δz or $\phi(z') - E$. For a metal-vacuum-metal tunneling setup, the barrier height ϕ is given by the work function of the material. The inverse decay lenght defined as $\kappa = \sqrt{2m\phi}/\hbar$ is of the order of $1/\text{Å}$ and the tunneling current changes by an order of magnitude when the tip-sample distance is altered by one Ångström. The rapid decay of the tunneling current with separation is fundamental for the high resolution obtained with STM.

While the above described one-dimensional model is already sufficient to qualitatively describe the tunneling current dependence on the gap width, a more realistic, three dimensional many-body picture is required for a quantitative description of the electron tunneling phenomenon. Such theory was initially developed and presented by John

Bardeen in 1961 [13], exactly 20 years before the invention of STM. At a time, Bardeen was working on a theory that would explain the tunneling currents flowing in the metal-oxide-metal junctions[1].

In Bardeen's formalism, the tunneling matrix element M_{mn} between the electronic states of the tip Ψ_{m} and the surface Ψ_{n} is given by

$$M_{\mathrm{mn}} = -\frac{\hbar^2}{2m_{\mathrm{e}}} \int_S (\Psi^*_{\mathrm{m}} \nabla \Psi_{\mathrm{n}} - \Psi_{\mathrm{n}} \nabla \Psi^*_{\mathrm{m}}) \mathrm{d}\mathbf{S} \tag{1.2}$$

where the integral is over an infinite arbitrary surface S within the vacuum barrier region that separates tip and sample. To calculate the tunneling current I at the bias voltage V_{s}, only elastic tunneling from occupied into unoccupied states of the counter-electrode are considered. The transmission in the opposed direction is substracted. The tunneling current is then given by

$$I = \frac{2\pi e}{\hbar} \sum_{\mathrm{m,n}} f(E_{\mathrm{m}})[1 - f(E_{\mathrm{n}} + eV_{\mathrm{s}})]|M_{\mathrm{mn}}|^2 \delta(E_{\mathrm{m}} - E_{\mathrm{n}}), \tag{1.3}$$

where f is the Fermi-Dirac distribution describing the mean occupation probability of states of the two metals at the energies E_{m} and E_{n}. Dirac's delta function $\delta(E)$ describes the conservation of energy in the case of elastic tunneling.

Because the exact wave functions of the tip and the sample are unknown, the matrix element has to be approximated. J. Tersoff and D. R. Hamann developed a theory in which they assumed a spherically symmetric wave function for a tip state, as displayed in Figure 1.2. In addition, the electrons in the sample are described by the surface wave functions which propagate freely parallel to the surface plane, but display exponentially decaying behaviour into the vacuum [16, 17].

[1] The experimental observations were made by Giaver [14] and Nicol [15] in 1960.

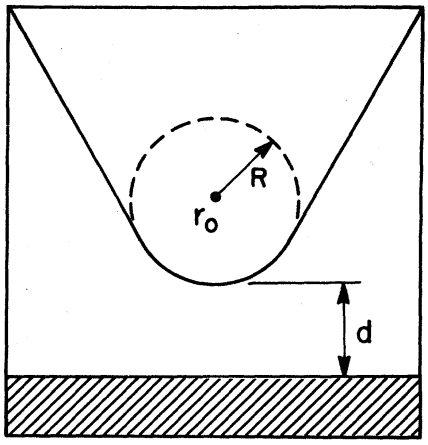

Figure 1.2: Schematic image of the tunneling geometry. The probe is assumed to be locally spherical, giving rise to radially symmetric tip wave function (s-wave). The image is from Ref. [17], J. Tersoff and D. R. Hamann paper from 1985.

Substituting the matrix elements calculated with a help of this wave functions

$$M_{\mathrm{mn}} = 4\pi R \frac{\hbar^2}{2m} \Omega^{-1/2} e^{\kappa R} \Psi_{\mathrm{n}}(\vec{r}_0), \tag{1.4}$$

where R is the radius, $\vec{r}_0$ the center of the curvature and Ω is the volume of the probe, in a limit of low temperature and small bias voltages, the tunneling current becomes:

$$I = 32\pi^3 e^2 \hbar^{-1} V_{\mathrm{s}} R^2 D_{\mathrm{t}}(E_{\mathrm{F}}) e^{2\kappa R} \kappa^{-4}(E_{\mathrm{F}}) \sum_{\mathrm{n}} |\Psi_{\mathrm{n}}(\vec{r}_0)|^2 \delta(E_{\mathrm{n}} - E_{\mathrm{F}}). \tag{1.5}$$

$D_{\mathrm{t}}(E_{\mathrm{F}})$ is the density of states per unit volume of the tip. Further simplified expression for the current is

$$I \propto V_s \rho_{\mathrm{t}}(E_{\mathrm{F}}) \rho_{\mathrm{s}}(E_{\mathrm{F}}, \vec{r}_0) \tag{1.6}$$

where $\rho(E_{\mathrm{F}})$ is the local density of states. The constant-current STM

images at low bias voltages thus represent **the contours of constant local density of states** of the sample.

The theory is extended to finite bias voltages (our experiments satisfy the low temperature limit) by integrating over energy interval eV_s. An additional assumption can be made that the tip density of states is flat in this measurement interval. The tunneling current is then equal to

$$I \propto \rho_t(E_F) \int_0^{eV} \rho_s(E_F + \epsilon, \vec{r}_0) d\epsilon. \tag{1.7}$$

The STM at low bias voltages thus represents the local density of states and at finite bias voltages **the integrated local density of states** of the sample from E_F to $E_F + eV_s$.

1.1.1 Imaging modes

The most commonly used imaging mode in STM is the constant current mode. A feedback controller compares the actual with the set-point current (predefined by the user) and adjusts the voltage applied to the piezo controlling the tip height to keep the tunneling current at the steady value (Figure 1.3). By recording this voltage i.e. the displacement in height, topography of the surface can be extracted. An alternative way to scan over the surface is to keep the tip height constant and measure the tunneling current. However, this method involves the risk of crashing into the surface or adsorbates, and is therefore mainly used on atomically flat surfaces or areas previously scanned in constant current mode. The advantage of this mode is that it can be used at a relatively high scanning frequencies, except when being employed for spectroscopic imaging where frequency shift or differential conductance are acquired.

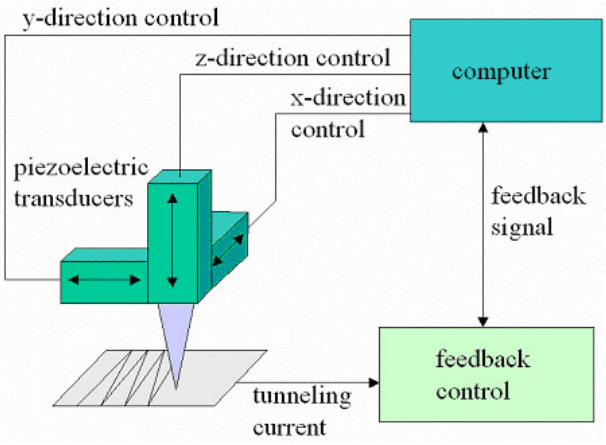

Figure 1.3: Schematic view of the STM setup. The metallic tip is attached to one of three piezoelectric transducers: x, y, and z piezo, that expand and contract in a controlled way upon application of suitable voltages. The tip can be, in general, moved in all spatial directions, but is made to raster the xy plane in a controlled way by applying appropriate voltage signal to x piezo and slower voltage ramp on the y piezo. The tunneling current is after amplification by a high-gain, low noise preamplifier, compared to a set-point (reference) value. The difference between the two is amplified and used as a feedback signal to drive the z piezo. If the tunneling current is larger than the set-point value, the z piezo withdraws the tip from the sample and vice versa. A detailed description of the experimental setup will be given in chapter 2. From Ref. [18].

1.2 Double barrier tunneling junction

Throughout this thesis, we will encounter situations where we are interested in studying intrinsic properties of the adsorbates. For molecules adsorbed directly on the metal surfaces, the electronic properties are affected by the metal states and surface-mediated orbital hybridization (see section 4.4). To prevent this unwanted coupling, an ultrathin insulating film can be introduced. The layer has to be thin enough to maintain the STM current, but still thick enough to

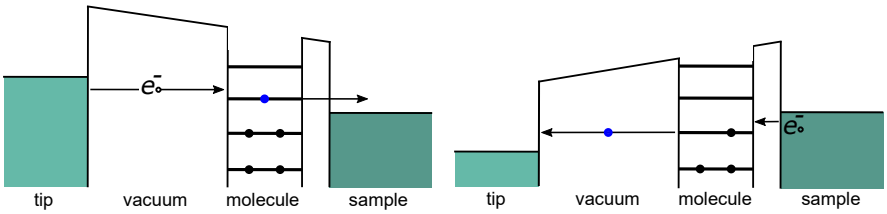

Figure 1.4: Energy diagram of a DBTJ formed by introducing an insulating film between molecule and metal substrate. In this way, the electronic levels (both unoccupied and occupied) of single molecules can be probed by changing the bias voltage. (left) Applying positive bias voltage V to the sample with respect to the tip allows electrons to tunnel from the tip to unoccupied state(s) of the molecule and later to unoccupied states of the sample. (right) The electron tunneling process through molecule for negative bias voltage applied.

electronically decouple the adsorbate.

Additional potential barrier formed by introducing a film leads to a formation of what is usually referred to as *a double-barrier tunneling junction* (DBTJ). In this geometry the electron tunnels sequentially, first from the substrate to the adsorbate to localize there, and then to the tip, or vice versa (see Figure 1.4). Differential conductance spectra acquired above the adsorbates show very pronounced peaks. In this way, the energetic positions of the (un)occupied molecular orbitals are detected by adding/removing of an electron[2]. The bias window between the first maxima on the negative and on the positive bias side is called *in gap* region. Here, the contrast in the STM images of molecules could still arise even though there are no states available to tunnel through. This phenomenon can be explained by the local modification of the tunneling barrier height.

Not quite the same, but rather similar, is the situation when the

[2]It would be actually more precise to talk about the negative/positive ion resonances, but terms like HOMO, LUMO. LUMO+1 etc. are still widely used for simplicity.

molecule adsorbs directly on a metal but does not react strongly with the substrate. Despite being challenging to define what exactly the second barrier is in this case, DBTJ can still be applied to quantitatively explain the results (chapters 4 and 5).

1.3 Coulomb blockade

Let consider a capacitor made of two metal surfaces separated with an insulating layer and assume that both capacitor plates carry the same charge Q of opposite signs. The energy stored between the capacitor plates is

$$E_{\mathrm{C}} = \frac{Q^2}{2C}. \tag{1.8}$$

Now, let a single electron tunnel between the plates, such that new distribution of charge is made: $Q + e$ resides on positive and $-Q - e$ on the negative plate, where e is the electron charge. The new energy stored in the capacitor is $E_{\mathrm{C}}^{final} = \frac{(Q+e)^2}{2C}$ and the energy difference $\Delta E = E_{\mathrm{C}}^{final} - E_{\mathrm{C}} = \frac{e(Q+e/2)}{C}$. For the tunneling to occur it is required that $\Delta E < 0$, yielding

$$Q > -\frac{e}{2}. \tag{1.9}$$

For both polarities, the current will flow only when a voltage is sufficiently large: $|V| > |e|/2C$. This is the **Coulomb blockade** and the energy is called *the charging energy*:

$$E_{\mathrm{C}} = \frac{e^2}{2C}. \tag{1.10}$$

The Coulomb blockade raises from the energy barrier to be exceeded when one additional electron is to be added or removed. By considering a quantum dot/molecule system coupled to external leads, like in the case of DBTJ, one obtains the same result if the tunneling junctions are modeled as leaky capacitors. The term originates from

transport measurements through a quantum dot where a suppression of current between the source and drain was observed for a certain values of gate voltages [19].

The temperature has a very important role in Coulomb blockade. For the phenomenon to occur, the electron thermal energy has to be much lower than the charging energy ($E_C \gg k_{BT}$). As the energy level separation for quantum dots is small the experiments need to be carried out at very low temperatures in order to see the effect. In addition, tunneling has to be limited to some degree i.e. the tunneling resistance $R_t = \tau/C$, where τ is the lifetime of an electron on one side of the barrier, must be larger than $R_t \gg \hbar/e^2$ [20]. It is also obvious that the smaller (more localized) quantum dots and molecular orbitals have larger charging energies E_C.

1.4 Atomic force microscopy

The main difference between the AFM as compared to the STM is that the imaging signal is given by the force between the scanning probe tip and the sample, instead of the tunneling current. The central working element of every AFM is the flexible cantilever that senses the forces. Initially built from Au foil, the cantilevers are nowadays mass-produced by microfabrication with integrated tips from silicon, metal or other material. The cantilever is characterized by the following intrinsic properties: its spring constant k, eigenfrequency f_0 and quality factor Q. The deflection of the cantilever when the tip is approached to the sample is most commonly sensed by measuring displacement of a laser beam reflected from its back side (known as the optical beam deflection system). The reflected laser spot falls on a photodiode divided into sections and generates the photocurrent which magnitude depends on the position of the spot. The combined STM/AFM apparatus used in this thesis employs slightly different detection scheme (see chapter 2.3).

There are two different operation modes of AFM. The contact (also known as static) and the noncontact or *dynamic* mode. In contact mode, the tip is mechanically addressed towards the surface. The force F acting on the tip leads to a quasi-static deflection $x = F/k$ of the cantilever. If the feedback control is set to keep the deflection x constant during the scan, a surface of constant force is measured. It is obvious that the deformation of the sensor has to be significantly larger than any deformation of the sample or the tip. This is why a relatively soft cantilevers are required to give a measurable deflection before causing any damage. Also, in this mode large lateral forces can build up damaging or sweeping weakly bound material. It is therefore mainly used for imaging hard surfaces where no significant modification of morphology is expected.

In AFM, there is always present issue of snap-in of the cantilever, that is, jump to contact. To overcome this, the vibratory motion of the cantilever perpendicular to the sample surface provides the required force to counteract the attractive interactions. When the tip is closest to the sample surface, as long as $|F_{\max}| \leq k_0 \cdot A$ the restoring force of the cantilever can avoid a snap-in. $F_{\max}$ represents the maximum attractive force between tip and surface. This can be easily achieved by using amplitudes A that are large enough or cantilevers of necessary stiffness k_0.

Dynamic AFM can be operated using different control methods. It is important to note that environment affects the type and intensity of forces acting between tip and sample, determining which mode is better suited for imaging. In the *amplitude modulation* mode (AM), the actuator is driven at a fixed off-resonant frequency. As the tip approaches the surface, due to the interactions, the amplitude changes and is used as a feedback signal for imaging. The issue is when the Q value is very high (which is the case under UHV conditions), the AM AFM then becomes very slow due to large timescale for the amplitude change. To decouple the speed from the Q factor the *frequency modulated* mode or FM AFM uses the deflection signal (bandpass filtered

and phase shifted) to create the signal which is fed back to the actuator. When the oscillation frequency changes due to the tip-sample forces, a phase-locked loop determines the new oscillation frequency f. The frequency shift $\Delta f = f - f_0$ is then used as the imaging signal. A feedback loop adjusts the drive to keep the oscillation amplitude constant. The time the system takes to react to a change of the resonance frequency is in the same order of magnitude as one oscillation period.

1.4.1 Dynamic AFM

In the following section we will describe the cantilever's motion as damped, externally driven linear harmonic oscillator (LHO) in the external force field. The approximate expression for the force as a function of the frequency shift will be given.

Let consider the oscillation properties of the spring pendulum with the point mass m attached to the massless spring with stiffness k_0. If a single degree of freedom is assumed, the equation of motion has a following form:

$$\ddot{z} + \omega_0^2 z = 0, \tag{1.11}$$

where $\omega_0 = 2\pi f_0 = \sqrt{\frac{k_0}{m}}$ is the natural or the resonance frequency, which is, as mentioned above, an intrinsic property of the system. If no external forces are applied, oscillations are free and harmonic: $z(t) = A\cos(\omega_0 t + \phi_0)$. The initial phase ϕ_0 and amplitude A are determined by starting values for the coordinate z and kinetic energy.

The tunning fork is a real oscillator and as such has some intrinsic damping due to friction (Figure 1.5, left). If these energy loses are not compensated externally, the oscillations will damp until they stop. To account for that, we can introduce the force $\vec{F}_\mathrm{F} = -\beta\vec{v}$ where β is constant and positive. The equation of motion Eq. 1.11 can be now

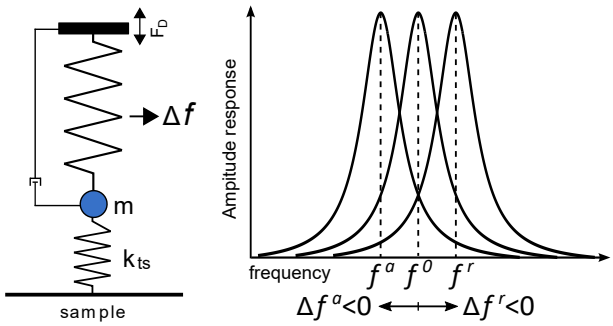

Figure 1.5: (left) The cantilever is described as an effective mass m attached to a spring of stiffness k_0. The tip-sample interaction is described by an additional spring of stifness k_{ts}. Additional properties, such as tip-sample damping and applied bias, are not shown. (right) The resonance spectrum of the free cantilever f changes due to the tip-sample interaction. In FM AFM the cantilever is actively oscillated at its resonance frequency and the frequency shift Δf is the observed signal. Repulsive forces increase the resonance frequency f^r such that $\Delta f^r = f^r - f < 0$ and attractive forces decrease this resonance frequency.

written as

$$\ddot{z} + 2\delta\dot{z} + \omega_0^2 z = 0, \tag{1.12}$$

where $\delta = \beta/2m$ is a damping factor. The type of oscillations depends on the ratio between δ and ω_0. In a case of small resistance ($\omega_0 > \delta$) oscillations are periodic with exponentially decreasing amplitude $z(t) = Ae^{-\delta t}cos(\omega t + \phi_0)$, $\omega = \sqrt{\omega_0^2 - \delta^2}$.

The quality factor

$$Q = \frac{2\pi E(t)}{\Delta E_{\mathrm{T}}} \tag{1.13}$$

is an important parameter which describes the dissipative processes in the system and is defined as the ratio between the stored and energy loss over one period ΔE_{T}. As the oscillator's initial total energy $E_0 = \frac{m\omega_0^2 A^2}{2}$ as a function of time in a limit of small damping $\omega_0 \gg \delta$ equals

to $E(t) = E_0 e^{-2\delta t}$, we have

$$Q = \frac{\omega}{2\delta} \approx \frac{\omega_0}{2\delta}. \tag{1.14}$$

The Q is a dimensionless factor that is actually the number stating how many oscillations are there in a characteristic damping time $\tau = 1/\delta$. To determine the Q and ω_0 of the cantilever, we use a constant excitation mode at the distances far away from the sample, where the interaction between tip and sample is considered to be negligible. By constant excitation we mean an external driving force $\vec{F}_D$ acting on an oscillator. In a presence of $\vec{F}_{\mathrm{F}}$ and $\vec{F}_{\mathrm{D}}$, the equation of motion is

$$\ddot{z} + 2\delta\dot{z} + \omega_0^2 z = \frac{F_0}{m}\cos\Omega t. \tag{1.15}$$

where Ω is the driving force frequency. Only forced oscillation will be present over the time $t >> 1/\delta$. The amplitude is given as

$$A_0(\Omega) = \frac{F_0}{m\sqrt{(\omega_0^2 - \Omega^2)^2 + 4\delta^2\Omega^2}}. \tag{1.16}$$

which represents a resonance curve. It is obtained by measuring the oscillation amplitude when the driving frequency is swept. The maximum oscillation amplitude corresponds to the resonance frequency $\Omega_{\mathrm{R}} = \sqrt{\omega_0^2 - 2\delta^2}$ and the phase shift is

$$tg\phi = \frac{2\delta\Omega}{\Omega^2 - \omega_0^2}. \tag{1.17}$$

If the two frequencies, the natural frequency ω_0 and the forcing frequency Ω are equal, the phase shift will be $\pi/2$ no matter how large is dissipation in the system.

A consequence of Eq. 1.16 is a rapid decay of the oscillation amplitude as the frequency goes away from the resonance value. We define $\Delta\Omega$ as the full width of the resonance curve at $1/\sqrt{2}$ of the maximum

amplitude. For small δ it has a magnitude of 2δ and a quality factor is then $Q = \omega_0/\Delta\Omega$. This mean that the resonance width is determined by Q and ω_0.

Finally, we consider the case of an oscillator, damped and driven, in a force field. This corresponds to a situation when the tip of the microscope is brought very close to the substrate and is therefore affected by the forces between tip and sample: F_{ts}. Now, we can write the equation of motion of the driven and damped oscillator as:

$$\ddot{z} + 2\delta\dot{z} + \omega_0^2 z = \frac{F_{\mathrm{D}}}{m}\cos(\Omega t) + \frac{F_{\mathrm{ts}}}{m}. \tag{1.18}$$

The external force F_{ts} results in the change of the position about which the oscillations are occuring z_0. For small oscillations, we can exchange $z(t)$ in Eq. 1.18 with $z'(t) = z(t) - z_0$:

$$\ddot{z}' + 2\delta\dot{z}' + \omega_0'^2 z' = \frac{F_{\mathrm{D}}}{m}\cos(\Omega t). \tag{1.19}$$

Eq. 1.19 and Eq. 1.15 differ only in the new spring stiffness k' and new equilibrium position z_0, where $\omega' = \sqrt{k'/m}$ and $k' = k - \frac{\partial F_{\mathrm{ts}}}{\partial z}$. Due to the force field, the oscillator is detuned to a new resonance frequency (see Figure 1.5).

Assuming further the force gradient is small compared to k, we can take Taylor expansion of the additional frequency shift

$$\Delta\Omega = \Omega_{\mathrm{R}}' - \Omega_{\mathrm{R}} = \Omega_{\mathrm{R}}\left(\sqrt{1 - \frac{\omega_0^2}{k\Omega_{\mathrm{R}}^2}\frac{\partial F_{\mathrm{ts}}}{\partial z}} - 1\right) \tag{1.20}$$

where Ω_{R} is the resonant frequency in the presence of the force field, to obtain

$$\Delta f \propto -\frac{f_0}{2k}\frac{\partial F\mathrm{ts}}{\partial z}. \tag{1.21}$$

The frequency shift is therefore **approximately proportional to tip-sample force gradient** in a limit of small amplitudes [21].

For large (arbitrary) amplitudes, a more general expression for the frequency shift Δf exists. It is derived from the first-order perturbation theory with the Hamilton-Jacobi approach [22]:

$$\begin{aligned}\Delta f &= -\frac{f_0^2}{kA}\int_0^{1/f_0}\{F(z+A[1+\cos(2\pi f_0 t)])\cos(2\pi f_0 t)\}\mathrm{d}t \\ &= -\frac{f_0}{\pi kA}\int_{-1}^{1}\left\{F(z+A[1+u])\frac{u}{\sqrt{1-u^2}}\right\}\mathrm{d}u,\end{aligned} \tag{1.22}$$

where z is the distance of closest tip approach during the oscillation. If the $F(z)$ is known the formula can be used to obtain Δf. Sader and Jarvis deconvolution approach to calculate the forces from the $\Delta f(z)$ for arbitrary oscillation amplitude:

$$F(z) = \frac{2k}{f_0}\int_z^{\infty}\left\{\left[1+\frac{A^{1/2}}{8\sqrt{\pi(t-z)}}\right]\Delta f(t) - \frac{A^{3/2}}{\sqrt{2(t-z)}}\frac{\partial[\Delta f(t)]}{\partial t}\right\}\mathrm{d}t \tag{1.23}$$

is only valid when there is no dissipation in the junction i.e. in the elastic regime of tip-sample interactions [23].

1.4.2 Forces in AFM

In AFM various forces contribute to the total force between the tip and the surface. Although all forces detected in the experiments are of electromagnetic origin, they can very much differ in range and strength. It is almost impossible to separate the different force contributions even when the oscillation amplitude is adjusted to be of the same order as the characteristic length scale of the force that is to be probed. For example, only with the atomically defined tip terminations and oscillation amplitudes of a fraction of an Ångström one can gain a certain control over the short-range interactions. In chapter 4 we will show how by a suitable subtraction of Δf images, the signal mainly produced by electrostatic interactions can be extracted.

Van der Waals forces (vdW). The vdW forces stem from dipole interactions between atoms and molecules (both polar and non-polar). They include forces between the permanent dipoles, a permanent dipole and an induced dipole, and the forces between instantaneously induced dipoles (known as London dispersive forces). There are also interactions between the dipole moments and the higher multipole moments, and the mutual interactions of the latter with each other, but they are usually significantly smaller. In general, the vdW forces can be attractive and repulsive. The dispersion forces are attractive and are always present between the atoms. For the macroscopic objects, due to their additive character they can play very important role. In AFM they lead to a large attractive background signal. In order to reduce their influence (commonly, they are not of interest in our measurements) it is important to have very sharp tip on a longer vertical scale as compared to a single atom terminated tips required for STM operation.

The vdW forces between tip and surface can be obtained by modeling the tip with a paraboloid with local radius R at a closest distance z from the infinite plane (Hamaker approach) and calculating all diatomic vdW interactions [24]. The vdW force is then

$$F_{\mathrm{vdW}}(z) = -\frac{A_{\mathrm{H}} R}{6z^2} \tag{1.24}$$

where A_{H} is the Hamaker constant that depends on the material (units of eV). A_{H} is also tip-sample separation dependent (and therefore not strictly a constant) due to retardation effects that arise due to smaller coupling efficiency at larger distances. It is clear from Eq. 1.24 that smaller radius R (= sharper tip) reduces the force.

Chemical force (CF). The CFs are significant at distances where the wave functions of the tip and the sample start to overlap, so they are very short-range in nature, much less than a nanometer. This is a reason why they are responsible for atomic resolution in AFM. The origin of repulsive CFs are the ion core repulsions or the Pauli exclusion

principle: As only two electrons can occupy the same quantum state at a same time, the electrons will be forced to occupy levels at higher energies, which would lead to the increase in the system total energy. On the other hand, if the overlap of the wave functions reduces the total energy, CFs are attractive. These are the forces that bind the atoms together to form the molecules and are related to the nature of the atomic species involved.

To model them, the Lennard-Jones potential (LJ) for two atoms as a function of their distance is employed [25]:

$$E_{\mathrm{LJ}}(z) = E_0\left(\left(\frac{z_{\mathrm{b}}}{z}\right)^{12} - 2\left(\frac{z_{\mathrm{b}}}{z}\right)^{6}\right) \tag{1.25}$$

where E_0 is the binding energy at the binding distance z_{b}. The LJ potential is not perfect way to describe Pauli repulsion, as only pairwise interactions are included. The force derived from LJ potential is

$$F_{\mathrm{LJ}}(z) = \frac{12E_0}{z_{\mathrm{b}}}\left(\left(\frac{z_{\mathrm{b}}}{z}\right)^{13} - \left(\frac{z_{\mathrm{b}}}{z}\right)^{7}\right). \tag{1.26}$$

Electrostatic forces (EF). The EFs are longe-range in nature and are always attractive, so the corresponding frequency shift is negative. The tip and the sample can be treated as two plates of a capacitor, to which a capacitance $C(z)$ is attributed. If each plate has a charge $|q|$, then the energy of the system is $U = q^2/2C$. The electrostatic force of a capacitor reads

$$F_{\mathrm{el}} = \frac{1}{2}\frac{\partial C}{\partial z}(V - V_{\mathrm{CPD}})^2 \tag{1.27}$$

where V_{CPD} is a *contact potential difference* (CPD) and V an externally applied voltage (bias voltage). By setting this value such that $V = V_{\mathrm{CPD}}$, the electrostatic force is compensated and the force is minimized, allowing a direct readout of the CPD. Obviously, force has a parabolic dependence on the bias voltage $F_{\mathrm{el}} \propto V^2$. The EFs arise from the potential difference between tip and sample and, on the nanometer scale, from local charges.

1.4.3 Kelvin probe force microscopy

In continuation of the previous section, in the following we will describe how AFM can be used to sense ES forces originating from the distribution of charges. But first, we will introduce method for the work function difference determination.

We start our explanation by considering two metals with different work functions Φ_1 and Φ_2 being far apart. They share the same vacuum level but their Fermi levels are not aligned (Figure 1.6, left panel). When metals are brought close and into electrical contact, electrons will flow until the Fermi levels become equal and an equilibrium is achieved (middle panel). Net charges accumulated on their surfaces cause an electric field E in the gap and a contact potential eV_{CPD} to build up. An actively applied voltage (compensation voltage) restores the situation from the beginning. The voltage $V = V_{\mathrm{CPD}}$ required to minimize electrostatic interactions corresponds to the difference in work functions between the sample and probe $V_{\mathrm{CPD}} = \frac{1}{e}(\Phi_1 - \Phi_2)$ (right).

This method to measure the differences in work functions between two metals dates back to 1898 when Lord Kelvin was performing experiments with two distance-oscillating parallel plates when he realized that an AC electric current induced by this motion could be nullified with an external voltage applied between them [27]. This DC voltage cancels out the electrostatic field so no capacitive current is induced.

The Kelvin probe method was combined with AFM in 1991 and Kelvin probe force microscopy (KPFM) was introduced to measure local variations of the work function difference [28, 29]. Figure 1.6 is usually exploited when Kelvin probe method has to be explained, but the real situation when the sharp tip is close to the surface is way more complex. At the metal surfaces the crystal symmetry is broken, a charge redistribution occurs which leads to an effective surface dipoles. The

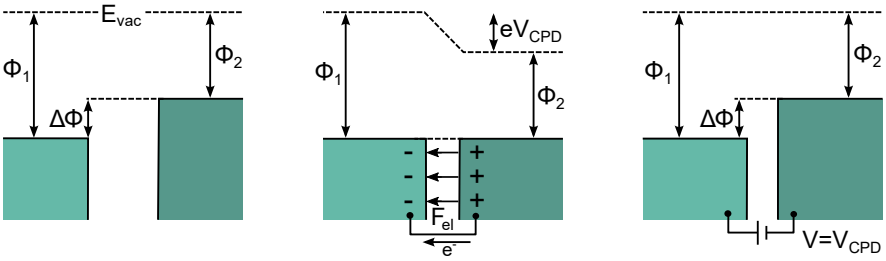

Figure 1.6: Illustration of the Kelvin principle. (left panel) The vacuum level E_{vac} is shared between two isolated metals with different work functions. (middle) The two metals are electrically connected and the Fermi levels are at the same energy. The charge transfer results in an electric field E (and therefore to attractive force F_{el}) between the metals. (right) The situation is restored when an external voltage $V = \Delta\Phi/e$ compensates the contact potential difference (CPD) and minimize the electrostatic interaction. Figure after Ref. [26].

potential from the bulk does not drop to zero suddenly at the surface-vacuum interface, but instead it decays within few Ångströms to escape the surface potential. How it will decay depends on the nature of the surface, for metals, electrons are screened by their image charge and the potential drops as $\propto 1/z$ [30]. For ionic surfaces, like NaCl, where charges of opposite signs are next to each other, the potential drops exponentially [31]. Individual charged adsorbates can affect the potential landscape locally. In FM AFM, the tip can be approached to these distances and the work function, as a macroscopically defined property does not reflect the measured potential difference any more. Therefore, a concept of work function has to to be extended to the local scale, so it is rather *the local contact potential difference* (LCPD) that we are talking about than the concept of the work function difference [32–34].

Unlike to Kelvin method, where a current was used for CPD determination, in KPFM it is the electrostatic force that is exploited as a signal. To measure the ES force, an electrical AC voltage is applied in the junction (in addition to the DC bias voltage) to generate oscillat-

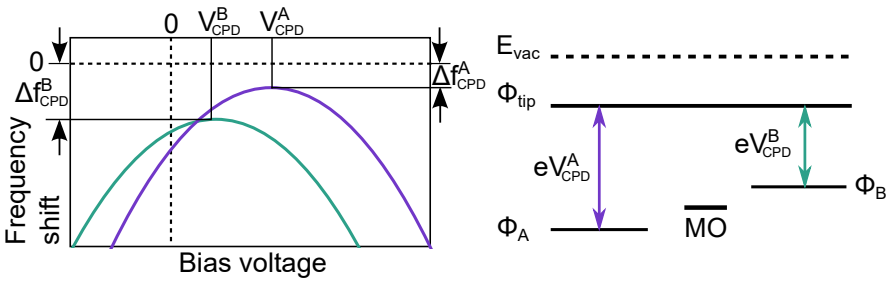

Figure 1.7: (left) Two $\Delta f(V)$ curves measured on two materials with different Φ. The electrostatic force is minimized at $V^{\mathrm{A}}_{\mathrm{CPD}}$ and $V^{\mathrm{B}}_{\mathrm{CPD}}$. Even for compensated CPD, the Δf is non-zero because of the other force contributions still acting on the sensor. (right) A diagram of the work function differences and the vacuum level alignment rule. The relative position of the molecular orbital (MO) with respect to the Fermi level of a substrate's material determines the charge state of the molecule. The position of the Fermi level with respect to the vacuum level is determined by their work functions. The MO can be either empty or filled depending on which material is used as a substrate i.e. by tuning the work function value, the charge state of the molecule can be manipulated (see chapter 3).

ing ES forces. The resulting frequency shift signal contains terms with the same frequency as the AC signal. These are derived by means of a lock-in amplifier and compensated (nullified) by applying a separate DC voltage V_{CPD} by the feedback controller. Usually, this is performed during scanning in constant frequency feedback, so that the ES potential landscape of the sample can be mapped simultaneously with the topography.

Alternatively, the contact potential can be determined from the frequency shift measured at a fixed tip position as a function of the bias voltage (Kelvin probe force spectroscopy - KPFS) [35]. Such a spectra shows a parabolic behaviour (see Eq. 1.27) and the LCPD is determined by the position of the maximum of the curve. As compared to the KPFM imaging speed, this method is slow (as the spectrum has to be recorded at every image point and later fitted with a parabola),

requires high stability and a way to compensate for a drift. Recording parabolas, however, has advantages over KPFM as it yields high spatial resolution even when the variations of LCPD is relatively small and allows for detection of any deviations from the parabolic shape. We used this method in chapters 3 and 6 to determine local shifts of the LCPD for a differently charged molecules. Any deviations from the parabolic shape are usually sign of the static [36, 37] and dynamic charging processes (chapter 4) or ionic polarization [38].

Figure 1.7 (left panel) shows two KPFS curves on two materials that have different work functions. In this example, the blue material has a larger workfunction than other material.

When two materials with different work functions are present in the same junction, or due to geometric inhomogeneities of the surface, the KPFS measurements are the subject of the *averaging effects* [39]. The CPD is not just a value right below the AFM tip but is a weighted average of different surface areas with different work functions. Even when the surface is homogeneous and atomically flat, these effects can occur if the work function of the tip is inhomogeneous, that is, the mesoscopic shape of the tip can have a considerable influence on the tip work function. In that case, the CPD value should strongly depend on the absolute tip-sample distance. Additional problems can arise when the tip is very close to the surface. Parasitic potential drops may strongly influence KPFS results [40] or high currents can destroy sensitive samples.

2 Experimental setup and methods

2.1 LT-UHV STM/AFM apparatus

All SPM experiments presented in this thesis were performed using low-temperature combined STM/AFM, based on a qPlus sensor [8]. The design was developed by Dr. Gerhard Meyer [41] and commercialized by Dr. Sven Zöphel [42]. A very detailed description of the system can be found in Refs. [43, 44]. Here, only the most relevant parts of the setup will be shortly summarized.

The vacuum chamber consists of three separable parts: (i) a chamber housing the SPM head, separated from (ii) the preparation chamber by a gate valve and (iii) a small chamber (load-lock) attached to the preparation chamber. The load-lock serves for a quick sample and evaporator transfer from the ambient to UHV conditions. It can be pumped separately by the turbomolecular and roughening pumps. The ion and titan sublimation pump are attached to the preparation chamber which is equipped with a sputter gun, leak valves, salt evaporators and, if needed, a quadropole mass spectrometer for residual gas analysis. The pressures down below $4 \cdot 10^{-11}$ mbar are readily attainable. The samples are handled and transfered between the preparation chamber and the microscope by a three-axial manipulator which allows for a rotation along x-axis and can be cooled by cryogenic liquids. The preparation chamber is also equipped with a storage that can hold up to six samples/evaporators. The metal crystals are heated indirectly

via button heaters on which they are mounted. The temperature of the sample is monitored via K-type thermocouple attached to the side of the sample. In this way, the samples can be prepared (sputtering, annealing, molecule evaporation) in a wide temperature range. Transferable evaporators are employed for deposition of molecule or metal atoms on the cold surface. The SPM scan-head is mounted in SPM chamber beneath a liquid helium bath cryostat to allow experiments to be performed at low temperatures. It is surrounded by two concentric radiation shields. An optical access allows for a direct visual monitoring of the tip coarse positioning.

2.2 LT-SPM head

The SPM head follows the Besocke beetle-type design and delivers a very high thermal and mechanical stability, allowing to be operated in a temperature range from 5 to 300 K [45, 46]. For the measurement, the sample holder is clamped against the baseplate, on which three four-segment piezos are mounted. Each of these is carrying a sapphire ball on its top, supporting a 3-fold ramp ring made out of copper. By applying a suitable sawtooth voltage to the segments of the piezos, the ramp performs a motion relative to them in a stick-slip fashion. For the z coarse movement (up-down rotation) all piezos move tangentially, or parallel for the (x, y) coarse motion. (x, y, z) scanning is performed with the same piezo set. An additional ring of larger diameter surrounds the ramp preventing it from falling down by limiting its lateral range of motion. Figure 2.1 shows a graphical illustration and a photograph of a scanner.

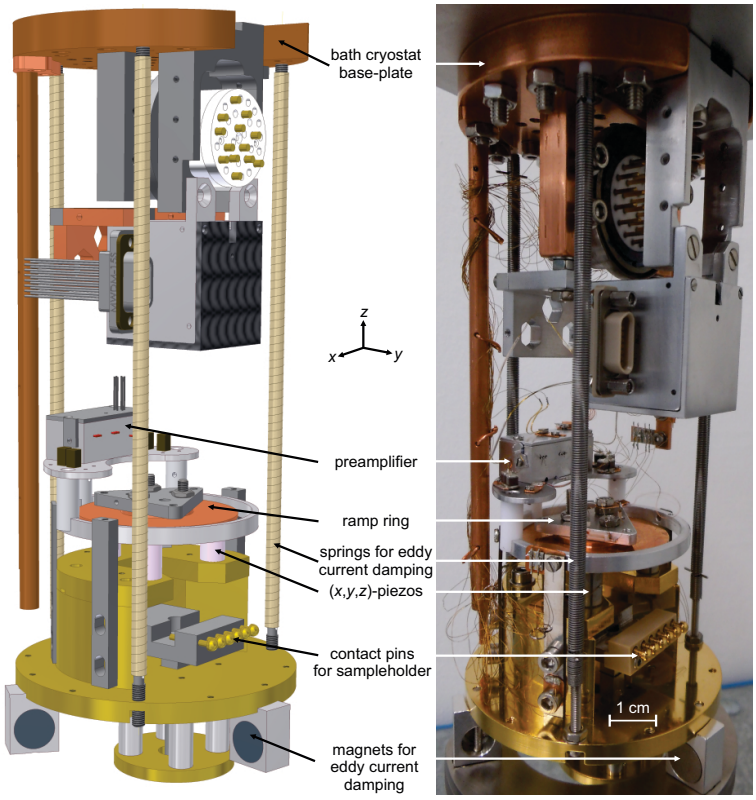

Figure 2.1: A sketch (on the left) and a photograph (on the right) of a STM/AFM scanner (built by Gerhard Münnich). It is Besocke beetle-type scanner suspended from springs attached to the liquid-He bath cryostat, which together with the magnets mounted at the bottom of the scan-head make an eddy current damping system. A preamplifier stage with installed amplifiers for both the current and deflection signal is mounted in proximity to the scanner to reduce electronic noise. From Ref. [44].

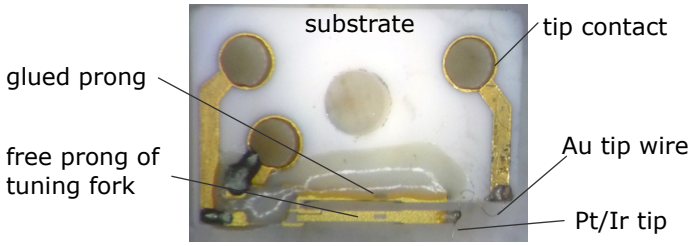

Figure 2.2: A photograph of the qPlus sensor. One prong of quartz cantilever (tuning fork) is glued to a ceramic substrate. On the quartz cantilever there are electrodes that collect the induced charges due to the mechanical strain caused by the deflection. A metal tip is glued to the free end of the prong and is connected via separate wire.

2.3 qPlus sensor

The heart of the microscope is a sensor, a quartz tuning fork mounted at the center of the ramp ring. The tuning forks are used in watch industry, and exploit the piezoelectric properties of quartz. Bending of the material induces uncompensated surface charges, which are collected by the attached electrodes. One prong of the tuning fork is glued to the ceramic substrate. The tip is glued to the second (free) prong and contacted via a separate gold wire such that the apparatus can be used as a combined STM and AFM. The oscillation of the tunning fork is actuated mechanically via excitation piezo mounted on a stack above the tuning fork. The sensor can be controlled to oscillate with amplitudes below Å because of its high stiffness. The deflection signal is converted into a voltage by means of a transimpedance amplifier mounted in the vicinity of the scanner, bandpass filtered and further adjusted in a voltage amplifier (SRS) before processed by the PLL controller. Our setup does not allow *in situ* sensor transfer.

The quality factor Q has a very high value, in 1-7 x 10^4 range, that minimizes the frequency noise and leads to an easy oscillations excitation. A typical value for the spring constant is $10^3\,\mathrm{N/m^{-1}}$ at a

resonance frequency of about 28 kHz. Except for the experiments in which the influence of the oscillation amplitude on the charging processes was investigated, the amplitude was set to be 0.5 Å giving the best trade-off between detection of short-range forces and sensitivity.

Many different A_{osc} are employed in experiments throughout chapter 4. It is therefore of great importance to first calibrate the oscillation amplitude correctly. For this, the sensor is oscillated at relatively large amplitudes (from 0.5 to 1.0 nm) in a constant current mode (that is, with the feedback turned on). Because of the exponential decay of the tunneling current with distance, the average tunneling current is dominated only by the contributions when the tip is closest to the surface (the lower turnaround point of the oscillation). In other words, two different oscillation amplitudes need two different tip-surface distances to maintain the same mean tunneling current. A change in the oscillation amplitude set point value will approximately linearly change the height of the tip. The obtained slope for the measured change in the tip height yields β, the conversion factor between the electrical cantilever signal (in voltage) and the real oscillation amplitude in units of length, e.g. Ångströms.

2.4 Metal substrates

In this thesis few different metal substrates are used for molecular self-assembly and insulating film growth. Details of the substrate preparation will be explained in a corresponding section that deals with the experiment performed on that specific substrate. Common for all of them is that they have to be atomically clean to allow identification of single molecules and allow them to arrange in supramolecular structures. For the substrates used here, to prepare them clean, it is sufficient to sputter the surface with ionized noble gas atoms for the appropriate time to remove the adsorbates and anneal afterwards

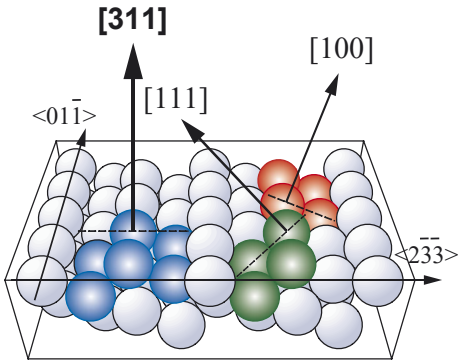

Figure 2.3: Ball-model representation of the Cu(311) surface. High-symmetry directions are indicated. Blue balls highlight the (311) unit cell. Green and red balls highlight the (111) and (100) unit cells, respectively. Image from Ref. [47].

to get large flat terraces. In the following, some basic properties of investigated samples: Cu(111), Cu(311), Ag(111) and Au(111) will be given.

The Cu(111) surface is obtained by cutting the (fcc) metal in such a way that the surface plane intersects the x-, y- and z- axes at the same value. Since this is the most efficient way of packing atoms within one layer, the surface is said to be "close-packed" (3-fold symmetry). The distance between the nearest neighbour atoms is 2.55 Å. The work function of Cu(111) is 4.95 eV.

Figure 2.3 shows a model of the Cu(311) surface. It is formed by two atomic lines width (111)-like terraces, separated by (100)-like steps. The distance between these intrinsic steps is d = 4.23 Å (terrace width: 3.68 Å). The work function of Cu(311) is 4.3 eV.

Silver is considered as a weak interacting substrate. It crystallizes with a lattice parameter of 4.085 Å, the next-neighbour distance in the closed-packed plane is 2.89 Å. As the Cu(111) surface, the Ag(111) surface supports a Shockley-type surface state (SSS) at -65 meV that

forms a two dimensional nearly free electron gas in the surface plane. Direct access to the surface state can be obtained by the $\mathrm{d}I/\mathrm{d}V$ spectroscopy, where the surface state onset is seen as an increase in the signal. The surface state is influenced by the present of adsorbates, defects and step edges: SSS electrons scatter and form interference patterns that are easily seen in STM images at low biases (electron standing waves) [48, 49]. Seufert *et al.* investigated the confinement of SSS electrons in quantum wells made in the molecular arrays of porphyrin as well as the interaction between the adjacent wells on Ag(111) [50]. $\mathrm{d}I/\mathrm{d}V$ spectroscopy has revealed that the onset shifts towards higher energies. Similar results were obtained in an earlier study by Morgenstern *et al.* where the confinement was studied in narrow steps of different widths of the Ag(111) surface [51]. The electrons could not be longer confined at the terraces if the width was smaller than $\lambda_F/2$, where λ_F is the Fermi wavelength for an infinitely large terrace.

Gold is an element that has a fcc crystal structure and the Au(111) surface is hexagonally packed with a lattice constant of 4.08 Å. It belongs to a small group of the fcc crystals that is characterized by a reconstruction, and the only element to show it for its (111) face. When imaged with STM, a long range structure can be observed, it is named $22\mathrm{x}\sqrt{3}$ or "herringbone" reconstruction. Discommensuration lines are of higher corrugation of about 0.03 nm because the top layer is compressed by 4.34 % in the closed-packed direction. The direction of these lines is along <112> and rotates by 120 ° which results in a typical zig-zag structures. The basic unit cell is two atomic rows wide (<100> direction) and every 22 lattice spacing in the <100> surface direction has two additional atoms. In total it contains 44 atoms in the bulk and 46 atoms in the surface layer (Figure 2.4). In the chapter 7 results of DFT calculations for covalently bounded structures adsorbed on Au(111) will be presented. There, the surface was approximated to be infinite and atomically flat fcc surface. Recently, F. Hanke and J. Björk performed DFT calculations to investigate atomic and electronic

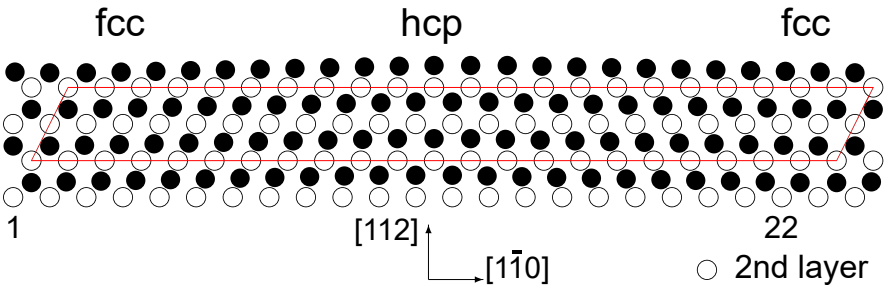

Figure 2.4: Schematic model of the reconstructed Au(111) surface with the herringbone lines, showing how 23 surface atoms fit into 22 lattice sites by compressing the top most layer of the surface. The stacking change from fcc to bridge to hcp to bridge and again to fcc. The largest portion of the surface can be associated with fcc alignment. The straight ridges (resulting from a buckling of the top Au layer between the fcc and hcp regions) are obvious features in any STM image of a clean Au(111) surface.

structure on reconstruction of the Au(111) surface. They showed that even though that studies in which the reconstruction is neglected overestimate the interaction energies, in majority of cases this does not result in a qualitative important change [52]. A schematic illustration of the Au(111) / 22x$\sqrt{3}$ reconstruction is given in Figure 2.4. The work function of Au(111) is 5.31 eV.

2.5 Ultrathin insulating films

To study adsorbates not perturbed by the metallic substrate, stable and atomically thin insulating films are required. Such films reduce the interaction and overlap of the wave functions, allowing for the imaging of molecular orbitals. Various thin films have been used as templates - oxide films are the most heavily investigated: A_2O_3 film on a NiAl(100) surface [53], PbO films on Pb(111) [54], and MgO [55–57]. In the group of B. Heinrich (later in the groups of J.

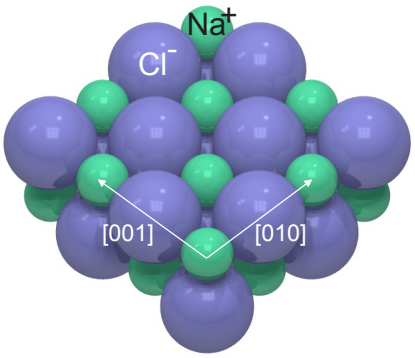

Figure 2.5: Ball-model of two layers NaCl(100). Image adapted from Ref. [75].

Gupta and C. F. Hirjibehedin) nitrides have been employed (CuN on Cu(100)) for investigation of spin related phenomena in single atoms and molecules [58–62]. Despited being only one layer thick, CuN has an insulating gap of about 4 eV [63]. Alkali halides can be deposited thermally, for example, NaCl can be grown reliably on Cu and Al surfaces no matter what surface orientation they have [64–67]. Also, epitaxial growth of NaCl on semiconductor surfaces has been shown for GaAs and Ge substrates [68, 69]. Electronic decoupling can be obtained not only by using these strongly polar materials, as layers of organic or noble gas molecules were demonstrated to be equally successful [70–74].

In the course of this thesis, adsorbates on NaCl grown on low-index Cu(111) and regularly stepped Cu(311) are investigated. A submonolayer or higher coverages of a few layers of NaCl crystal are deposited onto the sample from a homebuilt Ta crucible at a steady rate monitored with a quartz microbalance. On Cu(111), for a sample deposition temperatures close to room temperature and higher, the NaCl film grows as a bilayer with nonpolar step edges with smaller islands of third layers on top. There is a slight preference for orientations of this islands in which one of the polar directions is parallel to the closed-

packed directions of the Cu substrate, still, many different orientations of the NaCl island with respect to the Cu(111) exist. Different Moiré patterns can influence adsorption and diffusion of adsorbates [76]. The lattice constant of bulk NaCl at low temperatures used in our experiments is compressed by 2 % as compared to the value it has at room temperature (a = 5.64 Å). Once the Cu(111) surface is covered with a layer of NaCl the Cu(111) SSS band becomes *interface state band* and the band minimum shifts from 450 mV to about 230 mV below the Fermi energy [75].

On the Cu(311) substrate, the growth is different from the flat surfaces. For temperatures above 100 °C, a monoatomic islands are found before (for a coverages higher than 1 ML), the second-layer starts to grow. STM study has shown a strong substrate-film interaction: Cl^- ions are located above intrinsic steps which carry a positive charge due to the Smoluchowski smoothing effect [77], and Na^+ ions between them [78].

2.6 Manipulation of adsorbates

One part of this work will deal with the manipulation of adsorbed molecules. If the deposition of atoms or molecules is performed when the sample is at low temperature then they are usually fixed in place and the tip can be used to drag, push or pick up the adsorbates. The SPM is excellent tool for performing such tasks due to its sub-nanometer scale precision and high imaging resolution. A controlled manipulation of adsorbates has been performed for the first time by Don Eigler and his group at the IBM Almaden Research Center back in early age of STM, in 1990. They showed the reversible transfer of a Xe atoms from the surface to a tip. Nowadays, this process can be automated for individual atoms and small molecules [79]. Recently it was demonstrated how a kilobyte of memory can be written (and

rewritten) using chlorine vacancies in a chlorine-terminated Cu(100) surface [80].

Extending the vertical manipulation to large organic molecules we demonstrate controlled formation of quantum systems with desired geometry. Using the SPM tip we completely remove the selected molecules, patterning the self-assembled monolayer. Details will be given in chapter 5.

2.7 Tip functionalization

First successful manipulation of a CO molecule was performed in 1997 in the group of Prof. Rieder, FU Berlin [81]. Individual molecules were transfered from the Cu(111) surface to the apex of the tip by approaching the tip to the center of the molecule. Once on the tip, the attached molecule led to an enhancement of resolution in images recorded after the procedure. Such tips, where the last tip atoms are chemically modified, are called *functionalized*. In 2009, this method was applied to the FM AFM which yielded beautiful images of single pentacene molecules in a study by Gross *et al.* [82], and recently for imaging other molecules and products of chemical reactions (see chapter 7). Although a reliable procedure to pick and later release CO to the Cu(111) surface was demonstrated, it involves a complicated set of control sequence. Adsorption on NaCl islands or Au/Ag surface greatly facilitates pickup of molecules because of the reduced interaction with the substrate. It is usually sufficient to approach the molecule at low bias voltage for few Å before it hops to the tip apex. Although the CO molecules are the most widely used tip fuctionalization to date, other tip functionalizations have shown atomic resolution on molecules as well [83].

Interpretation of STM images obtained with functionalized tip is most of the time very difficult [84]. It is therefore important to prepare pure,

clean metallic tips for electronic structure characterization. For this, the tip is indented into the bare sample in order to coat it with surface atoms.

3 Apparent reversal of molecular orbitals reveals entanglement

Intramolecular electron-correlation effects are visualized by scanning probe microscopy on individual dicyanovinyl-substituted oligothiophene molecules. On NaCl/Cu(111) the molecules are neutral and the two lowest unoccupied molecular states are observed in the expected order of increasing energy. The sequence of the observed molecular orbitals is reversed on NaCl/Cu(311), where the molecules are negatively charged due to the lower work function of this surface. The experimental results, in open contradiction with a single-particle interpretation (SP), are explained by a many-body theory which predicts a strongly entangled doubly charged ground state.

3.1 Introduction

For the use of single molecules as devices, engineering and control of their intrinsic electronic properties is all-important. In this context, quantum effects such as electronic interference have recently shifted into the focus [85–91]. Most intriguing in this respect are electron correlation effects [92–98], which are intrinsically strong in molecules due to their small size [99–103].

In general, Coulomb charging energies strongly depend on the localization of electrons and hence on the spatial extent of the orbitals they occupy. It is therefore not surprising that the orbital sequence

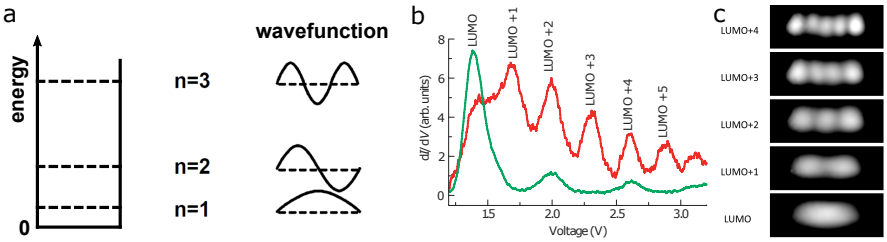

Figure 3.1: (a, left) Illustration of a one-dimensional particle-in-a-box model. The particle can move freely in the interior between the walls in constant, zero potential. This space is surrounded by barriers where infinitely large forces prevent the particle from escaping. Dashed lines are the allowed energy levels. (a, right) Initial wave functions for the first three states. (b) $\mathrm{d}I/\mathrm{d}V$ spectra measured at the center (green) and one end (red) of the oligothophene wire and (c) spatial distribution of these orbitals measured with STM (adapted from Ref. [109]). Increasing the energy, the number of nodal planes perpendicular to the longer molecular axis increases by one. Nodes are surfaces where the wave function has zero density.

of a given molecule can reverse upon electron attachment or removal, if some of the frontier orbitals are strongly localized while others are not, like it is the case in e.g. phthalocyanines [104–108]. Coulomb interaction may also lead to much more complex manifestations such as quantum entanglement of delocalized molecular orbitals and thus dominate the conductance properties.

In this chapter is shown, that the energy spacing of the frontier orbitals in a single molecular wire of individual dicyanovinyl-substituted quinquethiophene (DCV5T) can be engineered to achieve near-degeneracy of the two lowest lying unoccupied molecular orbitals, leading to a strongly-entangled ground state of $\mathrm{DCV5T}^{2-}$. These orbitals are the lowest two of a set of quasi particle-in-a-box-like states (Figure 3.1) and differ only by one additional nodal plane across the center of the wire. Hence, according to the fundamental oscillation theorem of the Sturm-Liouville theory their sequence has to be set with increasing

number of nodal planes, which is one of the basic principles of quantum chemistry [110, 111]. This is evidenced and visualized directly in real space from scanning tunneling microscopy (STM) and spectroscopy (STS) of DCV5T on ultrathin insulating films. Upon lowering the substrate's work function, the molecule becomes charged, which leads to a reversal of the sequence of the two orbitals. The fundamental oscillation theorem seems strikingly violated since the state with one *more* nodal plane appears *lower* in energy. This contradiction can be solved, though, by considering intramolecular correlation leading to a strong entanglement in the ground state of $DCV5T^{2-}$.

3.2 On the number of nodes of wave functions

Let's consider all orbitals of an isolated molecule and label them in increasing order of number of nodes as $\psi_1, \psi_2, \ldots, \psi_{n-1}, \psi_n, \ldots$ with their respective energies $\lambda_1, \lambda_2, \ldots$ The question we would like to answer is how many nodes the wave function ψ_n that corresponds to n^{th} energy level can have, and if the inequality $\lambda_{n-1} \leq \lambda_n$ will be true in general for every n and any molecule imaginable. Based on some arguments from the variational principle it can be shown that the ground state wave function has no nodes, but not to much can be said for the higher lying energy levels.

A mathematical theorem dealing with the number of nodes an eigenfunction that corresponds to a certain eigenvalue can have is called Courant's nodal line theorem (CNLT) and states that if eigenvalues of the elliptic equation $(\hat{L} + \lambda\rho(x))u(x) = 0$ are ordered according to increasing eigenvalues, then the nodes of the n^{th} eigenfunction divide the domain D into no more than n subdomains. $L = L(\Delta, x)$ is a linear, self-adjoint differential operator on a domain D with homogeneous boundary conditions $u(x) = 0$, $\rho(x)$ is positive and bounded and λ is the eigenvalue. The nodal set of $u(x)$ is defined as the set of points x such that $u(x) = 0$. The subdomains are called *nodal domains*, or

sign domains as $u_n(x)$ has one sign in the interior, separated by the nodes, or zeros, of eigenfunctions of L.

In other words, CNLT states that if we order the possible energy eigenvalues λ_i in the increasing order, then the n^{th} eigenfunction ψ_n, has **at most** n nodes, thus providing us only on an upper bound for the number of nodes a wave function may have. We only know that the ground state wave function ψ_1 cannot have any nodes within the region D. Wave functions for higher n may possess up to $n-1$ nodes within D but may as well have less. Therefore, we cannot know in all certainty if a wave function that has more nodes than another one will automatically correspond to a state with higher energy.

How many nodes and how these are distributed for ordinary second-order differential equations with homogeneous boundary conditions is the subject of Sturm-Liouville theory. It is a very special case of CNLT: we can strengthen it such that if we order the eigenvalues as $\lambda_1 \leq \lambda_1 \leq \lambda_3 \leq ...$, then the n^{th} eigenfunction corresponding to energy eigenvalue λ_n, has precisely n nodes. The **one-dimensional time-independent Schrödinger equation** in the coordinate representation can be also seen as Sturm-Liouville differential equation. In this case it is always true that a wave function with less nodes must always correspond to a state of lower energy than a wave function with more nodes. So, the wave functions of the one-dimensional particle-in-a-box must obey this rule. In the case of the time-dependent equation, like for the three-dimensional particle-in-a-box (generally for the systems of many degrees of freedom), this is not true anymore since it is a partial differential equation and the former is an ordinary differential equation.

Although these theorems give the answer on the number of zeros differential equation can have and are extremely important for the quantum mechanics, they are rarely part of the standard textbooks.

3.3 Methods

The Cu(111) and Cu(311) single-crystal samples were cleaned by several sputtering and annealing cycles. NaCl was evaporated thermally so that defect-free, (100)-terminated NaCl islands with few atomic layers were formed [78, 112]. DCV5T molecules were deposited onto the cold sample (below 10 K) inside the STM. Bias voltages are applied to the sample. All AFM data, $\mathrm{d}I/\mathrm{d}V$ spectra and maps were acquired in constant-height mode.

Calculations of the orbitals and effective single-particle electronic structure were performed in the framework of this thesis within the density functional theory as implemented in the SIESTA code [113] and are based on the generalized gradient approximation (GGA-PBE). We used a plane-wave cutoff of 600 Rydbergs and a double-ζ plus polarization basis set to describe the valence electrons. The atomic structure optimization was carried out until force tolerance on all atoms of 0.04 eV/Å was reached.

Our collaborators from the Institute of Theoretical Physics, University of Regensburg, modelled the many-body physics. Here, some details of their methodology is given: The many-body eigenstates are determined from a diagonalization of the many-body model Hamiltonian H_{mol}, which is defined further below in the text. Based on these, STM-image and spectra simulations were performed within a Liouville approach for the density matrix ρ. The dynamics of the STM junction is described by transitions between molecular many-body eigenstates and it is calculated *via* a generalized master equation $\dot{\rho}_{\mathrm{red}} = \mathcal{L}\rho_{\mathrm{red}}$ for the reduced density operator $\rho_{\mathrm{red}} = \mathrm{Tr}_{\mathrm{Sub,Tip}}(\rho)$ [114–116], where $\mathcal{L}$ is the Liouvillean superoperator. The coupling to the metallic substrate and the tip has been treated perturbatively and retained within the lowest nonvanishing order (sequential tunnelling approximation).

3.4 Engineering electronic structure of a molecular wire

The molecular structure of DCV5T, shown in Fig. 3.2b, consists of a quinquethiophene (5T) backbone and a dicyanovinyl (DCV) moiety at each end of the molecular wire. The delocalized electronic system of polythiophene and oligo-thiophene enables conductance of this material [117–119]. The lowest unoccupied orbital of each of the thiophene rings couples electronically to its neighbors and forms a set of particle-in-a-box-like states [109, 120]. The LUMO to LUMO+1 level spacing of the quinquethiophene (5T) backbone is $\approx 0.7\,\mathrm{eV}$ [109], which is in good agreement with the energy difference calculated for the free 5T molecules based on DFT, as shown in Fig. 3.2a. This DFT-based calculation also confirms the nature of the LUMO and LUMO+1 orbitals, both deriving from the single thiophene's LUMOs and essentially differing only by one additional nodal plane across the center of the molecule. To enable the emergence of correlation and thus level reordering, we have to bring these two states closer to each other. This can be achieved by substituting dicyanovinyl moieties with larger electron affinity at each end of the molecular wire. As the orbital density of the higher lying particle-in-a-box-like state, namely LUMO+1, has more weight at the ends of the molecule, it is more affected by this substitution than the lowest state, the LUMO. This is evidenced by corresponding calculations of DCV5T, for which the LUMO to LUMO+1 energy difference is reduced by more than a factor of two, see Fig. 3.2b. The increased size of the delocalized system in the case of DCV5T may also play a role in the reduced level spacing, however, as the spacing between LUMO+1 and LUMO+2 barely changes upon DCV substitution, this effect appears to be minor. For the rest of this work, we concentrate on the LUMO and LUMO+1 orbitals only. To avoid confusion, we refrain from labeling the orbitals according to their occupation and sequence but instead refer to them according to their symmetry with respect to the mirror plane perpen-

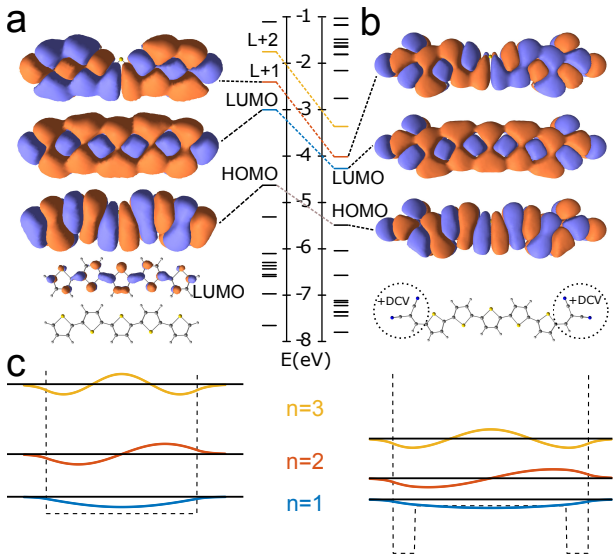

Figure 3.2: Molecular structure and density-functional theory based calculations of the electronic structure of 5T (panel a) and DCV5T (panel b). The bottom most part of both panels depicts the molecular structure, whereas the others show the calculated orbitals and energies for the HOMO, LUMO and LUMO+1 as indicated. The orbitals are depicted as contours of constant probability density. Relatively low values of constant probability density have to be used to match the experiment at low tunneling currents. For reference, the LUMO of 5T is also shown at a contour of larger probability density. The LUMO and LUMO+1 orbitals in both cases derive from the thiophene subunit's LUMO. They are the lowest two of a set of particle-in-a-box-like states and differ only by one additional nodal plane. Whereas the LUMO to LUMO+1 energy difference is $\approx 0.7\,\mathrm{eV}$ for 5T, this difference is drastically reduced in the case of DCV5T. The basic principle of level engineering adopted in DCV5T is illustrated for a one dimensional quantum box in panel c.

dicular to the molecular axis, as symmetric (S) and antisymmetric (AS). Hence, the former LUMO and the LUMO+1 are the S and AS states, respectively.

3.5 Reversal of the molecular orbital sequence

To study the energetic alignment of the orbitals as well as their distribution in real space, we employ ultrathin NaCl insulating films to electronically decouple the molecules from the conductive substrate [121]. It has been previously shown that in these systems the work function can be changed by using different surface orientations of the underlying metal support [78, 122, 123]. Importantly, this does not affect the surface orientation of the NaCl film, it still remains (100)-terminated, such that the local chemical environment of the molecule remains the same, except for the overall change of the work function.

However, in the present case, this alone has a dramatic effect on the electronic structure of the molecular wires as is evidenced in Fig. 3.3. There, the STM images are shown for voltages corresponding to the respective lowest lying molecular resonances at positive sample voltage for DCV5T adsorbed on NaCl/Cu(111) (panel a) and NaCl/Cu(311) (panel b). They both show a hot-dog like appearance of the overall orbital density as was observed and discussed previously [109, 124]. Importantly in the current context, however, the orbital density of DCV5T/NaCl/Cu(311) shows a clear depression at the center of the molecule, indicating a nodal plane, whereas DCV5T/NaCl/Cu(111) does not. Apparently, the energetically lowest lying state is not the same for the two cases, but S for DCV5T/NaCl/Cu(111) and AS in the case of DCV5T/NaCl/Cu(311). In contrast, STM images acquired at voltages well below the first resonance reflect the geometry of the molecule in both cases as wire-like protrusion (see insets of Fig. 3.3).

In previous studies of molecules on insulating films it was observed that, due to the electronic decoupling by the film, the molecular levels are roughly aligned with the vacuum level. From an electrochemical characterization the electron affinity of DCV5T in solution was determined to be at $-3.73\,\mathrm{eV}$ relative to the vacuum level [119]. The polarizability of the solution lowers the electron affinity level, such that

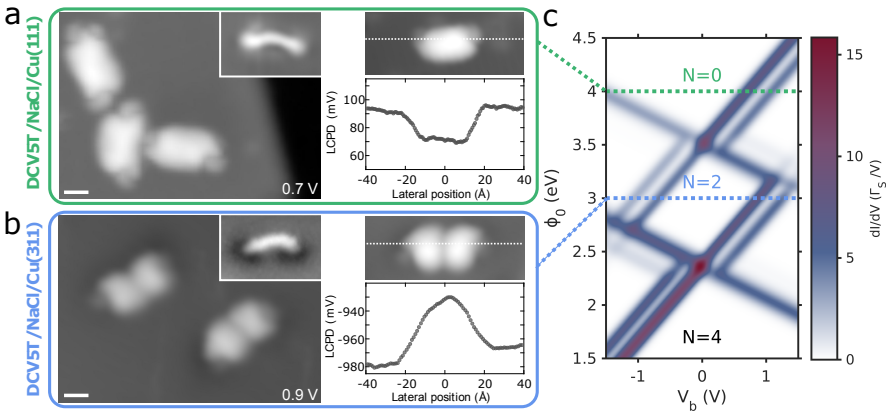

Figure 3.3: (a and b, left) STM images of the first DCV5T electronic resonance for NaCl/Cu(111) (a) and NaCl/Cu(311) (b) as substrates (Insets show corresponding STM images at voltages below the first molecular resonance). (a and b, right) Local contact potential difference across the molecule for NaCl/Cu(111) (a) and NaCl/Cu(311) (b) as substrates. (c) Stability diagram for DCV5T as a function of substrate work function and bias across the junction. The equilibrium particle numbers are indicated within the low conductance diamonds. The upper and lower dashed lines correspond to the NaCl/Cu(111) and NaCl/Cu(311) substrates, respectively. Imaging parameters: (a) $V = 0.8\,\mathrm{V}$, $I = 0.1\,\mathrm{pA}$. Inset $V = 0.2\,\mathrm{V}$, $I = 0.28\,\mathrm{pA}$. (b) $V = 0.9\,\mathrm{V}$, $I = 2.4\,\mathrm{pA}$. Inset $V = 0.3\,\mathrm{V}$, $I = 2.4\,\mathrm{pA}$. Scale bar 1 nm.

here the LUMO transport level can be expected at some tenths of an eV higher in energy. Considering the work function of NaCl/Cu(111) of about 4 eV [64, 121], this expectation in good agreement with the experimentally observed position of the S state for this system.

We hence assume that the molecules are neutral on NaCl/Cu(111) and that the S state corresponds to the LUMO. According to the literature, changing the copper surface orientation from Cu(111) to Cu(311) results in a lowering of the work function by approximately 1 eV [78, 112, 125]. Hence, one may expect that the former LUMO, initially located 0.7 eV above the Fermi level E_F in the case of NaCl/Cu(111)

will shift to below the Fermi level [108, 123] for NaCl/Cu(311) such that the molecule becomes permanently charged.

To analyze that, we performed KPFS measurements along the molecules for both substrates, as is shown in Figs. 3.3a and b. From a fit to the parabolic shape of the frequency shift $\Delta f(V)$ as a function of sample voltage V, the local contact potential difference (LCPD) between tip and sample [29, 37, 126, 127] is extracted. Next to the molecules, on the clean NaCl films, the LCPD differs by slightly more than 1 eV for the two systems providing a rough estimate of the work function difference for the two systems in accordance with literature values [78, 112, 125]. Since local surface charges and dipoles affect the LCPD above adsorbates, the latter should qualitatively reflect the charge state [128, 129], the electron affinity [130], and the charge distribution [127, 131]. The decrease of about 20 meV in LCPD over the molecule in the case of DCV5T/NaCl/Cu(111) we assume to be due to the large electron affinity of DCV5T. On the NaCl/Cu(311) substrate the observed increase of LCPD is consistent with an anionic state of DCV5T/NaCl/Cu(311) [132]. As will be substantiated further below, in agreement with a model including electronic correlations, we suggest that on NaCl/Cu(311) DCV5T is even doubly charged (Fig. 3.3c).

To obtain a systematic understanding of the level alignment of the S and AS states of the molecule on both substrates, we acquired differential conductance ($\mathrm{d}I/\mathrm{d}V$) spectra and $\mathrm{d}I/\mathrm{d}V$-maps on DCV5T molecules. Typical spectra measured at the center and the side of the molecule are shown in Figs. 3.4a and b on NaCl/Cu(111) and NaCl/Cu(311), respectively. DCV5T exhibits two $\mathrm{d}I/\mathrm{d}V$ resonances at positive bias but none at negative voltages down to -2.5 V. According to the $\mathrm{d}I/\mathrm{d}V$ maps and consistent with the different intensities in the spectra acquired on and off center of the molecule, the S state at $\simeq 0.7$ V is lower in energy than the AS state occurring at $\simeq 1.1$ V. The energy difference of $\simeq 0.4$ eV is in rough agreement to our calculations (see Fig. 3.2b). Fig. 3.4a also shows the corresponding

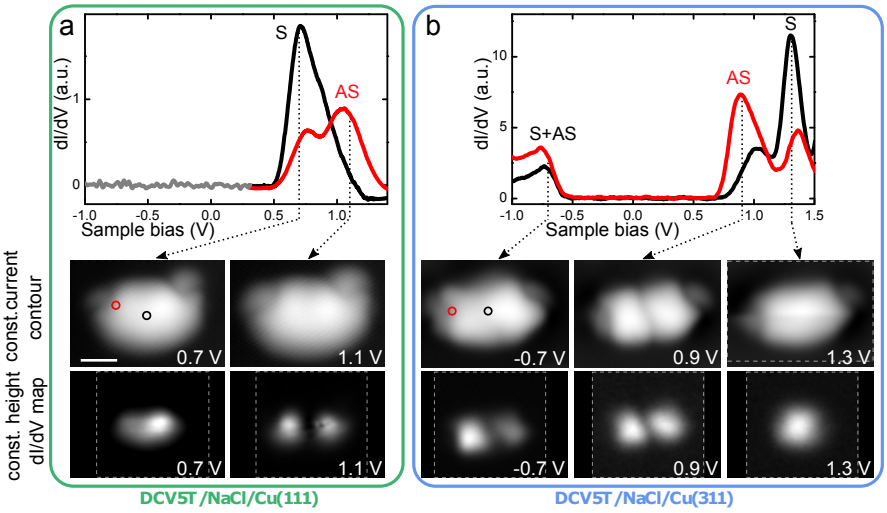

Figure 3.4: $\mathrm{d}I/\mathrm{d}V$ spectra (top panels), constant-current STM images (center panels) and $\mathrm{d}I/\mathrm{d}V$ maps (bottom panels) on the individual molecule DCV5T on NaCl/Cu(111) (a) and NaCl/Cu(311) (b) respectively. The resonances are labelled with S and AS, referring to resonances of the symmetic and antisymmetric states, respectively. $\mathrm{d}I/\mathrm{d}V$ spectra were recorded on (black) and off (red) the center of the molecule as indicated by dots in the constant-current STM images, using lock-in detection. To not miss any small $\mathrm{d}I/\mathrm{d}V$ signals in the low-bias range, a corresponding spectrum (grey) was measured at different set-point values such that the tip was $\simeq 2\,\text{Å}$ closer to the surface compared to the other two spectra (red and black). All spectra were slightly low-pass filtered. The negative differential conductance beyond the AS peak (black curve) can be attributed to the increase in the tunneling barrier height with increasing bias voltage [121]. The images are resized to have the same size and scale, whereby the area of measured data is indicated with white dashed rectangles. Imaging parameters for constant current images: (a and b) $I = 2.4\,\text{pA}$, bias voltage as indicated. Scale bar 1 nm.

constant-current STM images at voltages corresponding to the resonances. Whereas the one acquired at 0.7 V reflects the S shape, the one at 1.1 V seems to be a superposition of the S and AS states. This is expected since in the former and the latter case the bias voltage window includes only the S and both states, respectively. As discussed above, in the case of NaCl/Cu(311), DCV5T exhibits the AS state as the lowest resonance at positive bias voltages, this time at $\simeq 0.9$ V. This is additionally evidenced by the constant-current STM image and the corresponding $\mathrm{d}I/\mathrm{d}V$ map in Fig. 3.4b. The S state is now located at higher voltages, namely at $\simeq 1.3$ V, as seen in the spectrum and the $\mathrm{d}I/\mathrm{d}V$ map. Obviously, the two states are reversed in their sequence. In this case, at negative bias voltages, a peak in $\mathrm{d}I/\mathrm{d}V$ indicates an occupied state in equilibrium, in stark contrast to DCV5T/NaCl/Cu(111) but in agreement with the assumption of the molecule being negatively charged. The constant-current image acquired at -0.7 V, corresponding to the first peak at negative bias, seems to be also a superposition of both the S and AS states.

3.6 Failure of a single-particle picture description

Next, we will discuss why a single-particle picture fails to account for the orbital reversal. In contrast to optical spectroscopy where excitation energies are measured for a molecule with fixed number of electrons, in scanning tunneling spectroscopy an electron temporary tunnels into the unoccupied orbital, or is removed from the already occupied one: *transitions* from an initial state of N electrons to final states with $N \pm 1$ electrons are detected. In the DBTJ geometry employed here, the resonances in $\mathrm{d}I/\mathrm{d}V$ are associated with this temporary change of electron number on the molecule. In this terms the two peaks of DCV5T/NaCl/Cu(111) at positive bias are DCV5T$\leftrightarrow$DCV5T$^-$ transitions (See Figure 3.5A), and, in the same spirit, the ones of DCV5T/NaCl/Cu(311) at positive and at negative

bias should be interpreted as DCV5T^{2-} $\leftrightarrow$DCV5T^{3-} and DCV5T^{2-} $\leftrightarrow$ DCV5T^{-} transitions, respectively. The initial state is assumed to be the ground state as the experiments are conducted at low temperature, while the final state can be one of the excited states. In the single-particle picture, the final states are obtained by sequential filling (emptying) of the ground state orbitals with increasing (decreasing) order of energy. However, some very important effects are neglected: the reordering of the molecular orbitals (in SP one would expect only an equal shift in energies for all observed resonances after charging) due different charging energies and correlation effects (electron exchange). In Figure 3.5 all possible scenarios are discussed to portray discrepancies between the experimental data and the single-particle theory. Our experiments suggest a strong modification of the electronic structure that can be explained by going beyond this simplified picture and accounting for the response to the tunneling electons.

3.7 Basics of many-body theory

When the interaction between the particles is weak, then they can be considered to act independently. However, when the interaction is strong, the quantum state is not any more separable, hence, the system has to be treated in its entirely. Although there are several examples of many-body effects investigated in solid-state systems (such as high T_c superconductors) [133] and some theory calculations predicting orbital mixing due to electronic correlations, only one example of experimental observation with STM in molecular systems exists [102]. Usually, in the interpretation of spectra and images in the STM these effects are neglected and the results are explaned in terms of single-partice non-interacting orbitals, which is the topic of the previous section 3.6.

Even the simplest and smallest molecules consist of a large number of particles making an attempt to schematically display all possible

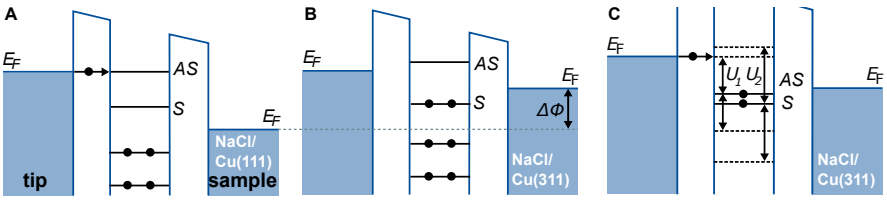

Figure 3.5: Illustration of a DBTJ in the single-particle picture and its failure to describe the experimental observations. (A) On NaCl/Cu(111) the molecules are neutral and the S and AS states become available for tunneling in their respective order. This is in agreement with the observations. (B) Changing the surface orientation to (311) lowers the work function by $\Delta\Phi$. The former LUMO shifts below the Fermi level of the substrate, and the molecule becomes charged. The additional electron(s) interact with other electrons which lead to shifting of the molecular orbitals e.g. the occupied states are not any more at the same energies. The first peak at the positive voltage should correspond to the AS state of the neutral molecule, but next-lowest transition should be detected as S, which is not in agreement with the model proposed as this state becomes available only for electron removal. (C) As a result of electronic screening and/or relaxation in the molecule and the film, both S and AS are shifted across the Fermi level and are singly charged. Charging energy U is required to put additional electron on the molecule. For the S state, this energy U_2 has to be considerably larger than U_1, if the S state is to be found at higher energy with respect to the AS state, however, this is inconsistent with the resonance (the superposition of both S and AS states) that appears at the negative bias. This contradiction will be solved by considering intramolecular correlation and strong entanglement in the ground state of doubly negative charged molecule.

electron configurations almost an impossible task. One elegant way to do this is by assigning many-body state to a discrete total energy of the whole system. This enables a simple and clear visual depiction of all electrons and their spin, and allows for a direct comparison between them. An example is given in Figure 3.6 for a system consisting of three electrons in equilibrium and after a single negative charge is introduced. Adding an extra electron changes the total number of particles in the molecule which consequently alters the total energy.

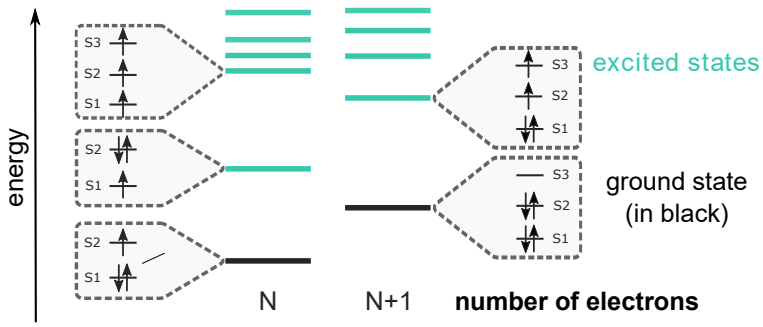

Figure 3.6: Sketch of many-body spectrum with occupations of first few lowest-lying states (the ground states are in black). As many-body states can be classified according to the different number of electrons, these are displayed in different columns. Arrows represent electrons.

The equilibrium state will be called *neutral ground state*, whereas all states with the same number of electrons as the ground state but lying energetically higher will be referred to as neutral excited states. The lowest lying state with one additional negative charge will be named the anionic ground state, and all energetically higher lying states in the same vertical column, anionic excited states. In the same manner, the labeling can be extended to the cationic, bianionic states etc. Getting familiar with this notation is important in order to understand the graphical depictions used in the remainder of this chapter.

In the next section we will invoke the role of electronic correlations to understand the orbital reversal.

3.8 The entanglement of the two particle ground state

Both the topographical and the spectroscopic data presented so far suggest that the electronic transport through DCV5T involves, in the

present bias and work function ranges, only the symmetric (S) and the antisymmetric (AS) orbitals. We concentrate on them and freeze the occupation of the other lower (higher) energy orbitals to 2 (0). In terms of these S and AS *frontier* orbitals we write the minimal interacting Hamiltonian for the isolated molecule,

$$\begin{aligned} H_{\mathrm{mol}} =& \epsilon_{\mathrm{S}}\hat{n}_{\mathrm{S}} + \epsilon_{\mathrm{AS}}\hat{n}_{\mathrm{AS}} + \frac{U}{2}\hat{N}(\hat{N}-1) \\ &+ J\sum_{\sigma\sigma'} d^{\dagger}_{\mathrm{AS}\sigma} d^{\dagger}_{\mathrm{S}\sigma'} d_{\mathrm{AS}\sigma'} d_{\mathrm{S}\sigma} \\ &+ J\left(d^{\dagger}_{\mathrm{AS}\uparrow} d^{\dagger}_{\mathrm{AS}\downarrow} d_{\mathrm{S}\downarrow} d_{\mathrm{S}\uparrow} + d^{\dagger}_{\mathrm{S}\uparrow} d^{\dagger}_{\mathrm{S}\downarrow} d_{\mathrm{AS}\downarrow} d_{\mathrm{AS}\uparrow}\right), \end{aligned} \tag{3.1}$$

where $d^{\dagger}_{\mathrm{S(AS)}\sigma}$ creates an electron with spin σ in the symmetric (antisymmetric) orbital, $\hat{n}_{\mathrm{i}}$ counts the number of electron in the orbital with $\mathrm{i} = \mathrm{S}, \mathrm{AS}$ and $\hat{N}$ represents the total number of electrons occupying the two frontier orbitals. The interaction parameters $U = 1.4$ eV and $J = 0.75$ eV are estimated from the DFT orbitals by direct calculation of the associated Coulomb integrals and assuming a dielectric constant $\epsilon_r = 2$ which accounts for the screening introduced by the underlying frozen orbitals [103, 134]. As expected from their similar (de-)localization, the Coulomb integrals of the S and AS states are almost identical.

Besides a constant interaction charging energy U, the model defined in Eq. (3.1) contains exchange interaction and pair-hopping terms, both proportional to J, which are responsible for the electronic correlation. The electrostatic interaction with the substrate is known to stabilize charges on atoms and molecules [122, 135, 136] due to image charge and polaron formation. We account for this stabilization with the additional Hamiltonian $H_{\mathrm{mol-env}} = -\delta\hat{N}^2$ The orbital energies $\epsilon_{\mathrm{S}} = -3.1\,\mathrm{eV}$ and $\epsilon_{\mathrm{AS}} = -2.8\,\mathrm{eV}$ as well as the image-charge renormalization $\delta = 0.43\,\mathrm{eV}$ are estimated from the experimental resonances of the neutral molecule and previous experimental results on other molecules

Depending on the work function ϕ_0 of the substrate DCV5T can become permanently charged in its ground state, as observed experimentally. To account for that, the grand canonical Hamiltonian, reading $H_{\mathrm{mol}} + H_{\mathrm{mol-env}} + \phi_0 \hat{N}$, has to be considered. The spectrum of this Hamiltonian, providing the energies $E_{N,m}$ of the m-th excited many-body state with N particles, can be used to calculate a stability diagram, Fig. 3.3c, known from quantum-dot science [137], as well as the many-body energy diagram shown in Fig. 3.7.

Many-body interaction manifests itself most strikingly for the ground state $\mathrm{DCV5T}^{2-}$, which will therefore be discussed at first. Consider the two many-body states, in which the two extra electrons both occupy either the S or the AS state: They differ in energy by the energy 2Δ, where $\Delta = \epsilon_{\mathrm{AS}} - \epsilon_{\mathrm{S}}$ is the single-particle level spacing between the S and the AS state. These two many-body states interact *via* pair-hopping of strength J, leading to a level repulsion. As long as $\Delta \gg J$, this effect is negligible. In DCV5T, though, the single-particle level spacing Δ is small compared to the pair-hopping J, leading to an entangled ground state of $\mathrm{DCV5T}^{2-}$ as

$$|2,0\rangle = \cos\theta \, d^{\dagger}_{\mathrm{S}\uparrow} d^{\dagger}_{\mathrm{S}\downarrow} |\Omega\rangle + \sin\theta \, d^{\dagger}_{\mathrm{AS}\uparrow} d^{\dagger}_{\mathrm{AS}\downarrow} |\Omega\rangle, \quad \text{with} \quad \theta = \frac{\arctan\left(J/\Delta\right)}{2} \tag{3.2}$$

where $|\Omega\rangle$ is the ground state of neutral DCV5T. Note that here, as $J/\Delta \approx 2.6$, this state shows more than 30% contribution from both constituent states, is strongly entangled, and therefore it can not be approximated by a single Slater determinant. The first excited state of $\mathrm{DCV5T}^{2-}$ is a triplet with one electron in the S and one in the AS orbital at about 54 meV above the ground state, as shown in Fig. 3.7.

The level repulsion in $\mathrm{DCV5T}^{2-}$ mentioned above leads to a significant reduction of the ground state energy by more than $J - \Delta$. This effect enhances the stability of the doubly charged molecule to the disadvantage of $\mathrm{DCV5T}^{-}$, which has just a single extra electron and therefore does not feature many-body effects. Quantitatively, this is

captured by the addition energies $E_N^{\mathrm{add}} = E_{N+1,0} - 2E_{N,0} + E_{N-1,0}$ being a measure of the stability of the N particle ground state. For DCV5T$^-$ and DCV5T^{2-} they read, respectively:

$$\begin{aligned} E_1^{\mathrm{add}} &= U - 2\delta + \Delta - \sqrt{\Delta^2 + J^2}, \\ E_2^{\mathrm{add}} &= U - 2\delta - \Delta - J + 2\sqrt{\Delta^2 + J^2}, \end{aligned} \tag{3.3}$$

For $U \gg \Delta \gg J$ the charging energy U dominates the spectrum as in a metallic quantum dot. Level quantization already shows up for $U \approx \Delta \gg J$ but the lower bound of the charging energies still remains U. In DCV5T, though, J is comparable to U and larger than the level spacing Δ – a regime, in which the addition energies E^{add} can even shrink to zero or get negative. This renders DCV5T$^-$ quite unstable and a small work function variation brings it towards the neutral or the doubly charged state as shown in the stability diagram of Fig. 3.3c.

Within the framework of the many-body theory, as sketched in Fig. 3.7, the apparent orbital reversal between Fig. 3.4a and Fig. 3.4b is naturally explained. To this end, as mentioned above, tunneling events in the STM experiments have to be considered as *transitions* between the many-body states of different charges N (see arrows in Fig. 3.7). The spatial fingerprints of the transitions and hence their appearance in STM images is given by the orbital occupation *difference* between the two many-body states and is indicated by the labels S and AS in Fig. 3.7.

When on NaCl(2ML)/Cu(111), the DCV5T molecule is in its neutral ground state, see green panel in Fig. 3.7 and Fig. 3.3. A sufficiently large positive sample bias triggers transitions to the singly charged DCV5T$^-$: The S and AS transitions subsequently become energetically available in the expected order of the corresponding single-particle states. A fast tunnelling of the extra electron to the substrate restores the initial condition enabling a steady-state current.

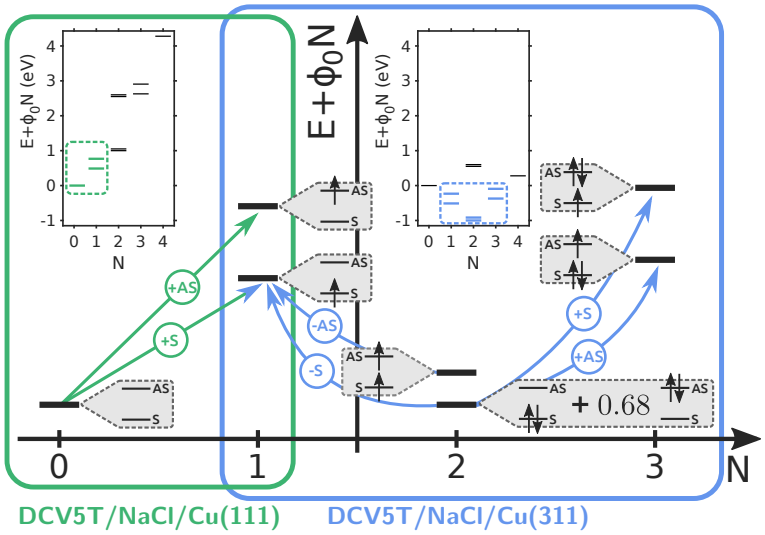

Figure 3.7: Scheme with the many-body transitions associated to the measured resonances. In the green framed panel the transition between the neutral and the singly charged DCV5T^{-} are illustrated (DCV5T/NaCl(Cu(111)). In the blue framed panel the transitions involving DCV5T^{-}, DCV5T^{2-} and DCV5T^{3-} are analyzed (DCV5T/NaCl(Cu(311)). The electronic structure associated to the different many-body states is explicitly given in the gray labels. In the insets, the many-body spectra of the molecule on the two corresponding substrates are plotted.

When on NaCl(2ML)/Cu(311) the molecule is doubly charged and in the entangled ground state described by Eq. (3.2), see Fig. 3.7. At sufficiently high positive sample bias the transitions to DCV5T^{3-} are opening, enabling electron tunnelling from the tip to the molecule. The topography of these transitions is again obtained by comparing the 2 and the 3 (excess) electron states of DCV5T (cf. Fig. 3.7). The transition to the 3 particle *ground* state occurs by the population of the AS state and it involves the *first* component of the entangled 2 electron ground state only. The second component cannot contribute to this transition, which is bound to involve only a *single* electron

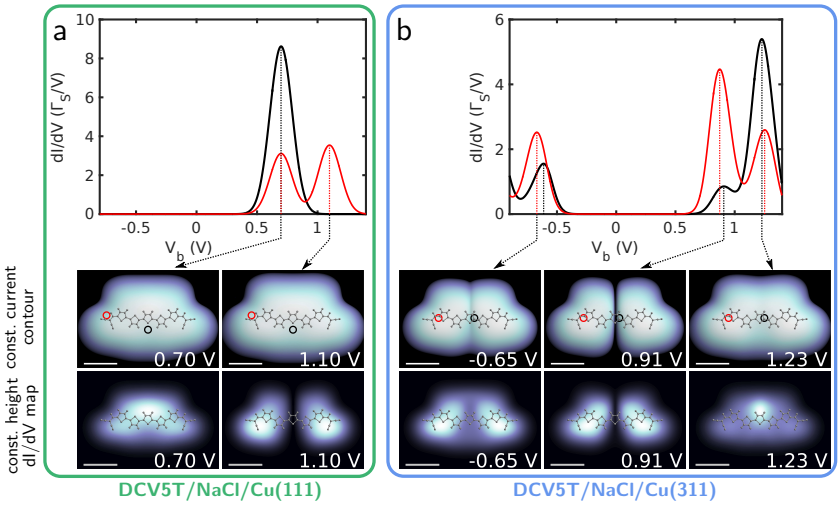

Figure 3.8: Theoretical simulations of dI/dV spectra (top panels), constant-current STM images (center panels) and dI/dV maps (bottom panels) on the individual molecule DCV5T on NaCl/Cu(111) (a) and NaCl/Cu(311) (b) respectively. dI/dV spectra were recorded on (black) and off (red) center of the molecule as indicated by dots in the constant-current STM images.

tunneling event. Correspondingly, at a larger bias the *first excited* 3 particle state becomes accessible, *via* a transition involving the *second* component of the 2 particle ground state only. This transition has a characteristic S state topography. Hence, although the electronic structure of the 3 electron states does follow the Aufbau principle, the entanglement of the 2 particle ground state leads to the apparent reversal of the orbital sequence.

As described in the methods paragraph, in addition to the many-body spectrum the full dynamics of subsequent tunneling processes for all relevant situations was calculated, resulting in the calculated dI/dV characteristics, constant current maps and constant height dI/dV maps for a DCV5T single molecule junction presented in Fig. 3.8. A qualitative agreement with the experimental results of Fig. 3.4 can

be observed both for the relative strength of the spectral peaks and the $\mathrm{d}I/\mathrm{d}V$ maps. The above discussed apparent orbital reversal is fully confirmed by the calculations.

The experimental data of DCV5T on the Cu(311) substrate at negative bias also show a non-standard feature. The $\mathrm{d}I/\mathrm{d}V$ map at resonance resembles a superposition of the S and AS orbital, see Fig. 3.4b. The effect is also reproduced in the theoretical simulations presented in Fig. 3.8. This can be rationalized in terms of a non-equilibrium dynamics associated to a population inversion recently predicted [103]. The transition between the 2 and the 1 particle ground states has the topography of a S orbital. Its close vicinity to the ground state implies that also the two particle first excite state should participate to transport. Moreover, the transition which connects the latter to the 1 particle ground state vanishes if the tip is in the vicinity of the molecular center, thus producing a nodal plane in the $\mathrm{d}I/\mathrm{d}V$ topography and a large population of the 2 particle excited state. Though, this non-equilibrium induced population inversion is in competition with relaxation processes which conserve the molecular charge. This experiment indirectly proves that, although not negligible, this relaxation is by far not the fastest process for STM on thin insulating films: In the opposite case the nodal plane at the negative bias resonance would not have been observed.

3.9 Assignment of the charge state by the shift of the resonance peaks

The thickness of the insulating layer grown on metal substrates can serve as a parameter to modulate the electronic properties of the supported adsorbates [57]. That is, by tuning the number of layers the most stable charge state can be found, or such a phenomenon, like the charge bistability can be observed [123]. This is related to a change

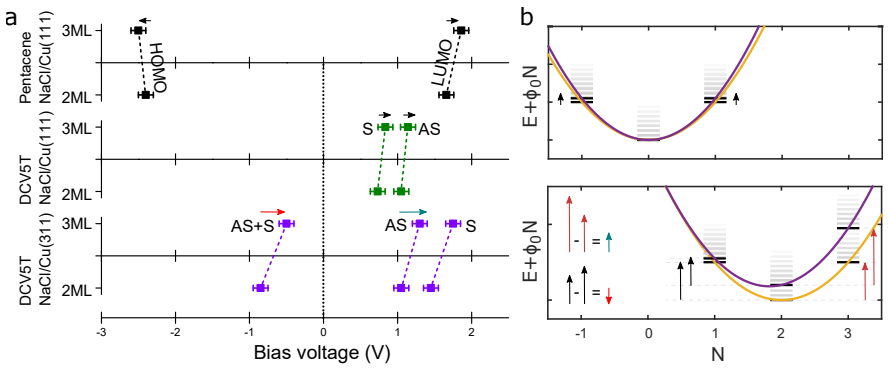

Figure 3.9: (a) Measured orbital energies (occupied and unoccupied) for pentacene and DCV5T molecule as a function of the number of NaCl layers and the substrate's chemical potential. The occupied molecular resonances have different functional dependence on bias voltage, for differently charged species. (b) Simplified sketch of the many-body spectrum of DCV5T for the bilayer and trilayer. Cationic, neutral, mono-, bi- and tri-anionic low-energy parts of the spectrum are shown (relative position of states is not derived from calculations and excited spectrum (in grey) is for demonstration purposes only).

in the electronic screening of the underlying metallic substrate when a number of layers is varied. To explore this effect for DCV5T, we performed additional experiment on a trilayer and extracted the positions of the resonance peak maximum (for S, AS and S+AS state) from a large set of $\mathrm{d}I/\mathrm{d}V$ spectra, measured on molecules adsorbed on a bilayer and trilayer of NaCl on both Cu(111) and Cu(311) (see Fig. 3.9a). For the doubly charged molecules (a, bottom most panel), the general trend observed is a shift in the relative position of maxima towards more positive voltages when the number of layers is increased. For the pentacene molecules [121], which are in the neutral state for a bias window applied, in contrast to DCV5T on NaCl/Cu(311), the spectra are almost the same for both negative and positive bias side, except for a slight offset.

As discussed in the chapter 1, DBTJs are very asymmetric transport

setups in terms of the tunneling rates between the molecule and the substrate and between the tip and the molecule. When the positive bias voltage is applied, the Fermi level of the tip and that of the copper are offset by eV. Part of this voltage drops across the NaCl, αV, and the rest of it across the vacuum gap between the molecule and the tip. Because of the voltage drops, the NaCl and vacuum barrier heights are dependent of bias applied. The magnitude of the resonant tunneling current depends on which barrier dominates the transport[1]. The NaCl thickness d increases from two- to three-layers (8.1Å), while z, the vacuum barrier, decreases since the set-point was kept unchanged for the spectroscopy measurement, we have different capacitance value as a result of this change, and hence, to the total energy. Under our experimental conditions, tunneling from the tip onto the molecule and the other way around acts as a bottleneck process.

The difference in the way in which peaks are evolving for the neutral and charged molecules when increasing the number of layers can be understood by considering the DBTJ with the vacuum and NaCl as barriers, and by modeling the system as a parallel-plate capacitor. For the tip-molecule and molecule-substrate capacitance we define $C_{\mathrm{T}} = \epsilon_0 A/z$ and $C_{\mathrm{S}} = \epsilon_0 \epsilon_r A/d$, where d is the thickness and $\epsilon = 5.9$ the relative permittivity of NaCl film. ϵ_0 is the vacuum permittivity and A is a surface of the single molecule, estimated to be $1.5\,\mathrm{nm}^2$. Interaction of the electrons is treated classically: to put one additional electron onto the molecule finite charging energy $E_{\mathrm{C}} = e^2/2C_{\mathrm{S}}$ is required, and for two electrons $E_{\mathrm{C}} = e^2(N - N_0)/2C_{\mathrm{S}} = 2e^2/C_{\mathrm{S}}$.

The most practical way to explain the results is by schematic representation (Figure 3.9b), where the total energies are shown in a similar fashion as in Figure 3.7. In addition, here we plot a curve that corresponds to a trilayer (in purple), being a parabola with a slightly different curvature as compared to a bilayer (orange). Both curves

[1] A considerable part of the bias voltage can also drop across the molecule due to the polarizability.

have parabolic shape because of the $E \propto e^2$ dependence. The chemical potential is affected when another substrate is used and additional term $\Delta\mu(N - N_0)$ has to enter the expression for the total energy, where μ is the substrate's chemical potential. Hence, we need to differ between (1) a neutral case, when the vertices of both parabolas coincide (b, top) and (2) doubly charged case, where the total energies are the same for N_0, but the ground state energies for N_2 are not equal and they do not overlap (b, bottom panel). For (1), the peaks at the negative and the positive biases should shift by the same value (in the opposite bias directions) when the number of layers is increased. This is indeed observed for the pentacene molecule, which we use as a reference here due to absence of resonances for the neutral DCV5T on the negative bias side (on a positive side there is agreement with experimental findings, Figure 3.9a, middle panel). In the latter case (2), a new chemical potential alters the position of both curves such that the ground state-to-ground state transitions are not any more symmetric for the trilayer around N_2 state, i.e. transition to lowest lying anionic state on the trilayer does not need as much energy as for the bilayer (red arrow). The situation is inverted for transition to tri-anionic state (green arrow). This can be rephrased in the following way: If a molecule is adsorbed on three layers of NaCl, instead of two, removing one of two additional electrons requires a lot less energy then charging it with additional one.

Even though STM was previously used to probe (indirectly) the charge state of single atoms and molecules, it is widely accepted that is not best suited for this task because of its working principle based on the tunneling of electrons, involving unintended (dis)charging of the investigated objects. Our method, however, take advantage of this fact, demonstrating that the charge state of neutral and negatively charged adsorbates can be determined by monitoring shift of the resonance peaks. There is no reason why it cannot be extended to distinguish between positive and neutral species, as long as those are enough stable to be investigated on the higher number of insulating layers.

3.10 Conclusion

In conclusion, we showed that a reduction of the single-particle level spacing of two frontier orbitals enables the manifestation of strong electron-correlation effects in single molecules. Here, the single-particle level spacing engineered by dicyanovinyl-substitution is leading to an apparent reversal of orbital sequence and a strongly-entangled ground state of $DCV5T^{2-}$. In this regime conduction exhibits a spatial signature fundamentally different from what a single particle picture would predict. Both the topographical and spectral signatures of this entangled state can only be captured within a many body picture for electronic transport.

4 Periodic charging of molecules coupled to the motion of an AFM tip

This chapter contains material published in the following publications:
N. Kocić, P. Weiderer, S. Keller, S. Decurtins, S.-X. Liu and J. Repp, 'Periodic charging of individual molecules coupled to the motion of an AFM tip.' *Nano Letters* 15 (2015), 4406
and
N. Kocić, S. Decurtins, S.-X. Liu and J. Repp, 'Forces from periodic charging of adsorbed molecules.' *Journal of Chemical Physics* (accepted).

In the previous chapter it was described how by the appropriate choice of the substrate's work function, single molecules can be deliberately and permanently switched in their charge state. In this chapter we will show how individual molecules at the edges of self-assembled islands grown on Ag(111) can temporarily change their charge state due to the presence of the electric field from a scanning-probe tip. Close to the threshold voltage for a charge state transition, periodic switching of the charge is directly driven by the cantilever motion in frequency-modulated AFM, as can be deduced from the signature in the measured frequency shift. The amplitude dependence indicates a smooth rather than a sudden charge state transition, while the absence of any appreciable signal in the dissipation channel points towards a non-hysteretic process. Temperature-dependent experiments show that the thermal broadening in the substrate is responsible for

the smooth charge transition. In this regime, the integrated frequency shift yields the tip-sample force that is due to a single additional electron. Further, the signature of the dynamic charging response provides information on the electronic coupling of the molecule to the substrate. In analogy to previous experiments on quantum dots, this may also be used in the future to access excited state properties of single molecules from AFM experiments.

4.1 Single-electron charging

Single-electron charging is critical for many areas of nanoscience, e.g. for quantum-dot research [138–140] and single-molecule electronics [141–143]. By means of scanning probe microscopy, control of the charge state in atoms [57, 144], molecules [72, 123, 145, 146], and quantum dots [147, 148] has been demonstrated. Charging and discharging events can be detected in the conductance measured in STM [149, 150], from the response signal to a scanned gate [151], as well as in the force [152–154], frequency shift [155–158] or dissipation signal [155, 159] in AFM. For AFM, the oscillatory motion of a frequency-modulated AFM tip can be directly coupled to the charging and discharging of localized electronic states in quantum dots, because it modulates the electric field in the junction, which in turn causes the charge state to oscillate. In the context of quantum dots, it has been proposed that this dynamic response to single electron charging process in AFM can be used to detect the properties of localized electronic states, including their excitation spectrum [160, 161]. Hence, analogous experiments on individual molecules may establish a novel spectroscopic tool to investigate their electronic properties.

4.2 Experimental details and sample preparation

For FM-AFM measurements the apex of the tip was functionalized with a CO molecule [82] except for the temperature dependent measurements. All AFM images were recorded by measuring the frequency shift while scanning in constant-height mode. The bias voltage V is applied to the sample. All spectra were acquired atop of the center of the molecules. While taking differential conductance ($\mathrm{d}I/\mathrm{d}V$) spectra the cantilever oscillation drive signal was switched off, while during FM-AFM data acquisition any bias modulation was switched off.

For the experiments at elevated temperatures the temperature dependence of the expansion coefficient of the piezo-electrical elements and the sensor's sensitivity has been calibrated from substrate defect step heights and from simultaneous STM/AFM measurements at various oscillation amplitudes. Upon increasing the temperature from 5.2 to 13.9 K the expansion coefficient of the piezo-electrical elements and the sensor's sensitivity change by slightly less than 15% and 10%, respectively. These temperature dependencies have been accounted for. For more details see section 2.8. The sensor is thermally coupled to the helium bath cryostat by a separate wire and may therefore be colder than the sample.

The molecule under investigation, 1,6,7,12-tetraazaperylene (TAPE)-[162] (for its structure see Figure 4.2) belongs to the bis(α, α'-diimine)-type of ligands. It is a planar D_{2h}-symmetric molecule and it is helpful to consider that its C-H groups qualify as weak hydrogen bond donors, so that many stabilizing C-H$\cdots$N contacts can be formed through an appropriate 2D assembly (Figure 4.2a).

TAPE molecules were thermally sublimed onto a Ag(111) surface held at low temperature with submonolayer coverage. Subsequent annealing to 280 K resulted in self-assembled islands with a periodic structure, in which each molecule is rotated by roughly $\Theta = 80°$ with respect to its four neighbors, as confirmed by atomically resolved AFM

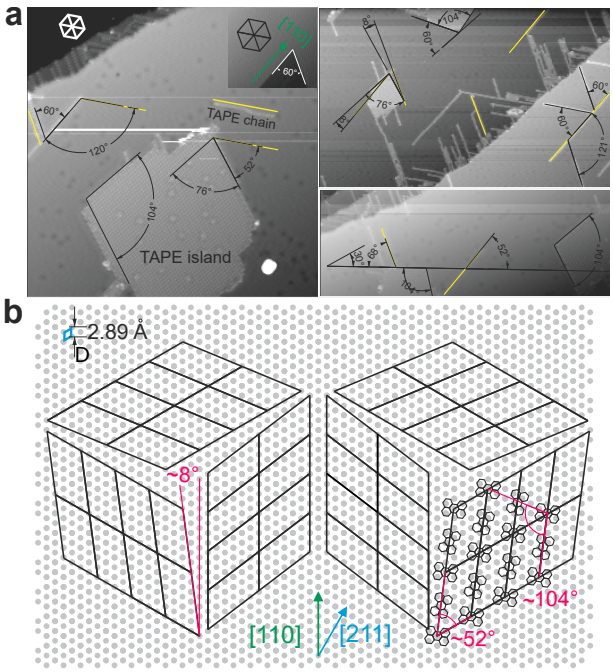

Figure 4.1: (a) Set of topographic images of Ag(111) after deposition of TAPE and annealing to 280 K. Directions of some chains are shown as yellow lines for a better visualization, with the measured angles indicated. Inset shows one of the Ag slip-step we used for the surface orientation determination. (b) Model of Ag(111) (atoms are represented as grey circles) and all possible orientations of TAPE islands on the surface. The measured angles in (a) can be rationalized based on the model. Large cells consisting of 8 unit cells are shown.

images (see Figure 4.8c). Due to clearly alternating molecular orientations within the layer, it can be described by oblique lattice with a cell containing two molecules. Upon annealing we also observed some linear chain-like molecular assemblies. These are composed of few up to hundreds of monomer units and most likely are connected by coordination bonds with Ag adatoms. Their properties will not be discussed in the framework of this thesis.

Evaluation of the azimuthal orientation of the molecular islands on Ag(111) surface relative to the chains, given in a set of the STM images in Figure 4.1a, reveals that the islands edges adopt angles of 52° (8°, 68°) with respect to the chains' directions, whereas the chains are rotated by multiples of 60°[1]. The angle between two adjacent molecular island edges is 104° or 76°. Apparently, the molecules take up only certain positions with regard to the substrate, because otherwise many different angles would be expected. This also means that unit cell vectors should fit to the substrate lattice. Note that, the existence of a definite adsorption site cannot be taken for granted: a large molecule which averages over few periods of the substrate corrugation potential is not in general expected to adsorb site-specifically. It is known that on weak-interacting metals e.g. on Au(111), many molecules form incommensurate overlayers, which then overgrow the reconstruction of the surface without being influenced by its complexity. On the other hand, on Ag(111) the molecule-substrate interaction is slighty stronger and may have as a result definite adsorption sites.

The orientation of both islands and chains in respect to the high-symmetry directions of substrate can be determined from atomically resolved STM images of the bare terraces. As atomic resolution of the closed-packed Ag(111) surface could not be obtained under conventional imaging conditions in STM, some areas with slip steps running along the closed packed <110> directions (green arrow in Figure 4.1a) allow us to propose orientation of the molecar island in respect to high-symmetry axes as shown in Figure 4.1b (other regions follow no specific surface direction, and therefore are wavy). Our experiments were complemented by DFT calculations by our collaborators from CFM/MPC, Spain, and Instituto de Física de Rosario, Argentina. Here, we will shortly describe their findings: The unit cell contains two molecules lying flat on the surface defined by the vectors **a** and **b** with lenghts 4 D and $\frac{\sqrt{172}}{2}$ D, respectively, with an angle between them of 52.4°. This is in a very good agreement with our measurements.

[1] Relatively small error bar of ±2° should be considered.

Inside the 2D assembly of the island, molecules experience an identical environment, so they can be viewed as being equal, each appearing as one protrusion (see Figure 4.2a). However, along the edges of the island, the molecules alternate between exposing four C-H groups and their α, α'-diimine side to the outside. The latter molecules, labeled here as type Q, have two lone-pairs of the nitrogen atoms unmasked along the periphery, and exhibit a distinctly larger apparent height in STM images than all other molecules, labeled as type A. Their different appearance is not related to distinct adsorption sites or in-plane orientations of the molecules relative to the high-symmetry directions of the substrate, but only due to their molecular neighborhood that decides upon which molecule takes the role of A and which of Q type.

4.3 Gating the charge state with electric field

For negative bias voltages below a certain threshold value V_{th}, type Q molecules appear similar to type A. We assign this sudden change in appearance to a charge state switching that is due to the electric field brought about by the voltage applied to the junction. This charge state switching is fully analogous to previous STM-based experiments by Fernández-Torrente and coworkers for TCNQ molecules on Au(111) [150], for which a transition between the neutral (at more positive sample voltage) and the anionic states (at more negative sample voltage) could be observed. Similar charging of local electronic states brought about by the gating effect of the tip has been observed in many cases [149, 163–165]. In all these cases the electric field in the junction shifts a localized state with respect to the chemical potential of the substrate. If without applied bias the localized state is close enough to the substrate's chemical potential, at a given threshold electric field $\mathcal{E}_{\mathrm{th}}$ the localized state can be shifted across the chemical potential of the substrate, which will change the (average) occupation of the state and hence the charge state. The shift of the localized state

in energy ΔE is proportional to the electric field $\mathcal{E}$ in the junction, which in turn is proportional to the applied bias voltage V, resulting in the proportionality $\Delta E = e\alpha V$ with the elementary charge e and a proportionality factor α, the so-called lever arm, which depends on the tip position.

In these studies, several key features in STM experiments of such charging processes have been identified as follows. (i) As the charging will affect the conductance of the STM junction, at the threshold voltage at which charging occurs a sharp peak or dip in differential conductance is observed. (ii) This peak or dip in differential conductance strongly depends on the tip-sample distance z, which affects the lever arm α. (iii) Only if the tip is close enough to a given localized state, will the gating be strong enough to lead to charging. Consequently, for images in a particular voltage range, the charging transition can be seen as characteristic ring-like features in images, the diameter of which strongly depends on the bias voltage. At the circumference of these rings, the transition from one to the other charge state occurs. All these fingerprints can be observed for the type Q molecules in the TAPE island edges. Figure 4.2b shows the sharp dip in differential conductance that strongly shifts with changing tip-sample distance (Figure 4.2c), whereas Figure 4.2d displays the characteristic ring-like features observed in images close to the threshold voltage.

After having identified a system that shows single-molecule charging resulting from gating with the scanning probe tip, in the remainder we will discuss the coupling of the charging effect to the oscillatory motion of our FM-AFM tip. Figure 4.3a shows frequency shift $\Delta f(V)$-spectra as a function of sample voltage V acquired with the tip positioned over the center of both type of molecules. The overall shape is parabolic, resulting from the electrostatic forces between tip and sample being proportional to $(V - V_{\mathrm{CPD}})^2$, which is well known from Kelvin Probe Force Spectroscopy [128, 155, 166]. V_{CPD} denotes the voltage of compensated contact potential difference. Type Q molecules show a distinct dip in $\Delta f(V)$ on top of the overall parabolic spectrum.

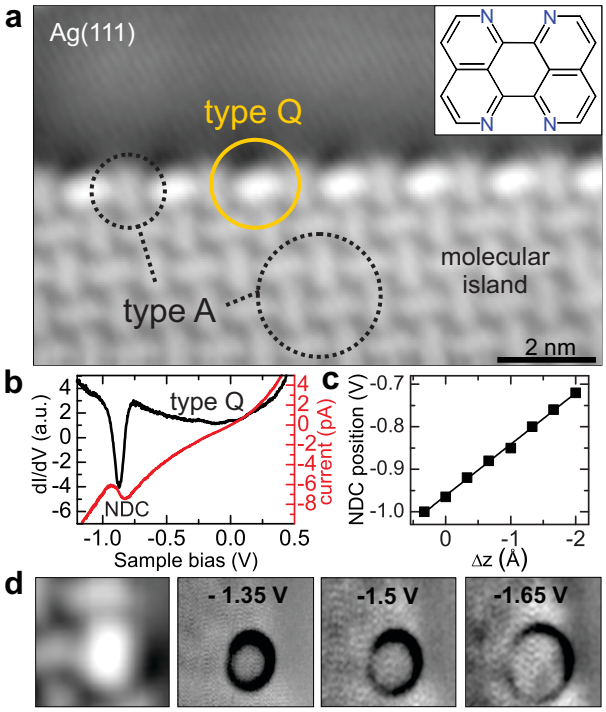

Figure 4.2: (a) STM image of the edge of a self-assembled island of 1,6,7,12-tetraazaperylene molecules (TAPE). Imaging parameters: $V = 0.1\,\mathrm{V}$, $I = 3.5\,\mathrm{pA}$. Inset: The molecular structure of TAPE. (b) $I(V)$ (red) and $\mathrm{d}I/\mathrm{d}V$ spectrum (black) acquired above the center of the Q molecule. (c) Observed positions of NDC in $\mathrm{d}I/\mathrm{d}V$ as a function of Δz. Positive Δz represents an increase in the tip-sample distance with respect to an STM set point, here $V = -1.4\,\mathrm{V}$, $I = 3.5\,\mathrm{pA}$ above the clean Ag(111). (d) Topographic image (left) and constant-height $\mathrm{d}I/\mathrm{d}V$-maps of the same area of an island edge for three different bias voltages, as indicated (tip retracted by 1 Å from set point: 7 pA, 0.16 V). The lock-in modulation is 8 mV rms at 230 Hz.

This feature, which is not present for type A molecules, occurs at the same voltage V_{th} where $\mathrm{d}I/\mathrm{d}V$-spectra show sharp negative differential conductance being associated with the change in charge state of the molecule. As the dip is associated to charging, the parts of the KPFS spectra left and right to the dip correspond to different charge states, for which the Kelvin parabolas are slightly shifted against each other [128]. If instead the voltage is fixed and the tip is approaching the sample, $\Delta f(z)$ becomes more negative with decreasing distance because of the attractive tip-sample interaction. Also for this type of spectra, type A and type Q molecules show the same overall behavior, except for a dip in $\Delta f(z)$ that is only seen for type Q molecules at a distance z at which the charging occurs, as is shown in Figure 4.3b. Hence, at the parameters corresponding to the threshold electric field $\mathcal{E}_{\mathrm{th}}$ for charging a pronounced dip in $\Delta f(z)$ is observed, which can be understood as follows. Even a small oscillation of the tip appreciably modulates the electric field and the gating of molecular levels in the junction. Therefore, by bringing a molecular level in alignment with the electrochemical potential of the sample, the periodic gating leads to an oscillation of the charge on the molecule being synchronized with the mechanical tip oscillation.

In FM-AFM the frequency shift Δf is proportional to the vertical derivative of the vertical component of the force as $\Delta f \propto \partial F_z/\partial z$ in the limit of small oscillation amplitudes. Hence, the almost identical Δf-spectra for type A and Q molecules for the parameter range, in which no charge state switching occurs, indicates that the tip-sample forces as a function of distance and voltage have to be very similar for the two cases, as their derivatives are almost the same. However, the forces for type A and Q molecules may well be offset by an (almost) constant value, which would not be affecting the Δf-signal. However, at the charge state transition, the effective force acting on the cantilever will make a transition from the one for neutral molecules to the one for charged ones [2] as is depicted in Figure 4.3c. Hence, at this

[2] We cannot exclude the possibility that the charging occurs between the anionic

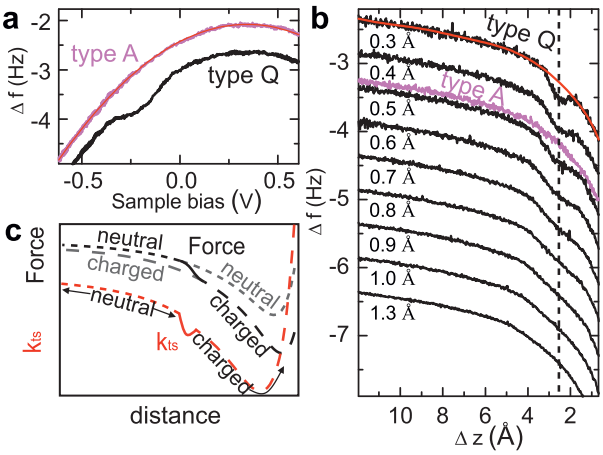

Figure 4.3: Frequency shift Δf measured as a function of V (a) and Δz (b) above type Q and type A molecules, respectively. The charging of the molecule is observed as a dip in both type of spectra. The spectra are offset by -0.6 Hz in (a) and -0.5 Hz in (b) for clarity. In (b) the tip oscillation amplitude is increased from 0.3 Å to 1.3 Å at $V = -0.6\,V$ and $\Delta z = 0$ refers to the vertical position above the Ag(111) surface with the tunneling set point of $V = 0.1$ V, $I = 1.2$ pA. (c) Sketch of force-distance curves for the molecule Q being in its neutral (dotted) and charged (dashed) state. If charging occurs at a certain tip height, the effective tip-sample force (black) will change from one to the other curve, resulting in a dip in $k_{\mathrm{ts}} = -\partial F_z/\partial z$.

transition, a constant offset between the forces for neutral and charged molecules will lead to a distinct peak or dip in the derivative of the force, and consequently to a pronounced feature in the frequency shift Δf spectra. We subtracted the overall dependence by fitting $\Delta f(z)$ spectra in the parameter region outside of the feature to a polynomial of eighth order, resulting in the feature associated to the charging, as is shown in Figure 4.5a. Such Δf spectra after subtracting the overall dependence, showing only the feature associated to charging, will be henceforth referred to as Δf_{dip}. To analyze this feature quantitatively

and dianionic state of the molecules.

one has to go beyond the limit of small amplitudes, as the charging may occur at a very narrow distance interval. To derive the frequency shift for finite amplitudes A, the tip-sample stiffness $k_{\mathrm{ts}} = -\partial F_z/\partial z$ has to be averaged over the oscillatory motion around the equilibrium position z_c of the tip with a semicircular weight function [167] such that:

$$\Delta f(z_c) = -\frac{f_0}{2k}\frac{2}{\pi A^2}\int_{-A}^{A} \left.\frac{\partial F_z}{\partial z}\right|_{z_c+\zeta} \sqrt{A^2-\zeta^2}\, d\zeta. \tag{4.1}$$

This relation can be used to extract the tip-sample stiffness $k_{\mathrm{ts}}(z)$ by deconvolution from $\Delta f(z)$-spectra. As deconvolution increases the apparent noise in the data, we instead discuss the expected shape of $k_{\mathrm{ts}}(z)$, convolve it according to Eq. 4.1 and compare the result to the spectra.

But before doing so, we will describe the basics of adsorption in the next section, as this will be of high relevance for the futher analysis of our spectra.

4.4 Newns-Anderson model of adsorption

In the 1930s people were trying to find a model to adequately describe the electronic structure of the surface. The simplest model proposed at that time is called jellium model of the metal surfaces. Gurney proposed a formalism to calculate some properties of adsorbates on the surface using some of the advantages of this approach, however, without any quantitative calculations [168]. He was able, though, to show that when the adsorbate interacts with the surface, the energy levels of the adsorbate are broadened and shifted due to the interaction with the substrate states. In 1969, Newns demonstrated that Gurney's model is a consequence of the formalism given by Anderson in 1961. Usually, one refer to this work as the Newns-Anderson model of adsorption [169, 170], or more fully as the Anderson-Grimley-Newns model [171, 172].

When the adsorbate and the surface are far apart, their electronic structures can be considered not to be disturbed by the presence of each other. If the adsorbate approaches the substrate, the wave functions overlap substantially and the whole system should be considered as a mixture of both. The overlap of the wavefunction of an adsorbate $|a\rangle$ with an energy ϵ_a, and metal surface one-electron Bloch states $|k\rangle$ with energies ϵ_k, is described by overlap matrix elements $V_{a,k} = \langle a|\,\mathbf{H}\,|k\rangle$, where $\mathbf{H}$ is the Hamiltonian of the whole adsorption system. Other matrix elements are $H_{aa} = \epsilon_a$ and $H_{kk} = \epsilon_k$ i.e. unperturbed levels for the free adsorbate and surface. The energy levels of the combined system can be calculated by the diagonalization of this Hamiltonian matrix. The projected density of states is the most easiest way to show the results of this diagonalization (Figure 4.4c). The derivation is demanding and is not meant to be part of this work. For a detail explanation see Ref. [173, 174]. The result is that the density of states for adsorption is given with the formula $n_a(\epsilon) = \Gamma/[([E - \epsilon_a]^2 + \Gamma^2)\pi]$, where Γ denotes the electronic coupling to the substrate and ϵ_a is the state's energy. Figure 4.4c shows schematically how the LDOS broadens from a delta function into a Lorentzian with a width Γ. In addition, the level shifts, and can change its occupancy.

To explain the broadening of the peaks, Holloway and Nørskov considered a level of the adsorbate far away from the surface and how it behaves as the adsorbate approaches the surface. The probability for the electrons to jump to the surface, and for the electron to jump from the surface to adsorbate is increasing by decreasing the adsorbate-substrate distance (Figure 4.4c). The resonance that has a finite lifetime Δt also has a finite width ΔE, related by the uncertainty principle $(\Delta E)(\Delta t) = 2\pi\hbar$. In other words, if the electron has a finite lifetime on the adsorbate, the level will be broadened by ΔE. If the electron is rapidly exchanging with the substrate, the lifetime will be very short and this will lead to a broad resonance.

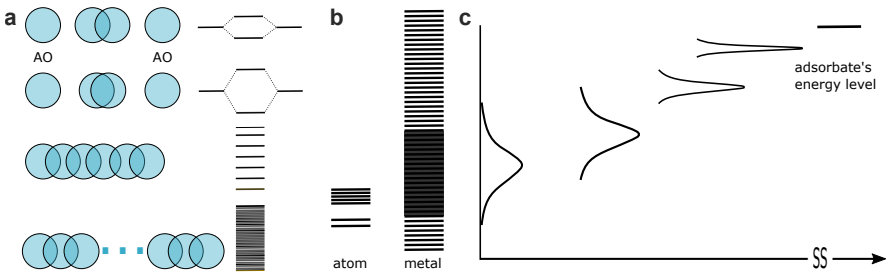

Figure 4.4: (a, top to bottom) Formation of a band as a result of adding single atoms to the chain of atoms: a one-dimensional metal case. If an atom is added to a single atom that has orbital of a certain energy, one bonding and one antibonding molecular orbitals are formed (splitting is dependent on the overlap). The number of molecular orbitals are always equal to the number of the atomic orbitals. As this number increases, the energy difference between the individual molecular orbitals decreases. When a very large number of atoms is added, the distance between the neighbouring energy levels approaches zero. (b) The electronic structure of the metal described by a series of continuous bands, where individual molecular orbitals cannot be resolved any more, and comparison with the discrete levels of a single atom. (c) As the adsorbate approaches the surface the shape of the state broadens to a Lorentzian with a width Γ, also sometimes called the *chemisorption function*. The relative position of the resonance and the surfaces Fermi level determines the nature of the surface bond. For example, if a previously unoccupied level lies below the Fermi level, metal will donate the charge to the adsorbate, if the resonance hits the Fermi level only in part, the electrons will be shared and a covalent bonds form. This model is not accounting for detailed electronic structure of the adsorbate.

4.5 The smooth charge transition

If the charge state transition was sudden, it would give rise to an infinitely sharp feature in $k_{\mathrm{ts}}(z)$ resulting in a dip in $\Delta f(z)$-spectra with a total width equal to the distance interval $2A$ that the tip oscillates over. As the measured dip in $\Delta f(z)$-spectra is always wider than that (Figure 4.5a), the charge state transition cannot be sudden. Fluctuations of the oscillation amplitude are way too small to account for

the blurring of the dip in $\Delta f(z)$-spectra. In the following we consider how this charge state transition occurs in detail and which shape of $k_{\mathrm{ts}}(z)$ to expect.

As pointed out above, from the signatures in the STM channel, the charging is ascribed to shifting a localized electronic state in the molecule across the Fermi level of the substrate. As the molecules are adsorbed directly on the metal substrate their electronic states will hybridize with those of the substrate, leading to a broadening in energy E with a Lorentzian profile, described in the previous paragraph: $\Gamma/[([E-\epsilon]^2+\Gamma^2)\pi]$, where $\epsilon(z,V)$ is the state's energy. The latter will be shifted in energy by the electric field in the junction as discussed above and therefore depends on the tip-sample distance z and bias voltage V. In addition to the finite width of the localized state that undergoes the charge transition, the smearing in the Fermi distribution function $f(E)$ at $T = 6\,\mathrm{K}$, the temperature of our experiment, contributes to the smoothing of the charge state transition as the state is shifted across the Fermi level. Based on this simple picture, which is illustrated in Figure 4.6, the occupation n of this broadened state is expected to change according to

$$n(\epsilon) = \int_{-\infty}^{\infty} f(E) \frac{\Gamma}{([E-\epsilon(z,V)]^2+\Gamma^2)\pi}\,\mathrm{d}E. \tag{4.2}$$

Assuming that the extra force F_q resulting from the additional charge $q = en$ is proportional to the latter and hence also to the occupation n, the additional tip-sample stiffness $\Delta k_q(z)$ will be proportional to $\partial F_q/\partial z \propto \partial n/\partial z = (\partial n/\partial\epsilon)(\partial\epsilon(z,V)/\partial z)$. Note that the z-dependence of n stems only from the z-dependence of the energy of the state $\epsilon(z,V)$. Using Eq. 4.2 this yields

$$\Delta k_{\mathrm{ts}}(\epsilon) \propto \frac{\partial n}{\partial \epsilon}\frac{\partial \epsilon}{\partial z} = \frac{\partial \epsilon}{\partial z}\int_{-\infty}^{\infty} \frac{\mathrm{d}f}{\mathrm{d}E}\bigg|_{E'+\epsilon} \frac{\Gamma}{(E'^2+\Gamma^2)\pi}\,\mathrm{d}E', \tag{4.3}$$

a convolution of the derivative of the Fermi distribution $\mathrm{d}f(E)/\mathrm{d}E$ and a Lorentzian peak. This is in line with the two smoothing mech-

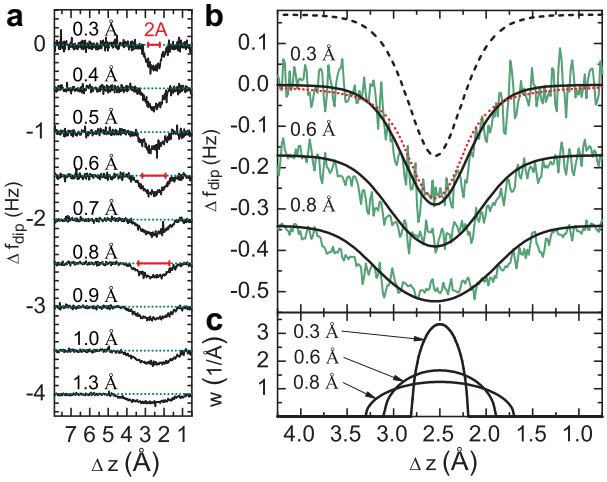

Figure 4.5: (a) $\Delta f(z)$ response of the charging process obtained by subtracting the fit to the overall shape from the measured spectra shown in Figure 4.3b. In (b) the dip of the frequency shift signal is shown for three different oscillation amplitudes A, each fit (solid line) by a convolution of the derivative of the Fermi function (dashed line) with a semicircular weight function $w(A)$ shown in (c). In comparison, a Lorentzian convoluted with $w(A)$ accordingly (dotted line), does not fit the data as accurately. In (a) and (b) spectra are vertically offset for clarity.

anisms identified above. If one of the two dominates the other, it will determine the shape of the dip in $k_{\mathrm{ts}}(z)$. We assume that the shift of the state's energy $\epsilon(z)$ with z can be linearized around z_c, because the oscillation amplitude A is always small compared to the tip-sample distance. As is shown in Figure 4.5b the derivative of the Fermi distribution $\mathrm{d}f/\mathrm{d}E$ convolved with the respective weight function according to Eq. 4.1 very well reproduces the experimentally observed dip in $\Delta f(z)$ spectra for different oscillation amplitudes. A similar procedure with a Lorentzian shows also good overall agreement, but not as good as for the derivative of the Fermi distribution. This suggests that the temperature-broadened Fermi distribution is

mainly responsible for the smooth charge transition.

4.6 Temperature-dependent experiment

To test this hypothesis, we extracted $\Delta f_{\mathrm{dip}}(V)$ by subtracting the overall parabolic behavior from $\Delta f(V)$-spectra measured at a set of slightly elevated temperatures between 5.2 and 13.9 K. Two of these $\Delta f_{\mathrm{dip}}(V)$-curves are shown in Figure 4.6b for the temperatures of 5.2 K and 9.5 K, respectively. The increase in width at elevated temperatures is directly apparent from the graphs, confirming our hypothesis of the thermal broadening being dominant [62]. To analyze this quantitatively, we fitted many analogous $\Delta f_{\mathrm{dip}}(V)$-curves for a set of three different amplitudes and five different temperatures to Gaussian functions. The resulting width (FWHM full width at half maximum) of the fit function is displayed in Figure 4.6c. A comparison to the expected width from the simple model outlined above yields very good agreement (dashed lines).

For these simulations it was assumed that the temperature-broadened Fermi distribution is mainly responsible for the smooth charge transition whereas the life-time broadening is negligible. Hence, in the limit of zero oscillation amplitudes the dip in $\Delta f(V)$ is given by the derivative of the Fermi function. The energetic shift between molecular level and the sample's Fermi level is scaled with the lever arm α and, consequently, the resulting dip in $\Delta f(V)$ at zero amplitudes has a FWHM of $\simeq 3.5 k_B T/\alpha$. A level arm of $\alpha = 1/62$ yields very good agreement. To account for finite oscillation amplitudes we convoluted this function with the corresponding weight function (see Eq. 4.1). To this end, we assumed the electric field in the junction and hence the lever arm α to scale inversely with the absolute tip-sample distance z, which we assumed to be $z_0 = 6$ Å. For the small oscillation amplitudes used in our experiments we linearized the $1/z$ dependence around z_0.

For example, a peak-to-peak tip oscillation of 1 Å at an average distance of $z_0 = 6$ Å is assumed to modulate the field in the junction by $1/6 \simeq 16\,\%$. Under these assumptions, the weight function can be expressed as a function of bias voltage, which we then convoluted with the above mentioned function of the temperature-broadened dip. The resulting curve was numerically fitted to a Gaussian. The lever arm α equals the ratio of the capacitive coupling of the molecule to the tip over the capacitive coupling of the molecule to the entire environment (to the sample, ground, and the tip) [157, 160, 175].

Both above values are reasonable for the given geometry [62]. The above findings provide a surprisingly small upper bound for the lifetime broadening Γ of $\Gamma < 3.5 k_B T_{5.2\,\mathrm{K}} \simeq 1.5$ meV. It further implies that the observed smooth charge transition has to be interpreted as a statistical tunneling process of substrate electrons on and off the adsorbate.

Note that, the simple picture described above does not include possible back-action of the charge in the molecule to the energetic level alignment. Such effects may arise e. g. from polarization and would be reflected in the shape and width of the dip in Δf. Hence, the analysis of dynamic charge response in FM-AFM-based spectroscopy as presented here in conjunction with a sophisticated theoretical description of molecular charging may shed new light on polarization effects in molecules in the future.

The above-discussed picture of the dip in $\Delta f(z)$ being associated with a charging process at a certain threshold electric field $\mathcal{E}_{\mathrm{th}}$ is further corroborated by varying the applied voltage and observing how the dip in $\Delta f(z)$-spectra shifts along z for increasing V, as is shown in Figure 4.8a. The dip in $\Delta f(V)$-spectra has the same origin and similarly widens with increasing oscillation amplitude as shown in Figure 4.8b without subtracting the parabolic background.

The additional force resulting from the one additional elementary charge can be calculated simply from integrating the dip in $k_{\mathrm{ts}}(z)$

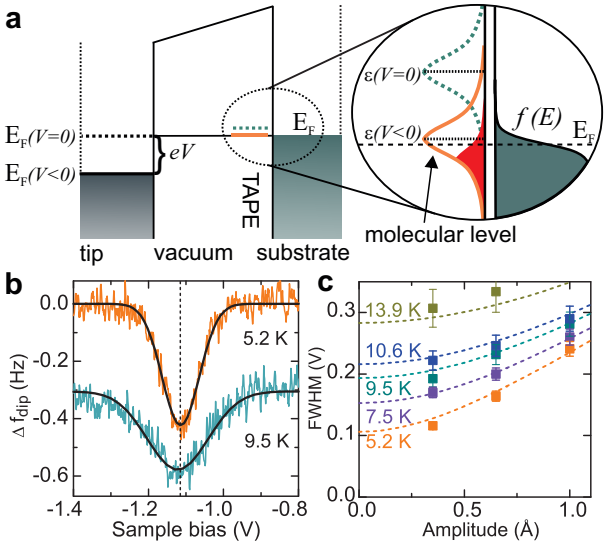

Figure 4.6: (a) Schematic illustration of the charging process upon shifting the Lorentzian-shaped electronic level across Fermi level of the substrate with an occupation according to the Fermi distribution function. The shaded areas illustrate the occupation of states. (b) Measured frequency shift response to charging Δf_{dip} for a fixed oscillation amplitude of 0.35 Å and two different temperatures of 5.2 K and 9.5 K, respectively. The curves are fitted to Gaussians. (c) Evolution of the full width at half maximum extracted from fitting procedures analogous to (b) as a function of oscillation amplitudes for five different temperatures.

over z [23]. This integration results in a force of $\Delta F = 3\,\mathrm{pN}$, which is comparable to values reported in the literature [155]. This value should not depend on the oscillation amplitude, which we confirmed within the uncertainty of the experiment. According to the mechanism behind the charging established in the literature [150], the charge state changes from neutral to negatively charged, when approaching the cantilever to the sample at an appropriate bias voltage. This is in line with the larger apparent height in STM images for the neu-

tral molecule. Hence, the dip in $k_{\mathrm{ts}}(z)$ indicates a more attractive interaction for the charged species as compared to the neutral one. Such an additional attraction is expected from both van-der-Waals and electrostatic interactions. The charging may also lead to a vertical relaxation of the entire molecule, which will also affect the force measured at a given height above the molecule.

4.7 The absence of dissipation

As described earlier, to keep the oscillation amplitude constant, the sensor must be continually driven. The driving signal, adjusted by an amplitude feedback controller, is a measure of the dissipation. When the sensor is far away from the sample, the dissipation is governed by damping in the sensor and its holder (intrinsic energy losses). In the experiments performed close to the sample, an increase of this signal allows for a direct measurement of damping processes in the junction. Hysteresis in the force as a function of distance leads to a signal in the dissipation channel [176, 177]. In the case of charging processes, such a hysteresis can result from structural relaxations in the junction [123, 144] or from a delay in the charging due to very low tunneling rates being on the time scale of the cantilever oscillation frequency f_0 [160, 175, 178]. The tunneling rates between molecule and substrate in our experiment are indeed expected to be much larger than f_0. Here, we can make estimation of this value: Currents in the process are in the order of 10^{-12} A, and hence, the time between two subsequent electrons to tunnel from the tip onto the molecule or into the substrate is approx. $e/I = 10^{-9}$ s. Tunneling processes between molecule and substrate are expected to be many orders of magnitude faster and can be considered to be instantaneous, at least, in timescale of the tip motion. The absence of hysteresis is in agreement with the observation that the charging is a smooth rather than a sudden transition as concluded from the above analysis of the Δf signal. In

the present case, the dissipation signal is below the experimental noise floor of 0.2 meV/cycle.

4.8 Charging rings in AFM

As mentioned in section 4.3, for images at appropriate voltages, the charging transition can be seen as characteristic ring-like features in $\mathrm{d}I/\mathrm{d}V$ images. Also Δf images acquired under such conditions exhibit rings associated to charging (see Figure 4.7) and as has been previously observed for quantum dots [156, 179]. In a certain bias voltage range, these rings can be observed directly above the molecule which is changing its charge state. If the charging of the molecules would be associated with a change in their lateral adsorption position, we would expect these ring-like features to show additional signatures resulting from a sudden change in topography. As this is not observed, we conclude that the charging does not affect the binding site.

4.9 Difference image

The spatial dependence of the additional attractive force can be seen in constant height Δf images acquired at an edge of a self-assembled island at zero bias voltage, as displayed in Figure 4.8c. At this voltage, A- and Q-type molecules are in different charge states. Not only do they appear differently in STM images, but also is their difference clearly visible in AFM images. The contrast of the type A and Q molecules is almost identical, except that the neutral type Q molecules appear brighter (less attractive) than the negatively charged type A molecules. This difference in Δf signal is apparent over the entire molecule and shows no pronounced submolecular features, suggesting that the one additional charge is delocalized over the entire molecule.

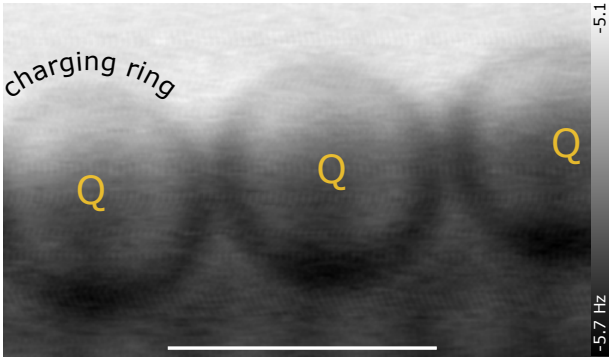

Figure 4.7: The frequency shift signal recorded at constant-height ($A = 0.95\,\text{Å}$, $V = -1\,\text{V}$, $\Delta z = 1.3\,\text{Å}$, where $\Delta z = 0$ refers to the vertical position above the center of the molecule in the interior of the island with the STM set-point parameters: $I = 9\,\text{pA}$, $V = -1\,\text{V}$). Ring-like contours, observed only above Q molecules, are due to charging of these. For lower (more negative) sample bias voltages their diameter increases. Scale bar 2 nm.

Figure 4.9a shows the same scan from Figure 4.8a but this time without the structure superimposed (the image is also rotated for better layout in the page). In a previous STM work, different types of adsorbed phthalocyanine molecules were shown to exhibit charge bistability [123]. In that case, the charge states were both stable within a certain range of applied bias voltages around zero, allowing to image the very same molecule in both charge states and to extract contrast changes. In the present case, this is not possible, since the charge state switching shows no hysteretic behavior, and hence, for a given molecule at a give voltage there is only one charge state observed. However, the highly regular arrangement in the self-assembled monolayer island still enables the extraction of a difference image as follows. Other than that, all molecules are placed in a highly regular way, thanks to self-assembly. This allows to generate two cutouts of the larger image, each showing four molecules, but only one of them containing a Q-type molecule, see Figures 4.9b,c. These can be over-

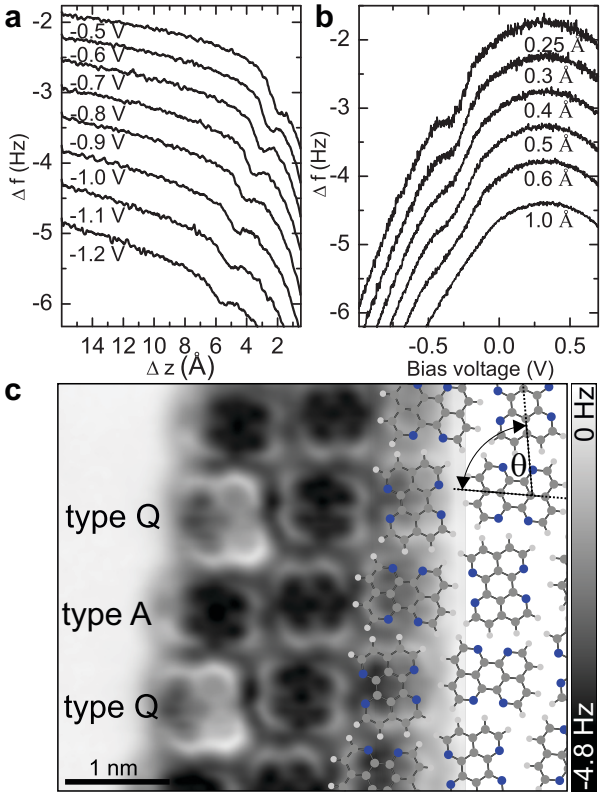

Figure 4.8: (a) $\Delta f(z)$ curves at different sample bias voltages (oscillation amplitude: 0.3 Å). The position of the charging feature shifts to larger Δz for more negative sample bias voltages. (The spectra were smoothed using Fourier-filtering.) Due to the higher attractive forces the curves are shifted to more negative Δf values. $\Delta z = 0$ refers to the vertical position above the Ag(111) surface with the tunneling set point parameters: $I = 1.2\,\text{pA}$, $V = 0.1\,\text{V}$. (b) $\Delta f(V)$ curves for different tip oscillation amplitudes A. Here, for increasing A the dip in $\Delta f(V)$ becomes washed out. The spectra are offset by -0.5 Hz for clarity. Set point parameters: $I = 1.2\,\text{pA}$, $V = 0.1\,\text{V}$. (c) Constant-height AFM image of an island edge with the molecular structure partially overlaid. Each molecule is rotated by roughly $\Theta = 80°$ with respect to its four neighbors. Imaging parameters: $A = 0.5\,\text{Å}$, $V = 0\,\text{V}$, $\Delta z = -1.75\,\text{Å}$.

laid, with the identical three molecules acting as alignment markers, and then subtracted from each other. The resulting difference image is displayed in Figure 4.9d. It shows a relatively homogeneous contrast over the molecule that differs in its charge state (top right in Figure 4.9d) and no pronounced intra-molecular features.

In AFM, several different forces may contribute to the signal. In the current context, electrostatic, van-der-Waals, and Pauli repulsion forces will be the relevant ones. Whereas the former two are quite long-range in nature and will therefore contribute also at larger distances, the fact that we do observe intra-molecular contrast in Fig. 4.9a indicates that Pauli repulsion is relevant at the given tip-sample distances. Upon charging, it can be expected that all three of the above-mentioned forces will change as a result of the extra electron interacting with the AFM tip. We expect that the *relative* change to the electrostatic force will be quite large as the net charge of the molecule changes dramatically. In contrast, the *relative* change to the other two force components is expected to be rather weak, as for the latter all electrons of the molecule will contribute and the change associated to a single extra electron will hence be minor.

But not only can the extra electron directly affect the tip-molecule interaction, it may also result in slight relaxations within the molecule and of the molecule with respect to the substrate. For example, a charged molecule may interact more strongly with the substrate, such that a reduced adsorption height can be expected. Such relaxations would also contribute to the AFM signal indirectly. In this case, we would expect mostly the Pauli repulsion to be affected, as this is particularly short ranged, and hence, small geometric changes will have a large impact on Pauli repulsion. At first glance, one might assume that an overall vertical shift of the entire molecule would give rise to a homogeneous contrast change over the entire molecule. However, even a small vertical displacement of the entire molecule would greatly intensify the intermolecular contrast instead of adding to the homogeneous background. If that would be the case, we would expect a different im-

age that shows features of the molecular geometric structure, since it was shown that the latter is provided by the Pauli repulsion [82, 180]. As the contrast in Figure 4.9d is relatively homogeneous we conclude that such contribution is apparently small. A weak sub-molecular contrast can be observed also over type-A molecules, probably resulting from the non-perfect overlaps of the subtracted frames at different lateral positions. Different bending of the CO molecule at the functionalized tip may also contribute to the remaining sub-molecular contrast differences.

We tentatively assign the contrast change shown in Figure 4.9d as being dominated by the electrostatic interaction between the extra electron and the tip. Interestingly, this contrast, while being homogeneous over the entire molecule under consideration drops quite abruptly where the molecule ends. This seems to indicate that the extra electron is delocalized over the entire molecule, giving rise to an AFM signal over the molecule but not next to it. Finally, the contrast change shows a linear gradient from inside to outside the molecular island. This may be due to a contribution that is not completely uniform and may be explained by the two α, α'-diimine groups facing a different environment — one is adjacent to the hydrogens of a neighboring molecule, the other is exposed to the bare silver terrace.

4.10 Threshold voltage for charging

As already discussed, the threshold voltage for charging V_{th} depends on the tip-sample distance. To this point, a single charging event only at negative bias voltage was mentioned, but for a certain parameter range, one can observe also a similar charging phenomenon at positive bias voltages. Figure 4.10a (right panel) shows a typical $\Delta f(V)$ spectrum, recorded at a fixed tip-sample distance z. Whereas the overall parabolic shape of the curve is governed by electrostatics [128, 155,

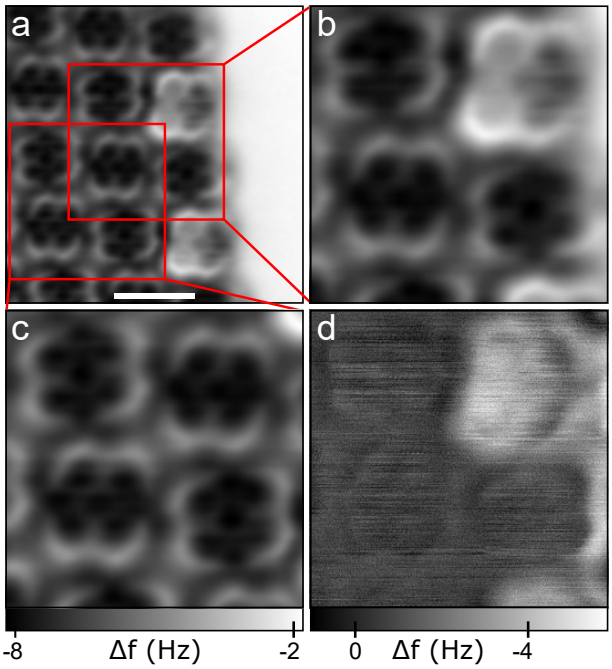

Figure 4.9: (a) Constant-height AFM image of a molecular island edge. Imaging parameters: $A = 0.5$ Å, $V = 0$ V, $\Delta z = -1.75$ Å. $\Delta z = 0$ refers to the vertical position above the Ag(111) surface with the tunneling set point parameters of $I = 1.2$ pA, $V = 0.1$ V. Scale bar 1 nm. (b,c) Zoom-ins of different areas from image in (a) as indicated. (d) The difference image obtained by subtracting image (b) from image (c) allows the effects of one additional charge to be visualized. The relative position of the two subtracted images was adjusted such that contributions above A-type molecules were close to zero. The images in (a), (b) and (c) have the same grayscale.

166], two dips, one each at positive and negative bias, indicate a charging event. Similar $\Delta f(V)$ spectra were recorded at a set of different distances z and the dip positions were extracted as a function of tip displacement Δz. In Figure 4.10a the bias voltages, at which charging was observed, is plotted against Δz for two different tip apices in

blue and green, respectively. Each data set for one particular charging event and one of the tips can be well fitted by a line. Each two lines corresponding to different charging processes but the same tip apex cross at $\Delta z \approx -11\,\text{Å}$ and small positive bias voltage.

The model for charging as discussed thus far suggests, that the electric field in the junction shifts an electronic level of the molecule across the Fermi level, such that its occupation changes [150, 158, 163, 181–184]. In light of this, it is not obvious, why two charging events can be observed. Maybe the two charging events correspond to the very same molecular orbital, but two different charging possibilities, separated by the Coulomb charging energy U. Hence, in this scenario an electron would be either added or removed from the same orbital at negative and positive bias voltage, respectively. The Coulomb charging energy U for a molecule directly adsorbed on a metal surface is greatly reduced due to screening and therefore may well be of the required magnitude [185, 186]. However, this would require the Q-type molecules to be already singly charged at zero bias and to become doubly charged at large negative bias voltages. We refrain from making such an assignment. We just note that two or more charging levels have been observed before for quantum dots as well as for molecules.

Irrespective of the nature of the two levels that are being shifted across the Fermi level, we can investigate whether the observed distance dependence fits to a simple model according to the picture behind the charging. As the fraction of the total bias voltage that drops between molecule and substrate is relatively small, such a level has to be close to the Fermi level also without any field in the junction. As one observes two charging events for opposite polarity, we have to assume two levels being close to the Fermi level at energies ϵ_1 and ϵ_2. In a simple plate capacitor model the fraction of the total bias voltage that drops between molecule and substrate, is simply given by the ratio of molecule-substrate distance d_{ms} divided by the total tip-substrate distance d_{ts}. Although at the atomic scale for adsorption of a molecule directly on the metal substrate the molecule-substrate distance d_{ms}

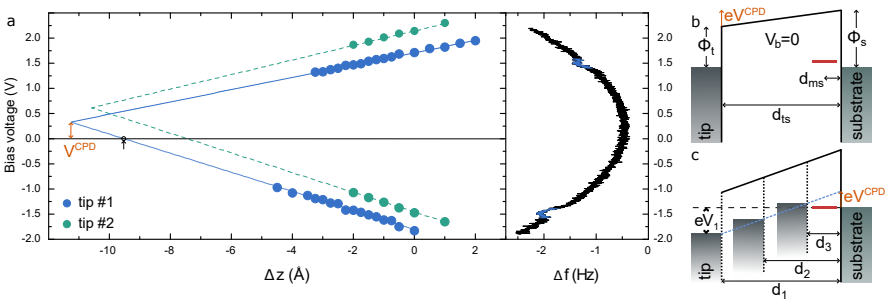

Figure 4.10: Extracted threshold voltages V_{th} for charging (left) as a function of tip height Δz at positive and negative bias voltages. The values were extracted from the observed dips in frequency shift spectra recorded for different Δz above the center of the Q molecule (example to the right for $\Delta z = -1.75$ Å). $\Delta z = 0$ corresponds to a STM set-point parameters above the Ag surface of $V = 0.6$ V, $I = 1.4$ pA for tip 1 and $V = 0.6$ V, $I = 1.9$ pA for tip 2, respectively. (b) Illustration of the potential drop in the junction without bias voltage applied, resulting from a finite contact potential difference (CPD), which results from a difference in work function of the tip Φ_{t} and sample Φ_{s}. (c) Illustration of the linear relationship of threshold voltage and distance as a result of the constant electric field required for charging the molecule. For different tip-sample distances, here exemplifed as $d_{1,2,3}$, the quantity $(V - V_{\mathrm{CPD}})$ has to be proportional to the distance (see dashed blue line) to keep a constant field that is required for charging the molecule.

is not a very well defined quantity, one may view this as an *effective* molecule-substrate distance d_{ms} that accounts for the possibility of an electric field to shift the molecular levels. One has to keep in mind, that for a non-zero contact potential difference between tip and sample, even at zero bias voltage there is a finite electric field across the junction (see Fig. 4.10b). Only at compensated CPD, that is at $V = V_{\mathrm{CPD}}$ the electric field vanishes. Although this is very well known from Kelvin probe force spectroscopy [29], it is usually less obvious in pure STM experiments. Hence, the shift of the molecular levels equals $\Delta E = e(V - V_{\mathrm{CPD}})d_{\mathrm{ms}}/d_{\mathrm{ts}}$, where e denotes the elementary charge. In the case of a charging event, this energy shift equals to

$-\epsilon_{1,2}$ such that the levels are aligned with the Fermi level of the substrate. Solving the above equation with respect to the bias voltage V, we obtain

$$V_{\mathrm{th}} = V_{\mathrm{CPD}} - \epsilon_{1,2} d_{\mathrm{ts}}/e d_{\mathrm{ms}}$$

Interestingly, this provides indeed a linear dependence of the threshold voltage with the tip-substrate distance d_{ts}, which in a more depictive description can be understood as follows. The charging condition is associated to a certain electric field in the junction. In the simple plate capacitor model, the potential drop has to increase linearly with distance to keep the electric field and thereby ΔE constant, giving rise to the linear scaling of V_{th} with tip-sample spacing d_{ts} (see Fig. 4.10c). This fits very well to the observed behavior. Moreover, the above equation suggests an interesting implication for the crossing point of the line fits in Fig. 4.10: irrespective of the particular values of $\epsilon_{1,2}$ all lines will cross at $d_{\mathrm{ts}} = 0$, where $V = V_{\mathrm{CPD}}$. Hence, the determination of the crossing points from observations as displayed in Fig. 4.10 should yield two valuable informations, namely, the LCPD and the absolute tip-to-substrate distance by providing $d_{\mathrm{ts}} = 0$ at the crossing point of the line fits. Note that the latter quantity is usually unknown in scanning probe experiments, such that having another way to estimate this quantity may be useful. The data in Fig. 4.10 suggest that the tip-to-substrate distance d_{ts} is ≈ 11 Å for the set-point parameters of 1.4 pA and 1.9 pA at 0.6 V, respectively. The local contact potential difference for the two tip apices has positive values of ≈ 0.3 and ≈ 0.7 eV, respectively. This is in the range of typical values measured also with KPFS.

As the crossing point of the two line fits is quite far from the range, in which data points are available, the question of the confidence range of the fits arises. To this end, we extracted the error margin for each of the two line fits exemplary for the dataset, for which more data points were available. From this, we calculated the error margins of the crossing point, corresponding to a standard deviation of 0.06 eV of the extract LCD value and 0.3 Å for the tip-sample separation. We

note that KPFS is known to be subject to spatial averaging. The determination of the CPD from local charging events as reported here may be more local and hence less sensitive to this effect. This might be particularly interesting, if the charging occurs at the tip instead of the sample side [184].

4.11 Conclusion

In conclusion, we showed that the oscillatory motion of a cantilever can be directly coupled to a charge-state transition of single molecules. In analogy to previous experiments on quantum dots, this allows one to extract information of the electronic states of molecules and its coupling to the substrate from AFM experiments. The analysis of dynamic charge response in FM-AFM-based spectroscopy as presented here may also shed new light on polarization effects in molecules in the future. Recently, the coupling between single-electron charging and the motion of a mechanical resonator has been demonstrated to lead to new exciting phenomena [187, 188]. Our study shows that this research avenue is also open for single-molecule systems. In addition, the observed edge effects in mono-layered islands reported here offer an electronically fascinating feature, namely well-defined, straight island edges with molecules in strictly-alternating charge states exhibiting four hydrogen terminals repeatedly flanked with a pair of electron clouds.

In addition, we visualized the difference in AFM images upon charging from a suitable subtraction of images. The contrast reveals that the extra electron is delocalized over the entire molecule and suggests that the main contribution to the difference image stems from electrostatic interaction. The changes of force associated to the charging were quantified as a function of distance and were found to only weakly decay with increasing distance. Finally, we investigated the distance dependence of the threshold voltage required for charing. The analysis

based on a very simple model suggests that these dependences allow an extraction of the local contact potential difference as well as the tip-sample spacing.

5 A functional cell for molecular quantum cellular automata

5.1 Introduction

A cellular automaton (CA) is a collection of cells on a (finite or infinite) grid that evolve through a number of discrete time steps according to a set of rules based on cell's previous state and interactions with its neighbourhood. The update rules can be defined in number of ways and are then applied iteratively in arbitrary time intervals.

The shape of the grid on which a cellular automaton is computed is one of its most fundamental properties. The simplest grid is one-dimensional: it is just a line of cells. If two dimensions are considered, additional complexity is introduced, so a square, triangular, hexagonal or other grids are possible[1]. Actually, the grid can be in any finite number of dimensions. In general, each automata cell can take one of finite number of n distinct states[2] at a given time. Beyond having only one state, the simplest set is when there are two states (also called "colors"), forming a binary automaton. The neighborhood is defined as the set of cells which determine cell's evolution. The most famous CA is Conway's game of life, discovered by John H. Conway in 1970 [189]. The game of life is a binary CA with a Moore neighborhood (only adjacent cells are considered) which generate patterns that seem to be

[1] In most cases, however, these CA are equivalent to a CA with a square grid with special rules

[2] Commonly an integer.

"alive". Although initially the propagation of game of life generations was performed by hand, very soon the advances in computing power allowed more extensive patterns to be investigated.

The quantum(-dot) cellular automata (QCA)[3] paradigm proposed by Lent and coworkers [193, 194] exploits the arrangement of individual electrons for processing information instead of using conventional current/voltage based technology. Advantages include small dissipation, high device density and improved switching speeds up to THz. It has been constructed in analogy to CA, but the model of CA evolves in steps while real systems react continuously. In the original concept, the basic cell is usually envisioned as a rectangular ensemble of four possible sites occupied by two extra electrons that can tunnel between the sites, but are always positioned at diagonal sites as a result of their mutual electrostatic repulsion[4]. Therefore, the cell in isolation has degenerate ground states, representing logic 0 and 1. If a cell is placed in vicinity of another cell with a fixed electron's positions it will align its electrons in the same way as that of the other cell i.e. the interaction with the neighboring cell will lift the degeneracy resulting in one well-defined ground state (Figure 5.1). In that way, the information can be transferred along a line of cells only based on this interaction. Experimentally, the first functional electrostatic QCA cell was demonstrated back in 1997 [195]. This was followed by realization of the elementary circuit elements, a digital logic gate [196], small binary

[3]The term refers to a physical implementation and should be distinguished from the models of CA that perform quantum computation. The main difference is that QCA in the latter sense requires quantum mechanical phase coherence on the whole grid, while in the former only inside a single cell, whereas the interactions between the cells are classical. Anton Zeilinger and Gerhard Grössing were the first to introduce the concept of quantum cellular automata [190], but the first example of quantized CA was given by Feynman in 1982 [191]. A mathematical definition of a QCA was given by John Watrous in 1995 [192].

[4]It is obvious that the two electrons are going to occupy antipodal parts of the cell because of the energy cost associated with bringing them in proximity. They can tunnel within the cell but no tunneling is possible between the cells.

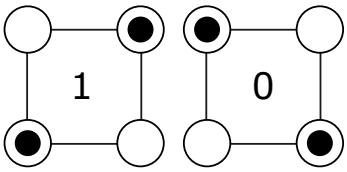

Figure 5.1: Anatomy of a quantum cellular automata (QCA) cell and binary interpretation. QCA is made of square cells with exactly four potential wells located at each corner. Only two electrons are locked in and can reside in two opposite wells.

wire and shift register [197]. In those experiments the sites were realized by quantum dots and owing to their very small charging energies, the experiments have had to be performed at sub-Kelvin temperatures. QCA can be also realized by closely spaced nanometer-domain magnets [198, 199].

For a room-temperature QCA device to be achieved, the energy spacing has to be increased by reducing the cell size to the molecular or even atomic scale. In this respect, the recently realized QCA based on the controlled formation of dangling bonds on a silicon surface [200] represents a leap in this development. The smaller the cell, however, the more critical is the correct alignment and spacing of neighboring cells for a correct implementation of its function. This poses a severe challenge in implementing molecular-based QCA, because all cells must be positioned with (almost) atomic scale precision. Self-assembled monolayers of molecules allow for such a precise mutual atomic-scale alignment of zillions of molecules, however, implementing a function in QCA requires particular structures of aligned cells and not just extended monolayers thereof.

This major obstacle in realizing molecular QCA can be solved by introducing a novel concept as demonstrated here. The novel concept is based on implementing and activation of the molecules to become an active cell. This way, one can still make use of the precision and

reproducibility in the molecular alignment from self-assembly, but at the same time realize specific QCA structures and thereby program certain functionality. In the realization demonstrated here, the activation of molecules is achieved by the creation of vacancies next to the activated molecule. However, this concept is much more general and could be also implemented differently, e. g. by addition or removal of a ligand on a functional molecule.

The two states of each cell is not implemented as usual by a charge rearrangement inside the cell, but by an exchange of a single electron between the substrate and the molecule (chapter 4 and Ref. [182]). Further, our work demonstrates that very complex functionality can be encoded into only few interacting molecules and, hence, the successful implementation of simple molecule-based quantum cellular automata (MQCA) behavior.

5.2 Activation of the molecules by patterning the cell

1,6,7,12-tetraazaperylene (TAPE) [162] (see Figure 5.2a for its chemical structure) form self-assembled monolayers on a monocrystalline Ag(111) substrate [182]. This self-assembly is guided by hydrogen bonds of C-H$\cdots$N contacts and results in a regular array of molecules, in which all molecules experience an identical environment (section 4.2). Contrary to that, along the periphery of the island the molecules differ in the number of nearest neighbours. Those of the molecules along the island edge that have their two lone-pairs of the nitrogen atoms unmasked along the edges, are found in a charge state different from the one of all other molecules in equilibrium and can be transiently charged by means of the electrostatic field brought about by a scanning tunneling microscope tip (chapter 4 and Ref. [182]). Such

molecules that facilitate charge transitions are labeled as Q and all other molecules as A.

Unmasking the lone-pairs of the nitrogen atoms of a specific molecule deep inside an island is also possible in a controlled fashion by selected removal of one of the neighboring molecules. We employed STM manipulation to remove individual TAPE molecules from the array (see section 5.6) [50, 79] creating vacancies. Indeed, two molecules next to a vacancy are transformed from A to Q as evidenced by their larger apparent height in low-voltage STM images, see Figure 5.5a.

To investigate the electronic properties of the molecular structures around a single vacancy, we measured a set of differential conductance ($\mathrm{d}I/\mathrm{d}V$) spectra at different positions as shown in Figure 5.5b. The observed features can be rationalized as follows. At the small spot of clean Ag(111), that is, at the vacancy itself, there is a confinement of the surface state as observed before [50]. The two Q-type molecules next to the vacancy show a *single*, sharp dip in $\mathrm{d}I/\mathrm{d}V$ at negative voltage V at around $V \approx -1\,\mathrm{V}$. This dip marks the charge state transition induced by the electric field of the tip, as explained previously [150, 182]. Repeated experiments show that the exact voltage threshold for the charge transition depends the tip-sample distance, but also slightly varies with variations of the tip apex, most probably determined by its exact shape and work function.

In contrast to island edges, where only every second molecule is of Q-type, the artificial and controlled vacancy creation inside islands facilitates the formation of Q-type molecules in direct vicinity to each other. Various of such structures of different complexity are exemplified in Figure 5.2b. Henceforth these structures are labeled according to the number of Q molecules in direct vicinity to each other acting as cells of the MQCA as dimeric (D1-D8), trimeric (T1-4 and T'1-4) and quadromeric (Qu1 and Qu2). For dimers D9 and D10 (and their mirror-symmetric counterparts, not shown), it was observed that they are not composed of Q molecules, but only A. This result can

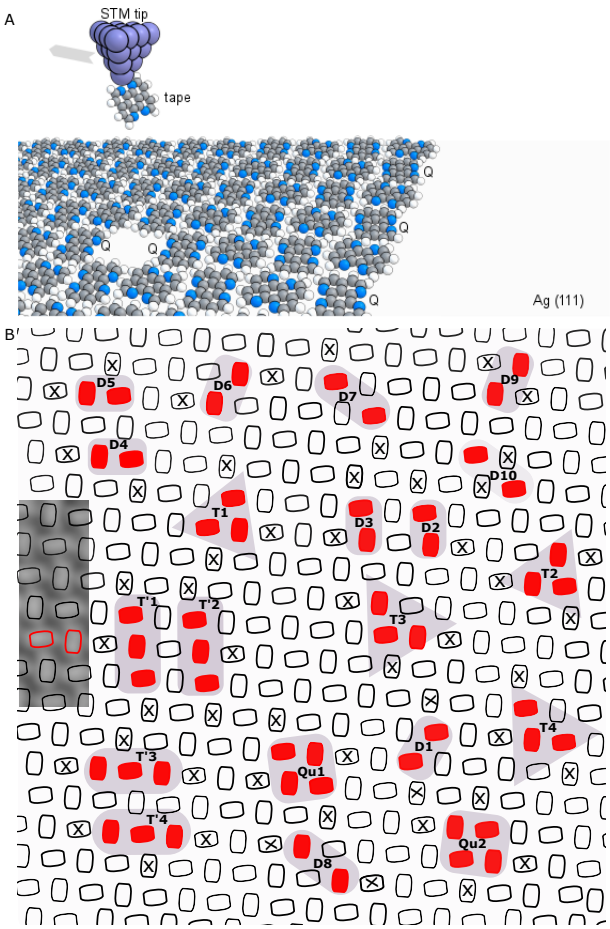

Figure 5.2: (A) Schematic representation of the construction of a single well and pair of Q molecules. Every second molecule at the edge is Q-type. Q molecules are formed in the interior of the array by removing single TAPE via STM tip (chemical structure of TAPE can be seen). Lower panel (B) illustrates the patterning of nanostructures investigated in this work. In the left part, an experimental STM image is shown with the model overlaid. Removed molecules are crossed and those colored in red are Q.

be rationalized by considering the number and type of the neighbours surrounding the molecules.

5.3 The charge state evolution: dimeric structures

An important prerequisite of cellular automata is the mutual interaction of neighboring cells, which we will address next. The simplest structures consist only of two molecules interacting with each other. As the self-assembled islands do not show a square lattice, but one with $\approx 80°$ angles (see section 4.2), there exist eight types of dimeric cell structures as mentioned in the previous paragraph.

Figure 5.3a shows a constant current image of the dimeric structures D1 and D2. Above the centers of the molecules labelled with numbers, $\mathrm{d}I/\mathrm{d}V$ spectra were recorded. For an isolated Q-type molecule which has a single vacancy as a neighbour (molecule **1**), the spectra show a sharp dip at a negative voltage V of about $-0.75\,\mathrm{V}$. This value marks the critical electric field that leads to a charge transition, as explained above. The overall shape of the spectrum has not changed significantly for molecules **3**,**4** of D1, except for a slight shift of a dip to the more positive bias voltages. The spectra measured on the molecules forming the dimeric structure labeled D2 do no resemble that of a single Q or D1. First, the spectrum **6** hosts a dip shifted to even more positive bias voltages, close to -0.4 V, and second, the spectrum **7** demonstrates a very rich structure, consisting of many dips and peaks. For the remaining structures D6-8 we have not observed quantitative differences as compared to D1, while the structures D3-5 show spectra very similar to the ones of D2 described above.

As there are two molecules in the dimeric structure D2, we have to assume two molecular levels, ϵ_6 and ϵ_7, that can be shifted across the

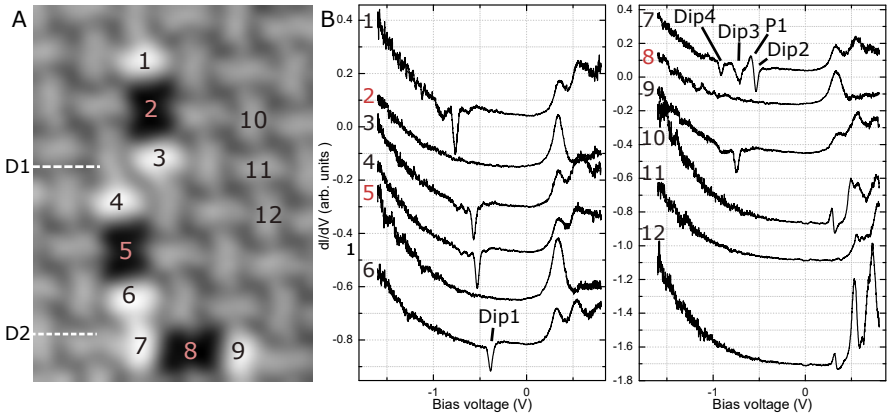

Figure 5.3: (A) Constant current STM image of a molecular island interior after removal of three molecules to form dimeric structures D1 and D2 (Imaging parameters $I = 0.9\,\mathrm{nA}$, $V = 0.2\,\mathrm{V}$). (B) The $\mathrm{d}I/\mathrm{d}V$ spectra recorded above the molecules and areas of clean surface. Tunneling gap was set with $I = 0.9\,\mathrm{nA}$, $V = 0.2\,\mathrm{V}$ above the middle of one of the charged species before the feedback was turned off. The curves are offset for clarity. All spectra were taken with lock-in modulation at 223 Hz and $V_{rms} = 15$ mV.

Fermi level [5]. In the formalism of the many-body theory discussed in chapter 3, we can couple these single states in combined many-body (MB) states. If we do not consider spin degrees of freedom and assume that only one state per molecule is involved, for N molecules exactly 2^{N} of these MB states exist. In the most simple case of the dimeric structure discussed so far, we have four possible states, as only one electron can reside in one molecular state. In order to visually represent MB states, we draw a box for every constituent state that can either be empty or filled with a circle, which represents an electron (Figure 5.4a).

[5] As the molecules experience slightly different environment, the energies of these two levels are not necessarily equal. From the analysis that was made in chapter 4 we know that the energy levels need to be few tens of meV above the Fermi level of the substrate without electric field applied in the junction.

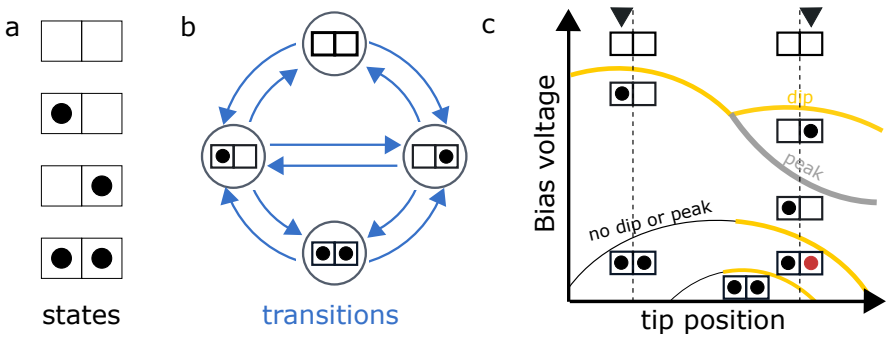

Figure 5.4: (a,b) Representations of quantum many-body states and transitions. (c) The accompanying scheme shows the expected electron occupations at different tip positions above dimeric structure. For the coupled many body states the origin of the grey band feature should correspond to the difference in occupation for the two 1 particle MB states.

In the case of an isolated Q molecule, the sharp dip in the spectrum indicates a transition of the charge state. In analogy, every dip and peak observed in the more complex structures will likewise indicate *transition* between different MB states. Figure 5.4b illustrates all possible transitions between the four MB states of D2. The total electron occupation can be determined using constant current imaging. From a set of STM images at different bias voltages we know that both molecules in D2 are neutral for any voltage being on the positive side of all peaks and dips in the spectra, as they have larger apparent height as compared to the rest of the interior of the molecular island. On the other hand, both molecules are charged for negative bias voltages far on the negative bias side ($V < -1\,\mathrm{V}$), as they than appear identical to A. Therefore, we can assign the two outermost MB transition to fully occupied and fully unoccupied states, respectively. We rule out any transitions directly between these two states.

In the STM experiments, the electric field acting as a gate potential for charging is largest beneath the tip. In general, the total potential

drops off almost entirely in the vacuum gap between tip and molecule, and only a very small fraction $\alpha(x, y, z)eV$ drops between surface and molecule. The potential drop can be controled by varying the tip-molecule distance: when distance between the tip and molecule is reduced, α increases, and so the electric field. For that reason, we should differ a case when the molecule is directly below the tip, and when it is not.

As discussed above, at sufficiently large negative bias voltage the transitions to the 1 particle states are opening, enabling electron tunneling from the substrate into one of the molecules in D2. Which of the two molecules will be first charged depends on a magnitude of the electric field at the molecule, that is, the location of the tip and the bias applied. First, when the tip is on top of the molecule **6** and bias voltage equals Dip1, **6** becomes switched in its charge state - from being neutral to anionic. At the more negative bias voltages, the 2 particle state becomes accessible enabling electron tunneling into **7**. As the occupation of the molecule beneath the tip remains the same, no signature of this transition in the spectra (neither dip or peak) is observed (see Figure 5.4c).

Based on the analysis made so far, for the tip being above the molecule **7**, we would expect to see a single dip. Remarkably, as the experimental spectra shows, not only one dip is observed, but three, where first two are separated by a peak[6]. In analogy to **6**, the first dip (Dip2) can be associated with charging of the molecule beneath the tip i.e. the injection of an electron into the molecule **7**. Decreasing voltage further would increase the electric field above the neighbouring Q molecule, until eventually tunneling into the next MB state becomes available. Simultaneously with charging of **6**, the molecular levels of **7** will be shifted to higher energies due Coulomb interaction. If ϵ_7 is pushed above the Fermi level of the substrate, the electron will tunnel out of this level - that is, the molecule discharges. Hence, in this process

[6]This dip-peak-dip features are more obvious for the T and Qu structures.

an electron is removed from **7** and one is added to **6**. A sharp peak P1 in the spectrum is due to an increased current upon crossing this transition.

By comparing charging lines of **6** and **7** (the bias voltage of Dip1 and Dip2) we realize that the former requires much lower electric field to be charged for the same tip-molecule position. This does not come as a surprise as the molecules in D2 experience slightly different environment. The transition from one 1 particle to another 1 particle MB state is favored over a direct transition to the 2 particle state for the particular set of bias voltages and tip positions, which is the effect of tunable coupling on the energy landscape of dimeric structure. Finally, we assign Dip3 to tunneling into the 2 particle MB state. This is illustrated in Figure 5.4b and c.

Although this model accounts for four transitions identified on D2, it fails to explain the final suppression of current (Dip4). Including spin degree of freedom may resolve that issue, as the number of states and transitions will increase. For a dimer, there will be 9 many-body states (of which two pairs and a set of three are degenerate) giving rise to one additional transition. The 2 particle ground state spin configuration can be either spin-singlet or spin-triplet, depending on the coupling constant. Spin exchange could change its sign in the presence of the electric (or magnetic) field for a wide range of coupling. In that terms Dip4 could be assigned to triplet-singlet transition. The fingerprint of such effect will be a large drop in the differential conductance.

5.4 Lateral-spectral and constant-height maps: trimeric structures

Over the last few decades, a lot of effort has been made to understand coupled QDs and control their properties [201–206]. In a so-called *sta-*

bility diagram[7], where the current through the QDs is given as a function of the gate voltages, the information about the charging energies, mutual coupling and gate lever arms is contained. In general, the stability diagram for a system that has N coupled dots is N-dimensional. Slicing this space in any two-dimensional plane reveals lines where the electrochemical potential of the leads matches that of QDs. Lines of constant electrochemical potential can meet, and when the coupling is present between the dots, point of intersection splits into two or more points, demonstrating what is known as *avoided crossing*.

Figure 5.5c shows an STM image after removal of three molecules (structure T1). As mentioned in section 5.2, those three vacancies could be as well formed such that the Q molecules are not arranged in a bent configuration, but in a linear form (T2, Figure 5.5f).

In the STM, when the tip is scanned across the surface, the lever arm for each molecule in the structure is changing. Because a single electrode is used, sweeping bias will be analogous to changing gate voltages. In order to access a part of the stability diagram, we measured differential conductance versus sample bias voltage spectra along certain directions [207, 208]. Figures 5.5d,f and h show these lateral spectral maps measured along the lines indicated in the topography images (top). Yellow and red colors in the map correspond to NDC and green and blue to positive differential conductance. Additional to curved bright lines, corresponding to the charging dip shifting to higher voltages as the tip approaches the center of a molecule, a very puzzling pattern is seen, suggesting complex switching behaviour.

The constant height $\mathrm{d}I/\mathrm{d}V$ maps recorded at fixed sample bias voltages are also, in a way, similar to the stability diagrams (Figure 5.6). This is because the level arm, as pointed out few times before, is position dependent and is different for each Q. In maps, the avoided-crossings are observed when the charging rings deviate from the circular symmetry or if they change their intersection points. This can be

[7] Example is e.g. Figure 3.3c

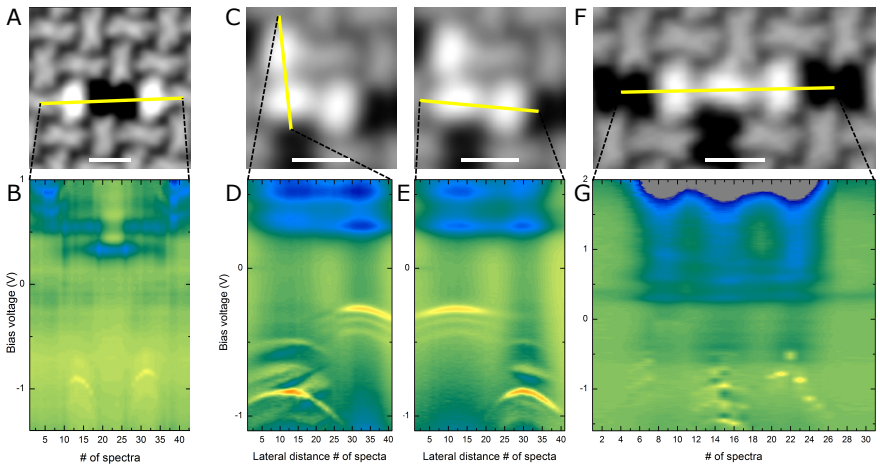

Figure 5.5: (A) Constant current STM image of a single vacancy and a pair of Q molecules ($I = 2\,\text{nA}$, $V = 0.16\,\text{V}$). (B) A set of differential conductance ($\text{d}I/\text{d}V$) spectra measured along line shown in (A): the spectral map. It is important to note that two bright curved yellow lines in the map that represent molecular ionization have their maximum at approximately same voltage. (C) Constant current STM image of T1. Left and right images are the same ($I = 2\,\text{nA}$, $V = 0.16\,\text{V}$). (D,E) Spectral maps demonstrating how a molecule, once charged, can be discharged due to the electric field from the neighbouring molecule and recharged again at more negative voltages. (F and G) Constant current STM image and spectral map of T2 ($I = 2\,\text{nA}$, $V = 0.16\,\text{V}$). All spectra were taken with lock-in modulation at 223 Hz and $V_{rms} = 15$ mV. (A,C,F) Scale bars 1 nm.

exploited to characterize the coupling strength between the molecules. As this work is still in progress, to understand mutual interactions in more details, we have to measure spacial maps with higher lateral resolution or complement our study with a DFT calculation of the system.

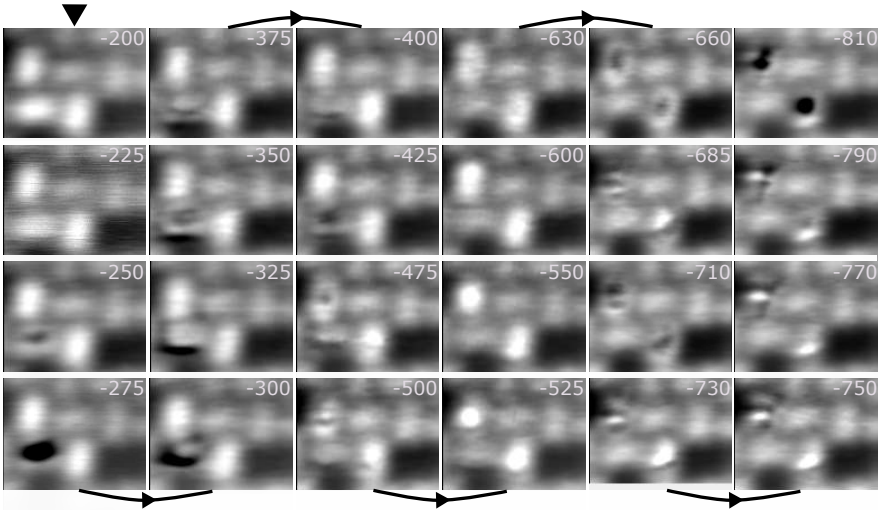

Figure 5.6: Constant height dI/dV maps of trimeric structure at different bias voltages (in mV). The onset for charging and discharging is traced by the elliptical (ring-like) and distorted contours. Lock-in modulation at 203 Hz and $V_{rms} = 5$ mV.

5.5 Bias dependent imaging: quadromers

As a final step, we produce a more complex geometry: Figure 5.7 shows a set of STM images at different bias voltages after construction of a windmill-like structure. The four molecules in the center appear bright for every positive bias voltage. As can be seen, at more negative voltages, the Q molecules of this structure become darker one by one, until voltages are reached where the whole structure, including the four molecules at the end points (which are single Qs), appear as A. For this particular voltage, the electric field in the junction is large enough to switch the molecule in its charge state no matter of its position in the structure (the relative position of the tip still matters and here, we refer to a position where the tip is atop the molecule of

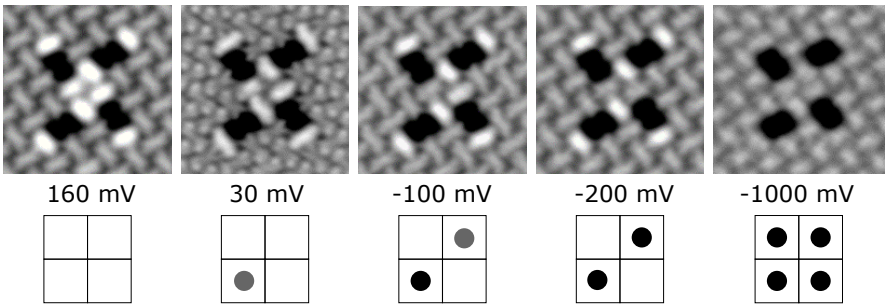

Figure 5.7: (top panel) Constant-current STM images of the Qu structure (windmill) at different bias voltages ($I = 0.9\,\mathrm{nA}$). (bottom panel) Schematic representation of the square cells filled with electrons.

interest).

Although the STM images of the windmill structure appear not to show any fuzzy features which are typically related to charging processes, the $\mathrm{d}I/\mathrm{d}V$ spectra and maps reveal a dynamic behaviour (Figure 5.8). The quantitative modeling of this configuration is out of the scope of this thesis. We therefore defer from a deeper explanation of the observed phenomenon.

5.6 Vertical manipulation

The manipulation experiments were performed by positioning the tip above the molecule to be removed (set point parameters: 2 nA, 160 mV) and lowering it straight down until the contact was made (bias is set to 30 mV and oscillation amplitude is 0.5 Å, with typical approach displacement of 2.9 - 3.3 Å). The efficiency of this procedure depends on the lateral tip position with respect to the molecule and tip geometry. Our combined STM/AFM system allows us to measure the current and frequency shift (Δf) simultaneously. Formation of contact is seen as a sudden increase in current and step kink in Δf.

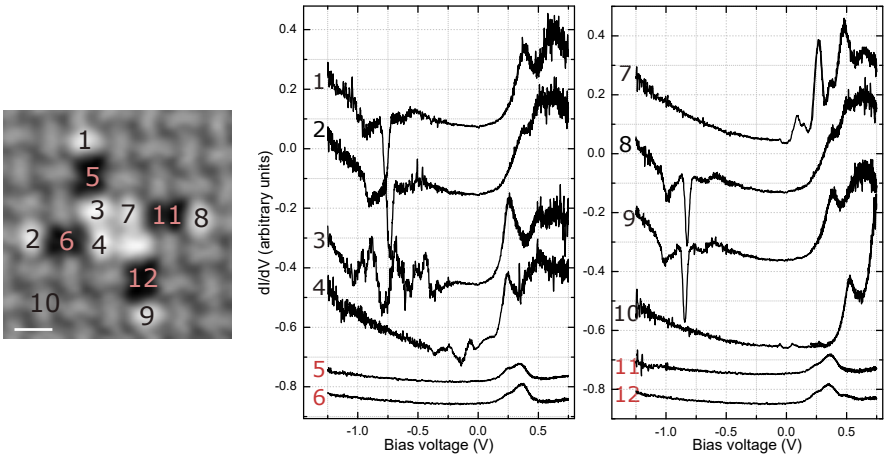

Figure 5.8: (A) Constant height STM image of the Qu structure ($I = 1.9\,\text{pA}$, $V = 0.16\,\text{V}$) showing where dI/dV spectra in (B) were recorded. All spectra were taken with lock-in modulation at 203 Hz and $V_{rms} = 18\,\text{mV}$ and are offset for clarity. Scale bar 1 nm.

Afterwards, the tip was retracted fast to the set point value and laterally moved to the area where the molecule was dropped off (typical parameters for this are: 300 mV, approach 12 Å). In total more than 200 molecules were extracted from the molecular islands in frame of this experiment, with a success rate higher than 90 % (any tip crash or picking of two or more molecules we count as an unsuccessful attempt). To confirm the tip was clean, we measured the spectroscopy of Ag surface state and LCPD on clean silver surface away from any islands or step edges and imaged targeted area before proceeding further. If the tip apex was not changed during the indentation attempt we repeated the procedure.

5.7 Conclusion

Here we address a critical issue in the realization of molecular quantum cellular automata, namely the *simultaneous* correct alignment and exact spacing of neighboring cells in combination with the programmability of the automata by controlled formation of complex and non-repetitive patterns of cells. The solution as presented here, lies in the combination of the creation of perfectly aligned inactive cells by self-assembly as a first and their selective and controlled activation as a second step. The self-assembly process will allow one to precisely control the underlying cell-to-cell alignment by means of synthetic chemistry. Whereas here the activation took place by vacancy formation, in the future, other mechanisms as e. g. the selective removal of ligands can be envisioned. We demonstrate that automata consisting of only few cells already show rich switching behavior.

6 A rocker switch formed by anchoring a single molecule to insulating surface

In this chapter, it will be shown how a real space investigation of a singly charged tetraazaperylene molecules adsorbed on an ultrathin insulating sodium chloride film grown on a copper substrate reveals a two-level system that can reversibly change between configurations, resembling the motion of a rocker switch.

6.1 Introduction

Switches are components that can interrupt or divert the signal depending on a factor that is set externally. In more general sense, the same term is used to describe systems that have at least two metastable states. These states need to be separated by a considerable barrier, such that no transition from one to another is occurring spontaneously. Additional prerequisite for a system to be considered as a good candidate for a switch in terms of usability, is the reliability of the switching process: the switch should endure many switching cycles and, most importantly, stay unaltered by reading out of all the states.

Present-day computers are based on encoding the binary information as **ON** and **OFF** states of bits that constitute switches in the above

definition. At the beginning of classical computing, electromechanical relays were used as the switches, later replaced with vacuum tube triodes and finally, by the modern transistor. If the transistors are ever going to be shrunk to the dimensions of a single molecule [209], hundreds of billions of them will be able to fit onto a single chip, increasing the computational abilities by many orders of magnitude. This will, however, inevitably bring additional challenges in terms of dissipation of energy, higher sensitivity to temperature changes and electromagnetic interference, which is detailed more in the chapter dealing with the molecular quantum cellular automata (chapter 5).

Over the past decades, in a field of surface science, switches have been intensely investigated. Employing STM and AFM a variety of molecular switches on surfaces has been realised. Based on their properties they were switched between two or more states triggered by diverse external stimuli: tunneling current [210–212], electric and magnetic fields [213, 214], light [215], heat [216] and mechanical force [216, 217]. Switches based on change in conformation [213, 218], charge and spin states [60, 72, 123, 144, 219], site displacements [220], bond formation [221] or dipole orientation [222, 223] were demonstrated. Thus far, this research has mainly been focused on implementing the switching function into the molecule itself. However, for a molecular switch to be used as a component of a future electronic device, its incorporation will entail contacting the switch to the substrate, other molecules and most likely to external electrodes as well. On the one hand, adsorption can suppress switching or lower the switching efficiency [224], on the other hand, interplay between the substrate and adsorbates may open up completely novel functionality. For instance, Kim *et al.* demonstrated structural modification of the Ge(100) surface as a result of a molecular motion [225]. Hagen *et al.* proposed a switching mechanism mediated by the substrate for photoinduced isomerization of tetra-*tert*-butyl-azobenzene molecules on Au(111) [226]. In a study by Schutte *et al.*, PTCDI molecules were pushed back and forth over oxygen rows of the unreconstructed titania (110) surface

with the apex of the AFM tip to form a switch [227].

In most of the above-mentioned experiments switching was performed on metal surfaces. A potential integration of a switch into a molecular electronic circuit would require suitable support, capable to electronically isolate components from each other i.e. to remove undesired coupling and avoid interactions with the environment. Such control can be achieved through fabrication of a switch on a semiconductor [228–231], bulk insulator [227], or an ultrathin insulating film supported by the metal substrate [221].

Here, we report a molecular switch based on the motion of a single tetraazaperylene molecule bonded to the topmost layer of bilayer insulating NaCl films on a Cu(311) surface at 7 K. The inclined molecule switches back and forth between the two equivalent conformations. The bistability is enabled by a bond formation and rupture between the admolecule and cations in the insulating layer, with switching direction controlled by positioning the tip slightly off-center above the molecule and initiated by applying voltage pulses of according polarity. Submolecular AFM imaging with CO functionalized tips provides information of the geometry, namely the tilt and adsorption position in both of the switching states.

6.2 Methods

Experiments were carried out on sodium chloride deposited onto a Cu(311) single crystal held at 100°C and previously cleaned by repeated cycles of annealing and sputtering. Low amounts of the 1,6,7,12-tetraazaperylene molecule ($C_{14}H_8N_4$, TAPE, chemical structure is given in Figure 6.2) [162, 182] were deposited on a surface by thermal evaporation at $T_{\text{sample}} \sim 7\,\text{K}$. Both, the substrate and adsorbate have been introduced in sections 2.4 and 4.2, respectively. All measurements presented here have been carried out on the NaCl bilayer.

6.3 Adsorption sites on a bilayer NaCl/Cu(311)

In STM, single molecules are identified on the substrate as oval protrusions in topography. At very low coverages, isolated molecules are randomly distributed indicating the diffusion barrier being high enough to prevent any mobility at 7 K. Low-bias imaging (within the gap) reveals the presence of six distinct adsorption orientations on a bilayer of NaCl: they are denoted as P, D, S, whereby S is further classified to four categories: I - IV (Figure 6.1). The images show a slight difference between them: P and D appear as a protrusion with a single depression next to it, while S is decorated with two smaller depressions. Upon adsorption on any surface, only those rotation symmetry operations with axes perpendicular to the surface and out-of-surface plane symmetry operations that match both the molecule and the substrate survive [232]. As the adsorbates have D_{2h} symmetry in a gas phase, the lower symmetry in the appearance of P and D (C_s point group) and S (C_1) must have its origin in the molecule-substrate interaction.

Ultrathin films of (100)-oriented NaCl islands grown on Cu(311) are terminated with nonpolar edges (alternating cations and anions) in second and any larger number of layers. If one of these edges is taken as a reference for measuring the azimuthal angle between the nonpolar direction of insulating layer and the long axis of the molecule, a statistical analysis reveals an angle of $45 \pm 3°$ for P and $135 \pm 3°$ for D species, making them parallel to the polar direction of NaCl. The P molecules are found on the surface with the highest probability, making roughly 50% of all observed structures, S and D making the rest (Figure 6.1b). Given the 4-fold symmetry of NaCl(100), P and D orientations are expected to be equally likely. Surprisingly, and despite having the exact same appearance as P, less then a few percent was found to be D. The peculiarity observed in orientation direction distribution of the adsorbed molecules, that is, the preference for P over D configuration and S I-II over S III-IV configurations, may be

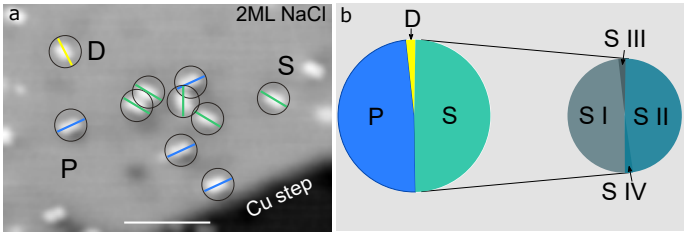

Figure 6.1: Low-bias STM imaging of tetraazaperylene molecules. (a) A large scale image after deposition. The species are labeled as P, D and S (Imaging parameters $V = 0.3\,\mathrm{V}$, $I = 2\,\mathrm{pA}$). Scale bar: 5 nm. (b) A pie chart showing percentage of adsorption angle distribution measured from 200 molecules. The distribution follows not a 4-fold, but a 2-fold symmetry.

explained as influence by the anisotropy of the underlying Cu(311) metal substrate. On Cu(311) the 4-fold symmetry is broken due to unidirectional stretch of NaCl(100) film of about 6 % of its bulk lattice constant, perpendicular to the intrinsic steps [233]. Hence, the substrate reduces the NaCl(100) surface cell square symmetry to rectangular, which explains why P is by far more likely than D. The same argument holds true for all four types of S molecules. S I-II are positioned with an angle of $\pm(22\pm3)^\circ$ to the direction of D, while S III-IV with that same angle in respect to orientation of P. The S III-IV types have been imaged in rare instances. For the S molecules the mirror planes perpendicular to the molecular plane are lost as they do not coincide with mirror planes of the NaCl(100) film, leading to a lower symmetry of the molecule-surface system in comparison to the NaCl surface itself, which results in a degeneracy in observed adsorption geometries. The rotation of S around its central axis relative to the high symmetry direction of the substrate (the Cu(311) surface has a mirror plane perpendicular to the $[01\bar{1}]$ direction) by a clockwise or counter-clockwise angle of about 22° keep it at the same adsorption geometry. Hence, the two observed orientations I and II of individual S molecules correspond to equivalent adsorption sites. S III and IV are related by the 90° rotation to two symmetrically non-equivalent

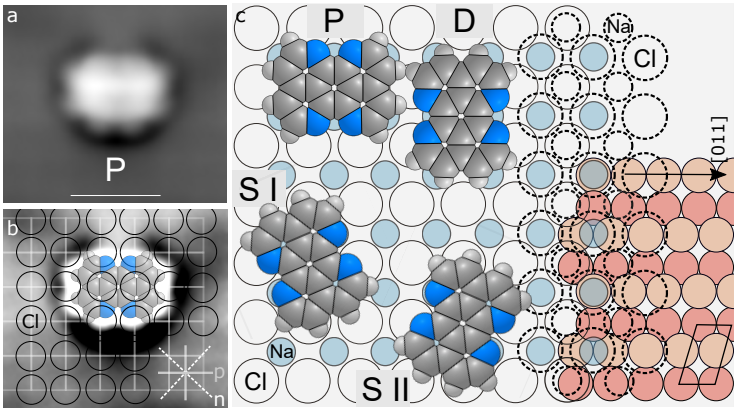

Figure 6.2: Adsorption sites of TAPE molecules on a bilayer NaCl supported by a Cu(311) surface. (a) Constant-current in-gap STM image of P-TAPE and the same area at different contrast (b) ($V = 0.3\,\mathrm{V}$, $I = 2\,\mathrm{pA}$). Images were acquired with a CO-terminated tip which enhanced the contrast as compared to a metal tip (an image of P with the metal tip can be found in Figure 6.3). Crossings of white lines in (b) mark Cl atom positions of the top most layer of NaCl, with indicated nonpolar (n) and polar (p) directions. According to the previous STM studies, the nitrogens appear as depressions in molecules on the NaCl film, reflecting lower tunneling probability. The reduction of symmetry for P from expected C_2 to C_s, can be attributed to the different local environment experienced by different parts of the molecule and/or small sliding displacement from a hollow site. Blue, grey and white colored spheres correspond to N,C and H atoms, respectively. (c) Molecular adsorption geometries (top view) as deduced from the scans. Two different reconstructions for the monolayer of NaCl exist (p(3x2)-I and p(3x2)-II) but only the interface layer that corresponds to the p(3x2)-I structure is shown (full line circles indicate Na (purple) and Cl (transparent) ion positions in second and dashed circles in the first layer), together with a portion of the bare Cu(311) surface in the lower right corner (light and dark colored circles represent Cu atoms in the first and second layer, respectively). Although both ordered structures of NaCl coexist on the surface for both monolayer and bilayer, no differences can be seen between them in atomically resolved images. Scale bar: (a) 1 nm.

sites S I and II, respectively, but likewise this two, both have the same adsorption sites.

We determined the adsorption site of P using AFM imaging with STM feedback on. As reported earlier, this mode enables atomic resolution on NaCl without disturbing the adsorbate [234, 235]. Since the nitrogen atoms in the TAPE molecule are considered to carry partial negative charge, it is expected that they will be attracted by positive Na^+ ions of the surface, resulting in a geometry in which (i) the central carbon ring is adsorbed above the Na-Na bridge site and the molecule's longer axis is aligned with a polar direction or (ii) the central ring is adsorbed on top of Cl ion and the two diagonal molecule's nitrogens are found above two Na atoms of the substrate (see Figure 6.2c). Even though such polar interaction between the nitrogen atoms in the molecule and the NaCl surface is expected to be relatively weak, it has been suggested that it may play a significant role, for instance, in the diffusion behaviour of the adsorbates [236]. Figures 6.2a and 6.2b show constant-current STM topography measured with the CO tip and the simultaneously acquired frequency shift image for P-TAPE. The faint maxima corresponds to the Cl atom position in the lattice [234]. The models of the adsorption sites deduced from the scans are shown in Figure 6.2c and are in the good agreement with expected geometries and discussed analysis in terms of symmetry given in the previous paragraph. In the rest of the text, we will only focus on P orientation.

6.4 Manipulation of the charge state and adsorption geometry

By means of voltage pulses it is possible to modify P-TAPE molecules. The procedure is depicted in Figure 6.3a,c for a voltage of positive polarity applied to the junction. During the voltage ramp, where the

STM tip is positioned directly above the center of TAPE molecule, a sudden change in current occurs. Posterior imaging of the same area confirms this: The molecule now appears surrounded by a dark halo, showing small protrusion on one of its side (Figure 6.3c). This process is highly reliable with a success rate larger than 95 %. As an alternative to the aforementioned procedure, the molecules can be switched with the same outcome only by scanning at relatively high positive bias voltages ($\geqslant$ 1 V). Interestingly, we find that S-TAPE sometimes has a tendency to rotate under this imaging conditions to P-TAPE, and subsequently change its appearance.

There are few possible reasons for TAPE appearing different after the manipulation process. A change in the tip apex was ruled out as all other neighboring molecules in the surrounding kept the same appearance. The process is found to be reversible by applying a voltage pulse of negative polarity and as no fragments were observed, the possibility of intramolecular bond dissociation was also excluded. The tunneling electrons may induce a change in the charge state, or a change in conformation, or as quite common for a case of molecules and atoms on NaCl film both of them [144]. It is, therefore, of crucial importance for the understanding of the switch to determine the charge state of a molecule.

The technique of using the scattering pattern of the interface state to reveal the charge state of adsorbate on a NaCl [123, 144] is not applicable in the case of NaCl/Cu(311). Instead we apply the more direct method based on characterization of electrostatic forces: KPFS [128]. Our data indicate that TAPE becomes negatively charged upon switching. The experimental observation of a depression forming around the molecules after the manipulation is consistent with this findings. Previously, this has been seen for e.g. change in appearance of the Au atoms on NaCl after charging [37, 144] and apparent height decrease for tetraazaphthalocyanines [123]. Large ionic relaxations within the NaCl film can create an attractive potential for additional charge which is further stabilized by the electronic polarization and addi-

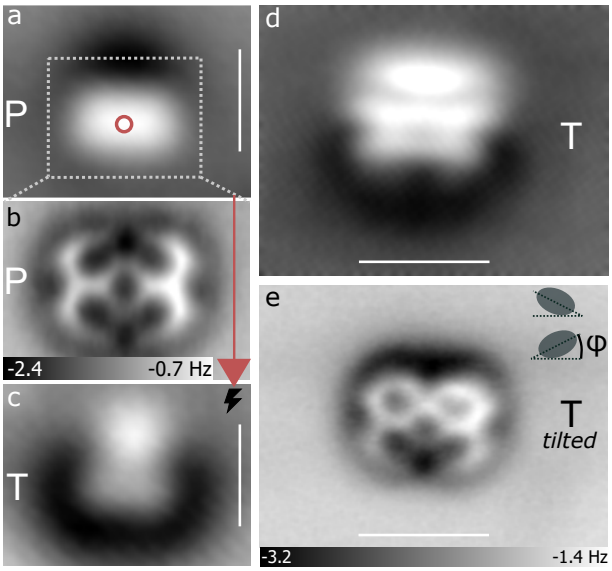

Figure 6.3: Anchoring of a molecule to the insulating surface. (a) Constant-current STM image of P-TAPE before the current pulse ($V = 0.3\,\mathrm{V}$, $I = 0.7\,\mathrm{pA}$) and (b) constant-height AFM image of the same molecule acquired in an area indicated with a dashed rectangle (the tip is approached by $\Delta z = 0.4\,\text{Å}$ from the set point above second layer of NaCl: $V = 0.3\,\mathrm{V}$, $I = 0.7\,\mathrm{pA}$. Circle indicate the position of the tip above the molecule during the application of the current pulse with the feedback loop switched off. (c) Constant-current STM image of the same molecule after the current pulse with the same imaging parameters as (a). (d) Constant-current STM image of the resulting species with a CO termination, producing enhanced resolution as compared to (c) ($V = 0.3\,\mathrm{V}$, $I = 1.0\,\mathrm{pA}$). (e) Constant-height AFM image of (d). The inset shows two mirror reflected geometries expected after the transformation. The angle ϕ is inclination between the surface and molecular plane. Scale bars: (a,c,d,e) 1 nm.

tional screening in the underlying layer. The interpretation of having two different geometrical configurations of the molecule-NaCl system is supported by the fact that both species are stable for at least several hours under typical measurement conditions. The change in the

charge state and further consequences of this result will be discussed elsewhere.

In order to identify any conformational change, we performed constant-height AFM imaging in noncontact frequency modulation mode, in which intramolecular resolution is nowadays routinely achieved with functionalized tips oscillating at a sub-Ångström amplitudes. As displayed in Figure 6.3b, all five rings of TAPE molecule are unambiguously identified having almost the same contrast, implying that the molecule is adsorbed in a planar geometry. A long-range attractive forces are responsible for the overall negative background, the short-range forces are responsible for a submolecular resolution i.e. a very small change in tip-molecule distance results in a significantly different contrast. By comparing scans before and after the charge-manipulation step (Figures 6.3b and 6.3e, respectively) it can be seen that the new species must corresponds to a different configuration, from now on referred to as T-configuration, characterized by the molecule being no longer parallel to the surface but *tilted*, as the brightness of one site is enhanced. As said, this is an indication that this part is more closer to the tip and Pauli repulsive force is stronger compared to the other end. Based on this AFM data and as evidenced by other observations discussed below, we propose a model as illustrated in Figure 7.4e: The Na^+ ion is forced to move upwards to coordinate with a pair of nitrogen atoms resulting in a tilt of the molecular backbone. Consequently, the opposing part of the molecules is tilted away from the surface plane - corresponding to the protruding feature in the STM image in Figure 6.3c.

To quantify the transformation, we measured the tilt of the molecular plane with respect to the substrate using force spectroscopy. For this, we acquired a set of frequency shift Δf curves at zero voltage as a function of tip-molecule distance z above the centers of the ring structures and determined where Δf has its minimum, as proposed by Schuler *et al.* [237]. The central regions of carbon and pyridine rings were chosen to minimize influence of CO bending, known to affect

Δf [238]. The adsorption angle was found to be $\phi \approx 10°$. Analogous to the Au^+ adatom switch reported recently [239], this new tilted adsorption geometry will give rise to two equivalent mirrored configurations because symmetry is reduced. Hence, a bistable behaviour is expected (see inset of Figure 6.3e).

6.5 Reversible bidirectional actuation of a molecular rocker switch

To explore the possibility to switch between these two conformations we employed STS. The reversibility of the switching process is illustrated in the sequence of STM images in Figure 6.4. It shows T-TAPE flipped twice after the bias pulses were applied above the molecule (to the right). It can be seen that the respective molecule behaves as a rocker - after the pulse, it is mirrored at a plane along the molecular axis (dashed white line): The bright spot attributed to nitrogens' lone-pairs turns to the opposite side. The switching direction is controlled by laterally displacing the tip from the center, closer to the depression (indicated with the black circle). A reversible interconversion between conformations is assumed to be based on the bond formation and rupture between the admolecule and metal ions in the insulating layer (illustrated in Figure 6.4d,e.) We suggest the switching is being induced via multiple vibrational excitations by tunneling electrons, as it was characterized by a threshold value for the bias (for both polarities) that equals the energetic positions of the molecular states. Transfer of electrons to electronic level leads to a transiently neutral or doubly reduced molecule. Upon leaving the molecule the electrons deposit their energy to the vibration degree of freedom and could hence excite the molecule, thereby initiating the process. Here, the insulating film plays a crucial role: it provides metal atoms as bonding partners and increases the lifetime of additional electron on

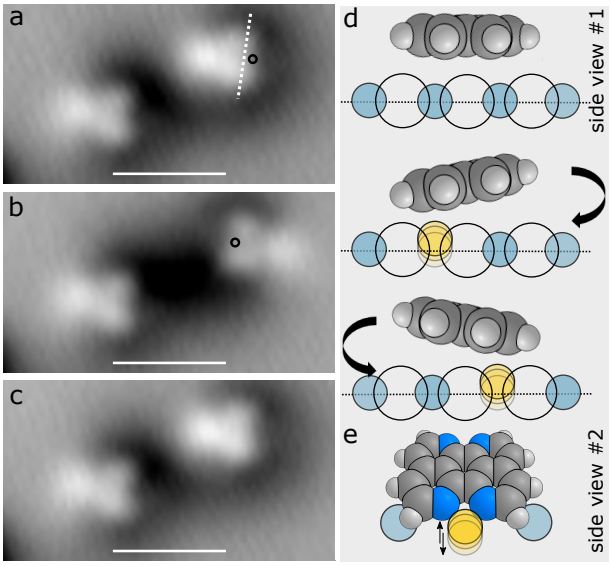

Figure 6.4: Bidirectional switching. (a-c) Sequence of in-gap topographical STM images revealing reversible switching of a Na:TAPE complex induced by tunneling electrons ($V = 0.5\,\mathrm{V}$, $I = 0.9\,\mathrm{pA}$). Electrons are injected at a fixed lateral tip positions indicated with the black circles (the dashed line is the switching axis). A sudden change of the tunneling current I marks a successful modification. The molecule on the left was used as a marker. (d and e) A tentative model before and after the complex formation as seen from the side positions 1 and 2; the interaction between the molecule and the substrate is dominated by the N-Na coordinative bonds. Ion-core positions of Na are represented with a colored sphere models. The color coding for the molecule is the same as used in Figure 7.2. Scale bar: (a-c) 2 nm.

a molecule due to reduced molecule-metal substrate interaction, thus giving rise to a higher quantum yield for the transfer to vibrations.

The crossover between *tilted* configurations was also induced at decreased tip-molecule distances with a scanning tip of our AFM at virtually no current. In the presence of the tip, a potential energy surface distorts until eventually one state becomes favorable over the other.

This might be attributed to deformation of the ionic film and relaxation of the molecular frame as the tip is approached to the molecule, or to a dipole-dipole interaction between the molecule and the tip, for example. According to the theory by Jelinek's group, the activation barrier for a silicon quantum dot switch can even disappear if the force enters the regime of the chemical forces [217]. Note that the potential landscape can change similarly under influence of the electric field, as was predicted in Ref. [240] and later shown by Grill's group [214]. The force induced switching does not allow the same degree of control of the process as demonstrated in the STM and surprisingly, in few cases, ends with $T \leftrightarrow P$ conversion. It is more than likely that the mechanical induced reaction depends on the tip height, lateral position and scanning direction, however, this is yet to be confirmed by mapping the three-dimensional force field. From there, the repulsive vertical and lateral forces required to actuate the switch can be extracted. A more detailed account of the switching mechanism, geometrical structure and nature of manipulation may be given by a theoretical modeling of the system in the future.

7 Regioselective dehydrogenative aryl-aryl bond formation

This chapter contains material already published in the following publication: N. Kocić, X. Liu, S. Chen, S. Decurtins, O. Krejčí, P. Jelínek, J. Repp, and S. X. Liu, 'Control of Reactivity and Regioselectivity for On-Surface Dehydrogenative Aryl-Aryl Bond Formation.' *J. Am. Chem. Soc.* 138 (2016), 5585.

Regioselectivity is of fundamental importance in chemical synthesis. Although many concepts for site-selective reactions are well established for solution chemistry, it is not *a priori* clear whether they can easily be transferred to reactions taking place on a metal surface. A metal will fix the chemical potential of the electrons and perturb the electronic states of the reactants because of hybridization. Additionally, techniques to characterize chemical reactions in solution are generally not applicable to on-surface reactions. Only recent developments in resolving chemical structures by AFM and STM paved the way for identifying individual reaction products on surfaces.

In this chapter, we exploit a combined STM/AFM technique to demonstrate the on-surface formation of complex molecular architectures built up from a heteroaromatic precursor, the tetracyclic pyrazino[2,3-*f*][4,7]phenanthroline (**pap**) molecule. Selective intermolecular aryl-aryl coupling *via* dehydrogenative C-H activation occurs on Au(111) upon thermal annealing UHV conditions. A full atomistic description of the different reaction products based on an unambiguous discrimination between pyrazine and pyridine moieties is presented. Our work

not only elucidates that *ortho*-hydrogen atoms of the pyrazine rings are preferentially activated over their pyridine equivalents, but also sheds new light onto the participation of substrate atoms in metal-organic coordination bonding during covalent C-C bond formation.

7.1 Introduction to the concept of regioselectivity

There are many synthetic protocols for the aryl-aryl bond formation, among which palladium-catalyzed cross-coupling chemistry is certainly most prominent in organic chemistry [241]. Nevertheless, the dehydrogenation, for instance between contiguous phenyls in phenylbenzenes, plays a similarly important role [242]. Notably the Scholl reaction [243–245], the dehydrogenative coupling under the influence of a Lewis acid, has often been used for polyphenylene compounds which are further converted to the corresponding polycyclic aromatic hydrocarbons (PAHs). These solution-based protocols paved the way for the preparation of a wide variety of π-extended PAHs by employing tailor-made oligophenylene precursors [246–249]. In a similar vein, noteworthy studies assessed whether the corresponding reaction mechanisms are based on the generation of a radical cation or an arenium cation. For example, Butenschön *et al.* initiated a discussion on the comparison of oxidative aromatic coupling and the Scholl reaction aiming to encourage further mechanistic studies [250]. Much less is known about a systematic examination on heterocyclic systems. Representative examples were exemplified by preparation of on N-doped nanographenes and graphene nanoribbons *via* cyclodehydrogenation of a dipyrimidyl-substituted precursors [251–253].

In contrast to the solution-based method, a complementary on-surface synthesis synthesis under UHV conditions enables the realization of unprecedented structures of PAHs that are otherwise unattainable [254–260]. A specific underlying growth mechanism has been described by

Cai *et al* [261]. It demonstrates the occurrence of an Au(111) surface-assisted dehalogenation reaction of dibromo-bianthryl (C-C bond formation by Ullmann coupling) leading to linear polyphenylene chains at 200 ° C which undergo a cyclodehydrogenation process upon annealing to 400 ° C, yielding structurally perfect and fully π-conjugated carbon nanoribbons. Depending on the precursor molecules, on-surface preparation of this type provides access to graphene nanoribbons with different widths and edge structures [262–266], including heteroatom-doped ones [267–269]. An intriguing question is, however, how a specific atomic configuration between reactant and metal catalyst controls the reaction process. In response, a recent study focused on the dehalogenation and C-C coupling mechanisms of a polycyclic hydrocarbon compound on a metal substrate covered with a monolayer of hexagonal boron-nitride [270]. To summarize, a key insight from on-surface reactions is, that there are no inherent limitations for this strategy to be extended to more complex systems, as far as the necessary precursor monomers can be synthesized. In practical terms, however, finding new routes to fabricate complex hetero-structures with for instance atomically precise N/C locations, still remains a challenge [271, 272].

A further important point is that the work, hitherto reported, does not yet adequately account for the possibility to steer catalytic regioselectivity [273–275], means to favor bond formation at a particular atom over other possible atoms, into the class of surface-assisted reactions. The on-surface C-H bond scission is generally not regiospecific when the molecules contain several C-H bonds [276]. Very recently, one approach is given with an experimental and theoretical study on cyclodehydrogenation reactions of tetraphenylporphyrin (2H-TPP) molecules on Ag(111). It has been found that the twofold symmetry of the 2H-TPP's core, which is defined by the position of the H atoms, determines the selective reaction outcome [273]. An alternative path for the regioselective formation of sophisticated structures is to apply a step-by-step connection of molecules which allows to connect them

in a hierarchical manner by a selective and sequential activation of different sites on their perimeter [277]. To achieve selectivity, these reactive sites must be incorporated in the initial molecular building block. In conjunction with the catalytic selectivity issue, the work of Hanke *et al.* draws our attention to cooperative effects. Cyclodehydrogenation corresponds to positive cooperativity, hence the probability of any given coupling is drastically increased if a neighboring coupling already exists [278].

An important consensus is that significant progress in the field of on-surface synthesis has mainly been facilitated by single-molecule characterization techniques such as AFM and STM. Recently, the chemical structures of individual molecules have been resolved by AFM which was enabled by the functionalization of the tip [82]. This method has paved the way of identifying individual molecules on surfaces in various contexts [234, 235, 279], and was soon after applied to *in situ* characterize and visualize on-surface chemical reaction products [221, 280–284].

In continuation of current research on fused heterocyclic compounds [285–288] such as tetraazaperylene [182] (see chapters 4,5 and 6), we set out to probe an even smaller tetraazapolycyclic precursor molecule, pyrazino[2,3-*f*][4,7]phenanthroline (**pap**) [289], for selective on-surface dehydrogenation and subsequent intermolecular C-C bond formation. This planar bis-N^N chelating molecule (Fig. 7.1) has so far exclusively been studied in the field of coordination chemistry acting as a bridging ligand to transition metal ions [290–293]. However, this heterocyclic molecule did draw our attention, firstly because its eight C-H bonds could be potentially differentiated in the dehydrogenative reaction pathways. Since two hydrogen atoms on the pyrazine ring may preferentially be activated over their pyridine equivalents, selective reaction sites are inherently incorporated. Secondly, subsequent intermolecular C-C bond formation can lead to larger heterocyclic compounds revealing atomically precise N/C locations. Here we present a combined STM/AFM investigation of an on-surface chemical reaction

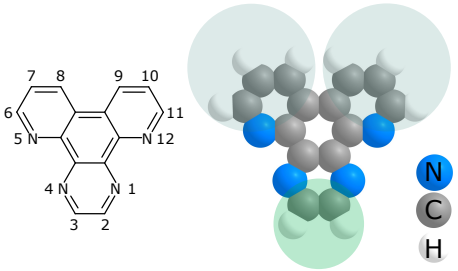

Figure 7.1: Molecular structure of pyrazino[2,3-*f*][4,7]phenanthroline (pap) with atom numbering. Highlighting examples of potential sites for selective intermolecular C-C couplings *via* on-surface dehydrogenation.

of the **pap** molecule under UHV conditions. This work demonstrates a clear discrimination between pyrazine and pyridine rings of the reaction products, thus giving convincing support for pyrazines' inherent reactivity playing a key role in the regioselective aryl-aryl dehydrogenative coupling.

7.2 Materials and methods

Chemicals. Pyrazino[2,3-*f*][4,7]phenanthroline was synthesized as described previously [289]. The high yield is in the range of 80–90%.

STM/AFM Measurements. For FM-AFM measurements, the apex of the tip was functionalized with a CO molecule and the images were recorded at sample bias $V = 0\,\mathrm{V}$ by measuring the frequency shift while scanning in constant-height mode. After preparing a clean Au(111) surface from cyclic sputtering and annealing to 550 ° C, **pap** molecules were deposited at a sample temperature below 10 K.

Simulations. The calculations of the free standing molecules have been performed within DFT as implemented in the SIESTA code [113]. The calculations are based on both the local-density approximation

(LDA) and the generalized gradient approximation (GGA). Core electrons are replaced by nonlocal norm-conserving pseudopotentials and valence electrons are described by linear combinations of numerical pseudo-atomic orbitals. An energy cutoff of 400 Rydbergs is employed and a double-ζ plus polarization basis set is used for the basis orbitals.

O. Krejčí and P. Jelínek from the the Nanosurf Lab in Prague performed total-energy DFT calculations using the FHI-aims code [294] to determine the adsorption geometry of **pap** molecules on a Au(111) surface. They carried out slab calculations: for the **pap** dimers optimization a 8×8 supercell made of four Au layers was employed to describe the Au(111) surface. From these, the three lower-most Au layers were kept fixed. A relaxation procedure was performed until the remaining atomic forces and the total-energy were below 10^{-2} eV/Å and 10^{-5} eV, respectively. Only the Gamma point was used for the integration in the Brillouin zone. All the calculations were carried out at the GGA-PBE level including the Tkatchenko-Scheffler [295] treatment of the Van-der-Waals interactions.

To simulate the high-resolution AFM images, a mechanical probe-particle AFM model [296] including the electrostatic interaction [297] was used. The frequency shift was computed from the simulated $F(z)$-curves using Giessibl's formula [167] using the experimental values of $A_{osc} = 50\,\mathrm{pm}$, $k_0 \approx 1.8 \times 10^3\,\mathrm{N/m}$ and a lateral stiffness of the CO molecule of $0.5\,\mathrm{N/m}$ with an effective charge on the probe particle of -0.05 elementary charges.

7.3 Sample preparation

The **pap** molecule was structurally characterized by single crystal X-ray measurement from its hydrated solid [292]. It is virtually planar; the maximum atomic deviation from the least-squares plane is 0.098 Å

and the mean deviation is 0.05 Å. First, the self-assembly behavior of **pap** on the Au(111) surface was investigated. The molecules were deposited at a substrate temperature below 10 K and the sample surface was imaged after an annealing step to room temperature. As illustrated in Figure 7.2, STM images of the surface show an average coverage of approximately one molecule per 3 nm^2. As is immediately apparent, the molecules form different types of self-assembled structures, including small clusters but also longer chains of molecules. While the self-assembled structure formation is not the focus of this work, this observation proves that even at room-temperature the molecules have enough mobility to aggregate in self-assembled structures. All structures can be rationalized in terms of C-H$\cdots$N hydrogen bonds formed between neighboring molecules.

To initiate the on-surface reaction, we annealed the sample to $(410 \pm 25)^\circ$ C for 1 min. Figure 7.3a shows a typical STM image of the surface after the annealing. From this and many other STM images in total 166 clusters were observed. Six different types of clusters, namely dimers (Di1, Di2), trimers (Tr1, Tr2), and tetramers (Te1, Te2) make up 94% of all structures, while no remaining monomers could be found on the surface. The limited size of clusters is in stark contrast to the self-assembled structures studied before the annealing step and a first hint towards the regioselectivity of the reaction. If all of the hydrogen sites would show the same reactivity, there would be no reason that no larger structures are formed as seen in the self-assembled structures. However, if one assumes that dehydrogenation mainly occurs at the pyrazine moiety of the molecule, clusters of limited size can be expected.

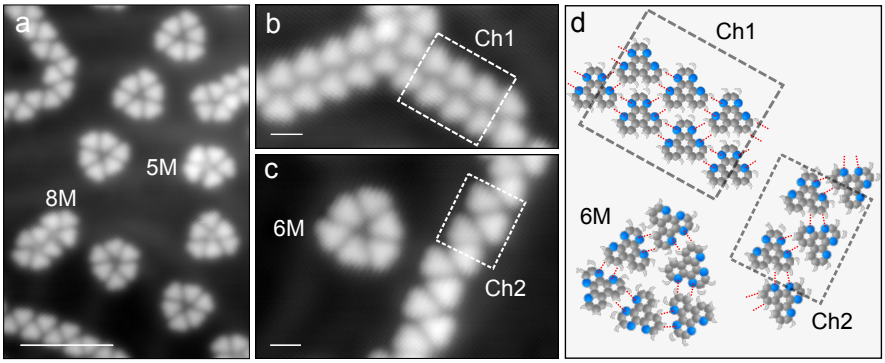

Figure 7.2: STM measurements of self-assembled hydrogen-bonded structures of pap molecules. (a-c) Typical self-assembled molecular clusters and (d) their proposed structure models with the same color code as in Figure 7.1. Imaging parameters: $V = 0.3\,\mathrm{V}$, $I = 2\,\mathrm{pA}$. Scale bar: (a) 5 nm and (b,c) 1 nm.

7.4 A discrimination of a pyridine from a pyrazine unit

To gain information about the regioselectivity from AFM in real space, one has to be able to identify the different sites within the molecule; in the actual context a discrimination of pyridine from pyrazine is necessary. Whereas for phenazine adsorbed on a copper surface the nitrogen can readily be identified inside the molecule [280], this is not directly apparent in the present case. That the substrate may affect the appearance of atoms in adsorbed molecules in AFM images goes in line with simulations of the AFM-imaging process performed for graphene nanoribbons doped with boron atoms [298]. There it was claimed that the difference in AFM contrast on boron atoms is only due to their different adsorption height as compared to carbon atoms. On the less reactive surface of Au(111) used here, it is therefore not surprising that no clear difference is observed. Nevertheless, the nitrogen sites can also be identified in the present case by two observations

as follows.

Within the triphenylene backbone of the **pap** molecule at four of six distinct atomic positions the nitrogen atoms are incorporated. The C8-C9 distance is slightly larger than the N4-N5 and N1-N12. On top, image distortions in AFM imaging with CO functionalized tips may influence the apparent atomic distances [43, 299]. Important in the current context is the prediction that electrostatic interactions contribute considerably to these distortions [296]. As the C-N bonds inside the molecule are expected to be slightly polar, AFM image distortions should slightly differ at the nitrogen and carbon positions in molecules. The distances between each two of these atomic positions in every edge of the molecules (see Figure 7.3) appear quite differently in the images. The distance in one edge is particularly longer (3.5–4.0Å) than those in the two other edges (2.3–2.9Å). From this observation, the carbon (long apparent distance between C8-C9, white arrowheads) and nitrogen (short apparent distance between N4-N5 and N1-N12, blue arrowheads) can be identified. This assignment is supported by DFT calculations and AFM image simulations as will be discussed further below.

In STM images, each molecule appears as a triangular protrusion. When directly relating the STM and AFM images of the same individual structures, one realizes that the nitrogen-substituted edges - as determined from the AFM distortions - appear smoother than the ones without nitrogen. Whereas at one of its three edges the contrast falls off relatively abruptly, at the two other sides this transition is smoother. This correlation between STM contrast and AFM-image distortions further supports the assignment of nitrogen positions inside the molecules.

Being able to identify the positions of nitrogens as discussed above, we now turn to the discussion of bond formation in different structures. From atomically resolved AFM images we extracted structural information, namely, which intermolecular chemical bonds were formed.

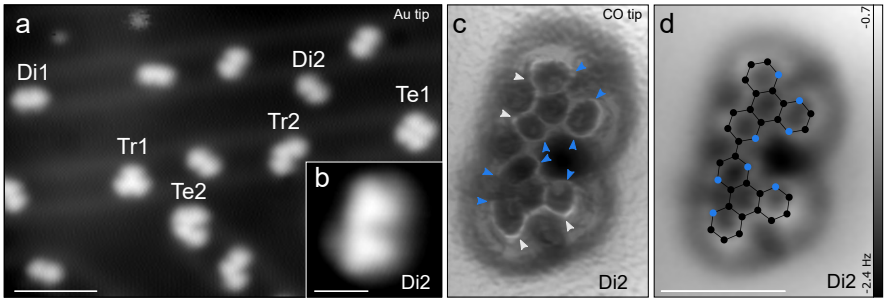

Figure 7.3: STM/AFM measurements of covalently-bonded structures. (a) STM image showing several different dimer (Di1, Di2), trimer (Tr1, Tr2), and tetramer (Te1, Te2) structures. (b) STM image of one of a Di2-dimer structure. (c and d) AFM images of the same Di2-dimer as shown in (b). The same AFM-image is displayed twice with (c) and without (d) being high-pass filtered to highlight the molecular structure. The two **pap** molecules constituting the dimer can be readily identified. The distances between each two marked (arrow heads) atoms in every edge of the molecules appear quite differently in the images. From this, the carbon (long apparent distance, C8-C9, white) and nitrogen (short apparent distance, N4-N5 and N1-N12, blue) can be identified. Based on this identification the position of the edges including the nitrogen atoms can be identified from STM images as the ones exhibiting a smoother contrast transition. In (d) the resulting molecular structure is overlaid with black and blue circles as carbons and nitrogens, respectively. Imaging parameters: (a) $V = 0.3\,\mathrm{V}$, $I = 1\,\mathrm{pA}$. (b) $V = 0.05\,\mathrm{V}$, $I = 1\,\mathrm{pA}$. (c,d) $\Delta z = 1.33\,\text{Å}$, Δz corresponds to a distance decrease with respect to a STM set point of I = 1 pA, $V = 0.05\,\mathrm{V}$ above the clean Au surface. Scale bar: (a) 5 nm and (b,d) 1 nm.

Figure 7.4a-e show the analysis of dimer structures. Irrespective of the AFM contrast indicating a covalent bond, the distances between adjacent heterocycles can be used as an indication of whether or not a bond is formed. The corresponding distance (red dots in Figure 7.4a and d) of (0.42±0.03) nm is in excellent agreement to the distance expected for such a covalent bond. DFT calculations of the covalently bonded dimer structure without substrate yield the same distance of 0.42 nm. Both dimer structures indicate that only one covalent bond

per dimer has been formed. In Di1 a bond has formed between two pyrazine moieties, namely a C2-to-C2-bond, according to the numbering introduced in Figure 7.1. Di2, in contrast, involves a bond between a pyrazine and a pyridine moiety, a C2-to-C6-bond. We counted 101 dimers of type Di1 and 20 dimers of Di2 in our study, indicating the preference for pyrazine-bonded structures. Another characteristic difference between the two dimer structures is the alignment of the two **pap** constituents as indicated in Figure 7.4. Whereas the alignment in Di2 is consistent with just a covalent bond formation, the alignment observed in Di1 suggests that the different angle is due to a stabilization of the dimer via metal coordination bonding, as shown in Figure 7.4c. To corroborate this interpretation, we also performed DFT calculations of these structures, again excluding the substrate. The DFT calculations reproduce the observed alignment angles (see Figure 7.4a and d) only if one includes or excludes a coordinating gold atom for Di1 and Di2, respectively. In particular, the slightly larger distance between the adjacent heterocycles that are not covalently bonded to each other (green dots in Di1) of (0.50±0.03) nm is in qualitative agreement with the corresponding simulated structure (see Figure 7.4c). In contrast, if there is no metal coordination involved, the corresponding distance measures (0.72±0.04) nm (yellow dots). We hence interpret this distance variation as being indicative of a metal coordination bond being present [300–305]. At first glance it is surprising that the gold atom is not directly visible in the AFM images — a circumstance that will be elucidated further below, after the analysis of tetramer Te1, shown in Figure 7.4f-j. On the surface it has C_{2v} symmetry (D_{2h} in the gas-phase) indicating that the bonds between the constituents are not all of the same nature. Following the reasoning from the dimer structure as outlined above, one immediately recognizes that Te1 consists of two dimers connected to each other *via* metal coordination bonds. This hypothesis is supported by DFT calculations carried out for the tetramer Te1 without substrate. Alternate models e.g. assuming four covalent bonds do not reproduce the experimentally observed structure.

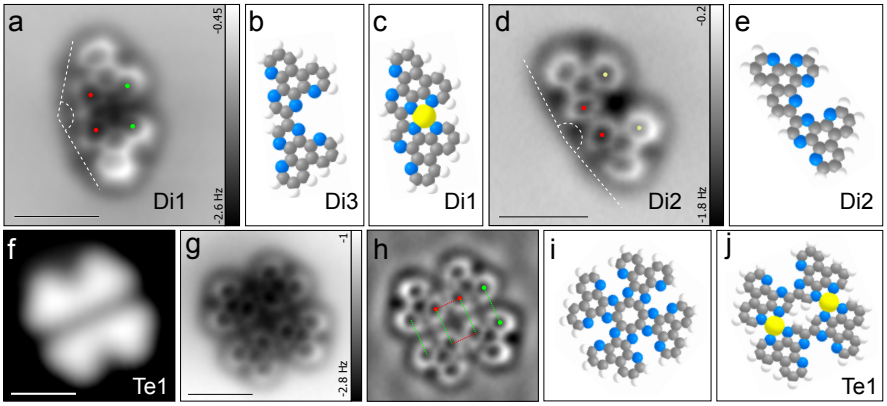

Figure 7.4: Detailed analysis of some of the observed molecular structures. (a and d) AFM images of a Di1- and a Di2-dimer, respectively. The distances between adjacent heterocycles (red and green dots) indicates that only one covalent bond was formed between each two **pap** constituents. The corresponding distance (red dots) of about 0.42 nm is in very good agreement to the distance expected for such a covalent bond. The main difference between the two dimer structures lies in the bond that has formed upon annealing (C2-to-C2 vs. C2-to-C6). Another characteristic difference between the two dimer structures is the angle of alignment of the two **pap** constituents as indicated by the dashed lines in the images. Whereas the alignment in Di2 is consistent with just a covalent bond formation, the alignment observed in Di1 can only be rationalized if a stabilization of the dimer via metal coordination bonds is assumed, as shown in (c). Hence, the slightly shorter distance between adjacent heterocycles (green dots) of about 0.56 nm compared to the one of about 0.72 nm (yellow dots) we interpret as being indicative of a metal coordination bond being present. The appearance of the molecular structure allows one to identify the nitrogen atoms (see above) as shown in the corresponding models (b, c, and e). (f-j) STM (f), AFM (g), high-pass filtered AFM (h) image and structural models (i, j) of the Te1 tetramer. Based on the dimer analysis one readily observes distinctly different distances between adjacent heterocycles in Te1, indicating that Te1 consists of two dimer structures that are interconnected by metal coordination bonds to form the tetramer as illustrated in (j). Other possible structures as the one in (i) do not reproduce the distances and alignment angles of Te1. Imaging parameters: (a,d) $\Delta z = 1.33\,\text{Å}$ from $V = 0.05\,\text{V}$, $I = 1\,\text{pA}$. (g) $\Delta z = 1.9\,\text{Å}$ from $V = 0.2\,\text{V}$, $I = 1\,\text{pA}$. (f) STM image $V = 0.2\,\text{V}$, $I = 1\,\text{pA}$. Scale bars: 1 nm.

7.5 Simulation of AFM images

We performed total-energy DFT calculations of four selected dimer structures including the substrate. Next we calculated AFM images of the corresponding optimized structures (see upper panel of Figure 7.5). Note that the image simulations take into account the bending of the CO molecule at the tip apex [296, 306], while the parameters required to simulate a CO tip were selected upon previous image simulations and their direct comparison to experimental data in other works [307]. To understand the possible participation of gold adatoms in metal-organic coordination bonding in our structures, we calculated not only Di1 and Di2, but two more dimers: The counterpart of Di1, but without a gold atom, henceforth labeled Di3, and the counterpart of Di2, but with an additional gold adatom, henceforth labeled Di4. Hence, these structures are pyrazine-pyrazine (C2-to-C2-bond, Di1 and Di3) and pyrazine-pyridine-bonded (C2-to-C6-bond, Di4 and Di2) dimers, each with and without a gold adatom coordinated to nitrogens. The relaxed geometries are shown in Figure 7.5, alongside with simulated AFM images. First we turn to the discussion of C8-C9 versus N4-N5 and N1-N12 distances, relevant for the assignment of nitrogen positions in each molecule. The DFT calculation yields C8-C9-distances of 2.98–3.00 Å being distinctly larger than the N4-N5 and N1-N12 distances that measure only 2.69–2.78 Å. In the AFM imaging with a CO-terminated tip, this difference seems to be even exaggerated by distortions, such that in the simulated images it can be clearly discerned (see white and blue arrowheads) in agreement with the experiment. This puts the assignment of nitrogen positions inside the molecules from AFM images onto solid grounds.

The simulated images also confirm that it is possible to have a coordinating gold atom present in the structure without directly resolving it with the AFM as a repulsive feature. The reason for the absence of a repulsive feature from the gold adatom is related to i) presence of charge transfer between the gold adatom and the molecule giving rise

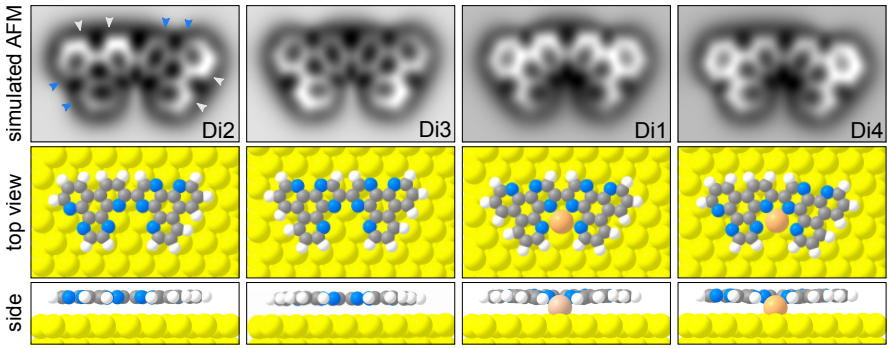

Figure 7.5: DFT-calculated structures and simulated AFM images. Pyrazine-pyrazine (C2-to-C2-bond, D1 and Di3) and pyrazine-pyridine (C2-to-C6-bond, Di2 and Di4) dimers, each with (Di1, Di4) and without (Di2, Di3) a gold adatom coordinated to nitrogens are shown in the calculated geometries. The corresponding simulated AFM images are shown above. The difference in the C8-C9 versus N4-N5 or N1-N12 distances (white and blue arrowheads, respectively) confirm the experimental assignment.

to an additional attractive interaction with CO-tip and to ii) the vertical position of the gold adatom and the surrounding nitrogen atoms being considerably closer to the surface than the one of the organic framework, diminishing the onset of Pauli repulsion. Consequently, the gold atom leads to a dark circular halo of long-range attractive interaction. Indeed such a dark halo can also be seen in the experimental AFM image of Di1, for which we expect a gold adatom to be present, lending further support for the presence of a gold adatom.

What more, both dimer structures without gold adatom show a straight 180° alignment angle consistent with our interpretation of Di2. However, the angle of Di1 is about 170°, but not as small as the experimentally observed one. We also note that the experimental image of Di1 has a bright protrusion at the bond that formed upon annealing, which is not reproduced by the calculated AFM image, leaving some room for the interpretation of the atomistic details in Di1, in particu-

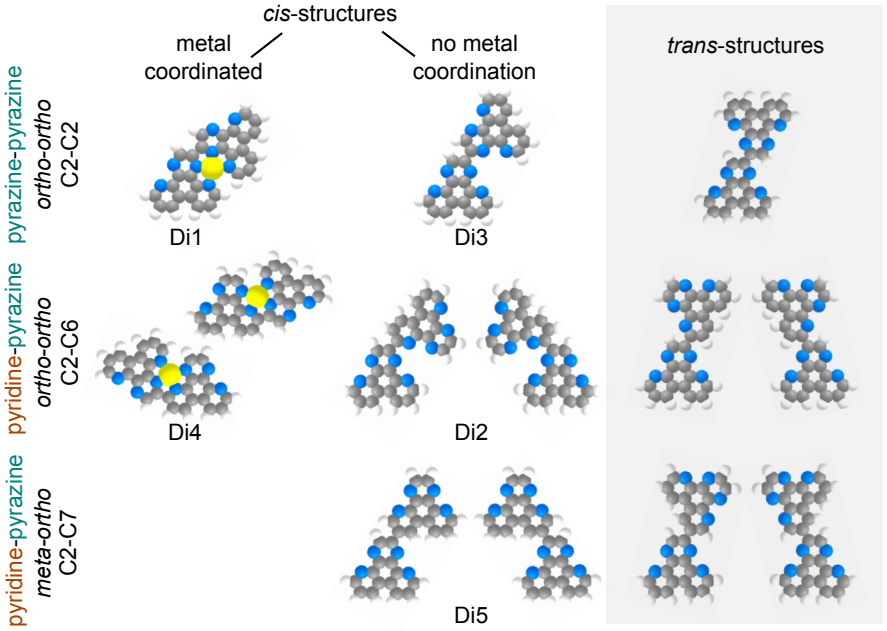

Figure 7.6: Possible structures of dimer formation. A covalent bond is formed either between *ortho*-carbon atoms of two pyrazine moieties (top row) or between a pyridine and a pyrazine moiety (center row) of the neighboring **pap** molecules. For the pyridine moiety also *meta*- and *para*-carbon atoms exist, which could react to form additional dimer structures exemplified for the *meta*-carbon (bottom row). For the pyridine-bonded structures, there are two enantiomers in each case. The bond configuration can be divided into *cis*-N^N and *trans*-N^N structures. Only the purely *ortho*-carbon bonded *cis*-N^N-structures facilitate metal coordination (Di1 and Di4).

lar as it regards the exact position and bonding of an additional gold atom. We therefore conclude that the exact bonding geometry in Di1 is not fully captured by our DFT calculation. This can be ascribed to a deficiency in the description of metal-organic complexes by the DFT method.

In addition, we enforced alignment angles smaller than 180° for both, Di1 and Di3. We observed a considerable increase of the total-energy for both structures of few eV for angles smaller than 150°. We therefore exclude that the relatively weak interaction with a flat Au(111) surface without adatoms being present can enforce such a geometry. Our DFT calculations of molecules without a gold adatom revealed only weak, mostly van-der-Waals interaction with the Au(111) substrate underneath. Consequently, the molecules Di2 and Di3 adopt an almost planar configuration with the plane of the molecule located approximately 3.3 Å above the Au(111). The absence of a strong chemical bond between the molecule and the substrate exclude strong conformational changes of the molecules caused by the substrate.

Taking all the above observations into consideration, it is clear that the structural information from AFM images is decisive for the identification of all bonding configurations. However, after establishing the direct relationship between the geometric structure deduced from AFM and the appearances in STM images, one can identify the different type of structures also from the STM images alone. We note that this relationship between structure and appearance in STM images was established and confirmed on the basis of atomically-resolved AFM images of in total 26 clusters. We therefore included also all highly-resolved STM images in the statistical analysis discussed in the remainder of this work.

7.6 Hierarchy of dimer structures

A covalent bond either between the two pyrazine moieties (Di1) or between a pyrazine and a pyridine moiety (Di2) of each two neighboring molecules was identified. Another difference between Di1 and Di2 lies in the metal coordination. However, irrespective of a possible metal coordination many more possibilities for a bond formation could be

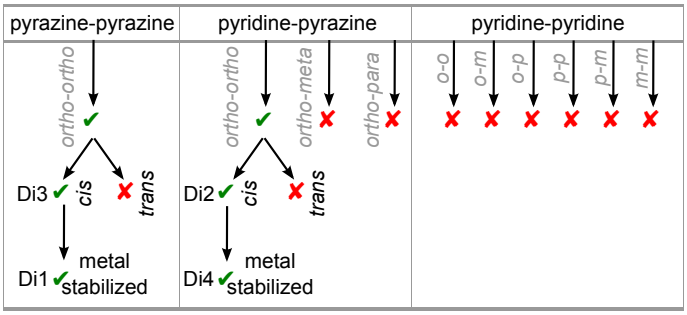

Figure 7.7: Hierarchy of dimer structures. Dimer structures can be classified according to the bonding moiety (top row), to their bonding positions (second row), relative orientation (third row), and additional metal coordination (bottom row). Structures observed in the experiments are checked, all others crossed, highlighting the strong selectivity of on-surface bond formation. The possibility of metal coordination seems to directly coincide with the respective structure being observed.

expected, even if regioselectivity is taking place. In this spirit, it is interesting to analyze, which dimer structures could possibly form and to compare that with the actual observations. Before doing so, we note that we never observed any structures involving covalent bonds between two pyridine moieties. We therefore largely exclude this possibility from the following discussion.

Figure 7.6 shows a set of dimer structures that could be envisioned. A covalent bond between pyridine and pyrazine yields a dimer of lower symmetry than in the other case, which therefore may occur in two different enantiomers on the surface. Indeed we observe each two enantiomers in equal amounts within statistical significance. We disregard stereochemistry in the remainder of this work. Moreover, the covalent bond formation could result in either a *cis*-N^N or a *trans*- N^N configuration of the two **pap** constituents as exemplified in Figure 7.8. Considering the possible stabilization of the *trans*-configuration by intra-molecular hydrogen bonds it is most surprising that we never

observed any structures in *trans*-configuration of the molecules. This finding can be accounted for the fact that a *trans*-configuration could not be stabilized by a metal coordination bond. The same holds true for structures in which *meta*- and *para*-carbon atoms of a pyridine moiety are involved in the dimer formation: these would not facilitate metal coordination and we did not observe them. These two findings point towards an important role of metal coordination in the covalent bond formation. Figure 7.7 summarizes the possible dimer structures and their occurrences in the experiment. Although Di3 and Di4 were not observed at all as single entities in our study, reconsidering the tetramer Te1, one realizes that Te1 consists of two such Di3 dimers, which are linked via metal coordination bonds. Similarly, Di3 and Di4 dimers were observed as building blocks of larger clusters Tr2 and Te2, respectively (Figure 7.8). Interestingly, the highly symmetric Tr1 was formed based on a strict regioselectivity of the pyrazine groups of three neighboring **pap** molecules for dehydrogenation leading to the formation of a hexaazatriphenyl core. It constitutes due to its three-fold symmetry and its N^N chelating property an established building block for a variety of applications [285, 288]. Alternatively, Tr1 can be described as a three-star version of dipyrido[2,3-*a*:3′,2′-*c*]phenazine, a bridging ligand applied in coordination chemistry [308].

Figure 7.8 shows an overview of the most probable structures that were observed and also are the basis for the statistical analysis for regioselectivity. In total we observed 203 bonds that have been formed. Among them, 160 bonds occurred between two pyrazine moieties of each two neighboring molecules, 43 between a pyrazine and a pyridine group, and none between two pyridine groups[1], demonstrating a very strong but not a extremely strict regioselectivity. Note that the latter statistics of the observation of different bond types is performed irrespective of whether Au adatoms are involved or not. As each **pap**

[1]There are a few observation of bonds, which could not be unambiguously identified. We therefore provide an upper limit of at most 2% of pyridine-pyridine bonded structures

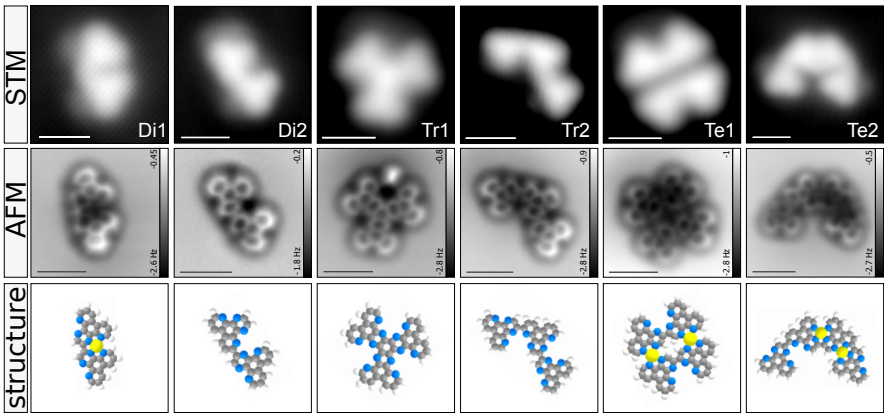

Figure 7.8: Analysis of main structures observed after covalent bond formation. STM images (top row), AFM images (middle row), and structures (bottom row) for products of dehydrogenation. The structural assignment follows the considerations discussed above.

molecule consists of two pyridine but only one pyrazine moiety, in absence of any regioselectivity one would expect a ratio of occurrences of 1 : 4 : 4 of bond-types pyrazine-pyrazine : pyrazine-pyridine : pyridine-pyridine — quite opposite to what is observed. When being interpreted in terms of thermodynamic equilibrium at 200 °C and the Boltzmann statistics, the observed occurrences would yield an energy difference of $\Delta E \simeq 2.6$ kcal/mol of pyrazine-pyrazine versus pyrazine-pyridine bonding geometry.

We would like to mention, that some of the images show apparent bonds between neighboring nitrogen atoms. However, such features have been observed before and were identified as imaging artifacts [306, 309, 310]. In this context it is important to note that the structural information deduced from the AFM images allows to unambiguously identify which moieties can be involved in the bonds from the molecules' orientations and the distances between heterocycles as presented above irrespective of where exactly real or apparent bonds

are observed.

7.7 A possible mechanism for selective bond formation

Although a thorough analysis of the mechanism behind our observations goes beyond the scope of this work, we now turn to a brief discussion of a *possible* mechanism behind one aspect of selective bond formation. As mentioned in the context of Figures 7.7 and 7.8 , only *cis*-N^N-structures bonded in *ortho-ortho* geometry enable the incorporation of a gold atom, whereas *meta-ortho*-bonded *cis*-N^N-structures as well as all *trans*-N^N-structures do not. Hence, apparently exactly those structures are experimentally observed, which could potentially be stabilized by a coordinating gold atom. Such a gold atom may modify the reactivity of its direct neighborhood, facilitating dehydrogenation. More likely it appears to us, however, that it is rather the geometry that is important: a gold adatom between two monomers, will stabilize two hydrogens each belonging to a different monomer in close proximity, in which a concerted dehydrogenation and immediate bond formation may be facilitated. At the elevated temperature, the entire surface will be subject to constant change and rearrangement, but the presence of coordinating gold adatoms may favor certain geometries over others. When considering such a scenario, the importance of the molecular degrees of freedom being reduced to two dimensions in on-surface chemistry becomes apparent. Note that the regioselectivity concerning the preference for pyrazine-bonded structures observed for the ratio of occurences of different dimers cannot be accounted for by the above considerations alone. Hence, this is a separate aspect of our observations and must stem from a different reactivity of different sites. Thorough theoretical studies on the mechanism and the exact role of Au in these aryl-aryl couplings are ongoing in our laboratory.

7.8 Conclusion

In summary, we have demonstrated that pyrazino[2,3-*f*][4,7]phenanthroline (**pap**) can bond-selectively be transformed through aryl-aryl coupling on an Au(111) surface in UHV conditions into a variety of heterocyclic compounds. The observed regioselectivity of the reactions originates from the fact, that *ortho*-hydrogen atoms of the pyrazine rings are preferentially activated for a dehydrogenative C-C bond formation over their pyridine equivalents. Most importantly, the combined STM/AFM study allows a full atomistic analysis of the different reaction products while unambiguously discriminating pyrazine from pyridine moieties. This synthetic strategy to utilize tailored polycyclic precursor molecules comprising pyrazine units will open an avenue for the construction of novel heterocyclic molecules. Depending on the number of pyrazine units incorporated into the starting molecule, the realization of more extended heteroaromatic structures with atomically precise nitrogen locations can be expected.

7.9 Contributors to this work

This project was a collaboration between UR and the University of Bern. **pap** molecules were synthesized by Songjie Chen. All experiments were performed together with Xunshan Liu during his secondment. Ondřej Krejčí and Pavel Jelínek from the Nanosurf Lab in Prague performed DFT calculations on the adsorption geometry and simulated the AFM images.

8 Summary

In this thesis a broad range of experiments that deal with fundamental properties of single molecule charging processes and thermally activated on-surface reactions is presented.

The first two chapters provide an overview of the principles and techniques used throughout this thesis.

In **chapter 3** it is discussed that a reduction of the single-particle level spacing of two frontier orbitals enables the manifestation of strong electron-correlation effects in single molecules. The single-particle level spacing engineered by dicyanovinyl-substitution leads to an apparent reversal of orbital sequence and a strongly-entangled ground state. In this regime conduction exhibits a spatial signature fundamentally different from what a single particle picture would predict.

The results presented in **chapter 4** demonstrate how single molecules at the edges of self-assembled molecular islands grown on silver can temporarily change their charge state due to the presence of the electric field from a scanning-probe tip. Close to the threshold voltage for a charge state transition, periodic switching of the charge is directly driven by the cantilever motion in frequency-modulated AFM, as can be deduced from the signature in the measured frequency shift. The amplitude dependence indicates a smooth rather than a sudden charge state transition, while the absence of any appreciable signal in the dissipation channel points towards a non-hysteretic process. Temperature-dependent experiments show that the thermal broadening in the substrate is responsible for the smooth charge transition.

In this regime, the integrated frequency shift yields the tip-sample force that is due to a single additional electron. Further, the signature of the dynamic charging response provides information on the electronic coupling of the molecule to the substrate. Suitable subtraction of images reveals that the extra electron is delocalized over the entire molecule and that the main contribution to the difference image stems from electrostatic interaction. Finally, we investigated the distance dependence of the threshold voltage required for charing.

A novel concept for the realization of molecular quantum cellular automata is demonstrated in **chapter 5**, namely the simultaneous correct alignment and exact spacing of neighboring cells in combination with the programmability by controlled formation of complex and non-repetitive patterns of cells. The solution lies in the combination of the creation of perfectly aligned inactive cells by self-assembly as a first and their selective and controlled activation as a second step. Whereas the activation took place by vacancy formation, in the future, other mechanisms as e.g. the selective removal of ligands can be envisioned. We demonstrate that automata consisting of only few cells already show rich switching behavior.

In **chapter 6** a molecular switch based on the motion of a single molecule bonded to the topmost layer of bilayer insulating films on a copper surface is presented. The inclined molecule switches back and forth between the two equivalent conformations. The bistability is enabled by a bond formation and rupture between the admolecule and cations in the insulating layer, with switching direction controlled by positioning the tip slightly off-center above the molecule and initiated by applying voltage pulses of according polarity. Submolecular AFM imaging with functionalized tips provides information of the geometry, namely the tilt and adsorption position in both of the switching states.

In **chapter 7** it is demonstrated that pyrazino[2,3-*f*][4,7]phenanthroline molecule can bond-selectively be transformed through aryl-aryl cou-

pling on a gold surface into a variety of heterocyclic compounds. The observed regioselectivity of the reactions originates from the fact, that ortho-hydrogen atoms of the pyrazine rings are preferentially activated for a dehydrogenative C-C bond formation over their pyridine equivalents. The combined STM/AFM study allows a full atomistic analysis of the different reaction products while unambiguously discriminating pyrazine from pyridine moieties. This synthetic strategy to utilize tailored polycyclic precursor molecules comprising pyrazine units will open an avenue for the construction of novel heterocyclic molecules. Depending on the number of pyrazine units incorporated into the starting molecule, the realization of more extended heteroaromatic structures with atomically precise nitrogen locations can be expected.

Bibliography

[1] G. Binnig et al. 'Tunneling through a controllable vacuum gap'. In: *Appl. Phys. Lett.* 40 (1982), 178.

[2] G. Binnig et al. 'Surface Studies by Scanning Tunneling Microscopy'. In: *Phys. Rev. Lett.* 49 (1982), 57.

[3] G. Binnig and H. Rohrer. 'Scanning tunneling microscopy-from birth to adolescence'. In: *Rev. Mod. Phys.* 59 (1987), 615.

[4] G. Binnig et al. '7×7 Reconstruction on Si(111) Resolved in Real Space'. In: *Phys. Rev. Lett.* 50 (1983), 120.

[5] G. Binnig, C. F. Quate, and C. Gerber. 'Atomic Force Microscope'. In: *Phys. Rev. Lett.* 56 (1986), 930.

[6] G. Binnig et al. 'Atomic resolution with atomic force microscope'. In: *EPL* 3 (1987), 1281.

[7] T. R. Albrecht and C. F. Quate. 'Atomic resolution imaging of a nonconductor by atomic force microscopy'. In: *J. Appl. Phys.* 62 (1987), 2599.

[8] F. J. Giessibl. 'Atomic resolution on Si(111)-(7×7) by noncontact atomic force microscopy with a force sensor based on a quartz tuning fork'. In: *Appl. Phys. Lett.* 76 (2000), 1470.

[9] C. J. Chen. *Introduction to scanning tunneling microscopy*. Vol. 4. Oxford University Press on Demand, 1993.

[10] J. A. Stroscio and W. J. Kaiser. *Scanning tunneling microscopy*. Vol. 27. Academic Press, 1993.

[11] G. Gamow. 'Zur quantentheorie des atomkernes'. In: *Z. Phys.* 51 (1928), 204.

[12] F. Schwabl. *Quantenmechanik*. Vol. 3. Springer, Berlin, 1998.

[13] J. Bardeen. 'Tunnelling from a Many-Particle Point of View'. In: *Phys. Rev. Lett.* 6 (1961), 57.

[14] I. Giaever. 'Electron Tunneling Between Two Superconductors'. In: *Phys. Rev. Lett.* 5 (1960), 464.

[15] J. Nicol, S. Shapiro, and P. H. Smith. 'Direct Measurement of the Superconducting Energy Gap'. In: *Phys. Rev. Lett.* 5 (1960), 461.

[16] J. Tersoff and D. R. Hamann. 'Theory and Application for the Scanning Tunneling Microscope'. In: *Phys. Rev. Lett.* 50 (1983), 1998.

[17] J. Tersoff and D. R. Hamann. 'Theory of the scanning tunneling microscope'. In: *Phys. Rev. B* 31 (1985), 805.

[18] `https://www.physics.purdue.edu/nanophys/newpage10-03/techniques/stm.htm`.

[19] H. Grabert and M. H. Devoret. 'Single Charge Tunneling: Coulomb Blockade Phenomena in Nanostructures'. In: *Physics (Plenum Press, New York)* (1992).

[20] L. Jacak, P. Hawrylak, and A. Wójs. *Quantum dots*. Springer Science & Business Media, 2013.

[21] F. J. Giessibl. 'Advances in atomic force microscopy'. In: *Rev. Mod. Phys.* 75 (2003), 949.

[22] F. J. Giessibl. 'Forces and frequency shifts in atomic-resolution dynamic-force microscopy'. In: *Phys. Rev. B* 56 (1997), 16010.

[23] J. E. Sader and S. P. Jarvis. 'Accurate formulas for interaction force and energy in frequency modulation force spectroscopy'. In: *Appl. Phys. Lett.* 84 (2004), 1801.

[24] H. C. Hamaker. 'The London-van der Waals attraction between spherical particles'. In: *Physica* 4 (1937), 1058.

[25] J. E. Jones. 'On the determination of molecular fields. II. From the equation of state of a gas'. In: *Proceedings of the Royal Society of London A: Mathematical, Physical and Engineering Sciences*. Vol. 106. The Royal Society. 1924, 463.

[26] P. Samorì. 'Scanning probe microscopies beyond imaging'. In: *J. Mater. Chem.* 14 (2004), 1353.

[27] L. Kelvin. 'V. Contact electricity of metals'. In: *The London, Edinburgh, and Dublin Philosophical Magazine and Journal of Science* 46 (1898), 82.

[28] J. M. R. Weaver and D. W. Abraham. 'High resolution atomic force microscopy potentiometry'. In: *J. Vac. Sci. Technol., B* 9 (1991), 1559.

[29] M. Nonnenmacher, M. P. o'Boyle, and H. K. Wickramasinghe. 'Kelvin probe force microscopy'. In: *Appl. Phys. Lett.* 58 (1991), 2921.

[30] H.-C. Ploigt et al. 'Local work function changes determined by field emission resonances: NaCl/Ag(100)'. In: *Phys. Rev. B* 76 (2007), 195404.

[31] F. J. Giessibl. 'Theory for an electrostatic imaging mechanism allowing atomic resolution of ionic crystals by atomic force microscopy'. In: *Phys. Rev. B* 45 (1992), 13815.

[32] R. Błaszczyszyn, M. Błaszczyszyn, and R. Męclewski. 'Work function of the adsorption system of potassium on tungsten'. In: *Surf. Sci.* 51 (1975), 396.

[33] K. Besocke, B. Krahl-Urban, and H. Wagner. 'Dipole moments associated with edge atoms; A comparative study on stepped Pt, Au and W surfaces'. In: *Surf. Sci.* 68 (1977), 39.

[34] T. V. W. Janssens et al. ‘Surface potential around potassium promoter atoms on Rh(111) measured with photoemission of adsorbed Xe, Kr, and Ar’. In: *Phys. Rev. B* 49 (1994), 14599.

[35] R. Bennewitz et al. ‘Aspects of dynamic force microscopy on NaCl/Cu(111): resolution, tip-sample interactions and cantilever oscillation characteristics’. In: *Surf. Interface Anal.* 27 (1999), 462.

[36] W. Steurer et al. ‘Probe-based measurement of lateral single-electron transfer between individual molecules’. In: *Nat. Commun.* 6 (2015), 8353.

[37] W. Steurer et al. ‘Manipulation of the Charge State of Single Au Atoms on Insulating Multilayer Films’. In: *Phys. Rev. Lett.* 114 (2015), 036801.

[38] F. Albrecht et al. ‘Probing Charges on the Atomic Scale by Means of Atomic Force Microscopy’. In: *Phys. Rev. Lett.* 115 (2015), 076101.

[39] F. Krok et al. ‘Lateral resolution and potential sensitivity in Kelvin probe force microscopy: Towards understanding of the sub-nanometer resolution’. In: *Phys. Rev. B* 77 (2008), 235427.

[40] A. J. Weymouth et al. ‘Phantom Force Induced by Tunneling Current: A Characterization on Si(111)’. In: *Phys. Rev. Lett.* 106 (2011), 226801.

[41] G. Meyer. ‘A simple low-temperature ultrahigh-vacuum scanning tunneling microscope capable of atomic manipulation’. In: *Rev. Sci. Instrum.* 67 (1996), 2960.

[42] S. Zöphel. ‘Der aufbau eines tieftemperatur-rastertunnelmikroskops und strukturuntersuchungen auf vicinalen kupferoberflächen’. PhD thesis. Freie Universität Berlin, 2000.

[43] M. Neu. ‘Rasterkraftmikroskopie auf atomarer Skala: Van-der-Waals Wechselwirkung in molekularen Systemen’. PhD thesis. Universität Regensburg, 2014.

[44] G. Münnich. 'Cross-sectional scanning probe microscopy on GaAs: Tip-induced band bending, buried acceptors and adsorbed molecules'. PhD thesis. Universität Regensburg, 2014.

[45] K. Besocke. 'An easily operable scanning tunneling microscope'. In: *Surf. Sci.* 181 (1987), 145.

[46] J. Frohn et al. 'Coarse tip distance adjustment and positioner for a scanning tunneling microscope'. In: *Rev. Sci. Instrum.* 60 (1989), 1200.

[47] J. Lobo and A. Mascaraque. 'Observation of the noble-metal L-gap surface state in Cu(311)'. In: *J. Phys. Condens. Matter* 18 (2006), L395.

[48] H. Hövel, B. Grimm, and B. Reihl. 'Modification of the Shockley-type surface state on Ag(111) by an adsorbed xenon layer'. In: *Surf. Sci.* 477 (2001), 43.

[49] T. Andreev, I. Barke, and H. Hövel. 'Adsorbed rare-gas layers on Au(111): Shift of the Shockley surface state studied with ultraviolet photoelectron spectroscopy and scanning tunneling spectroscopy'. In: *Phys. Rev. B* 70 (2004), 205426.

[50] K. Seufert et al. 'Controlled Interaction of Surface Quantum-Well Electronic States'. In: *Nano Lett.* 13 (2013), 6130.

[51] K. Morgenstern, K.-F. Braun, and K.-H. Rieder. 'Surface-State Depopulation on Small Ag(111) Terraces'. In: *Phys. Rev. Lett.* 89 (2002), 226801.

[52] F. Hanke and J. Björk. 'Structure and local reactivity of the Au(111) surface reconstruction'. In: *Phys. Rev. B* 87 (2013), 235422.

[53] J. Libuda et al. 'Structure and defects of an ordered alumina film on NiAl(110)'. In: *Surf. Sci.* 318 (1994), 61.

[54] Y.-S. Fu et al. 'Ultrathin lead oxide film on Pb(111) and its application in single spin detection'. In: *Appl. Phys. Lett.* 95 (2009), 063107.

[55] S. Schintke et al. 'Insulator at the Ultrathin Limit: MgO on Ag(001)'. In: *Phys. Rev. Lett.* 87 (2001), 276801.

[56] S. Valeri et al. 'Scanning tunnelling microscopy of MgO ultrathin films on Ag(001)'. In: *Phys. Rev. B* 65 (2002), 245410.

[57] M. Sterrer et al. 'Control of the Charge State of Metal Atoms on Thin MgO Films'. In: *Phys. Rev. Lett.* 98 (2007), 096107.

[58] C. F. Hirjibehedin, C. P. Lutz, and A. J. Heinrich. 'Spin Coupling in Engineered Atomic Structures'. In: *Science* 312 (2006), 1021.

[59] C. F. Hirjibehedin et al. 'Large Magnetic Anisotropy of a Single Atomic Spin Embedded in a Surface Molecular Network'. In: *Science* 317 (2007), 1199.

[60] T. Miyamachi et al. 'Robust spin crossover and memristance across a single molecule'. In: *Nat. Commun.* 3 (2012), 938.

[61] A. F. Otte et al. 'Spin Excitations of a Kondo-Screened Atom Coupled to a Second Magnetic Atom'. In: *Phys. Rev. Lett.* 103 (2009), 107203.

[62] B. Warner et al. 'Tunable magnetoresistance in an asymmetrically coupled single-molecule junction'. In: *Nat. Nanotechnol.* 10 (2015), 259.

[63] C. D. Ruggiero, T. Choi, and J. A. Gupta. 'Tunneling spectroscopy of ultrathin insulating films: CuN on Cu(100)'. In: *Appl. Phys. Lett.* 91 (2007), 253106.

[64] R. Bennewitz et al. 'Ultrathin films of NaCl on Cu(111): a LEED and dynamic force microscopy study'. In: *Surf. Sci.* 438 (1999), 289.

[65] W. Hebenstreit et al. 'Atomic resolution by STM on ultra-thin films of alkali halides: experiment and local density calculations'. In: *Surf. Sci.* 424 (1999), L321.

[66] S. Fölsch et al. 'Self-Organized Patterning of an Insulator-on-Metal System by Surface Faceting and Selective Growth: NaCl/Cu(211)'. In: *Phys. Rev. Lett.* 84 (2000), 123.

[67] J. Repp et al. 'Ionic Films on Vicinal Metal Surfaces: Enhanced Binding due to Charge Modulation'. In: *Phys. Rev. Lett.* 86 (2001), 252.

[68] S. Fölsch, U. Barjenbruch, and M. Henzler. 'Atomically thin epitaxial films of NaCl on germanium'. In: *Thin Solid Films* 172 (1989), 123.

[69] L. Gross et al. 'Contacting self-ordered molecular wires by nanostencil lithography'. In: *J. Vac. Sci. Technol., B* 28 (2010), C4D34.

[70] Z.-C. Dong et al. 'Vibrationally Resolved Fluorescence from Organic Molecules near Metal Surfaces in a Scanning Tunneling Microscope'. In: *Phys. Rev. Lett.* 92 (2004), 086801.

[71] N. Pavliček et al. 'Symmetry Dependence of Vibration-Assisted Tunneling'. In: *Phys. Rev. Lett.* 110 (2013), 136101.

[72] Y.-S. Fu et al. 'Identifying Charge States of Molecules with Spin-Flip Spectroscopy'. In: *Phys. Rev. Lett.* 103 (2009), 257202.

[73] N. Ohta et al. 'Enhancement of Inelastic Electron Tunneling Conductance Caused by Electronic Decoupling in Iron Phthalocyanine Bilayer on Ag(111)'. In: *J. Phys. Chem. C* 117 (2013), 21832.

[74] Z. Dong et al. 'Generation of molecular hot electroluminescence by resonant nanocavity plasmons'. In: *Nat. Photon.* 4 (2010), 50.

[75] J. Repp. 'Rastertunnelmikroskopie und-spektroskopie an Adsorbaten auf Metall-und Isolatoroberflächen'. PhD thesis. Freie Universität Berlin, 2002.

[76] J. Repp et al. 'Charge-State-Dependent Diffusion of Individual Gold Adatoms on Ionic Thin NaCl Films'. In: *Phys. Rev. Lett.* 117 (2016), 146102.

[77] R. Smoluchowski. 'Anisotropy of the Electronic Work Function of Metals'. In: *Phys. Rev.* 60 (1941), 661.

[78] J. Repp et al. 'Scanning Tunneling Spectroscopy of Cl Vacancies in NaCl Films: Strong Electron-Phonon Coupling in Double-Barrier Tunneling Junctions'. In: *Phys. Rev. Lett.* 95 (2005), 225503.

[79] M. F. Green et al. 'Patterning a hydrogen-bonded molecular monolayer with a hand-controlled scanning probe microscope'. In: *Beilstein J. Nanotechnol.* 5 (2014), 1926.

[80] F. E. Kalff et al. 'A kilobyte rewritable atomic memory'. In: *Nat. Nanotechnol* 11 (2016), 926.

[81] L. Bartels, G. Meyer, and K.-H. Rieder. 'Controlled vertical manipulation of single CO molecules with the scanning tunneling microscope: A route to chemical contrast'. In: *Appl. Phys. Lett.* 71 (1997), 213.

[82] L. Gross et al. 'The Chemical Structure of a Molecule Resolved by Atomic Force Microscopy'. In: *Science* 325 (2009), 1110.

[83] L. Gross et al. 'Atomic Resolution on Molecules with Functionalized Tips'. In: *Noncontact Atomic Force Microscopy*. Springer, 2015, 223.

[84] L. Gross et al. 'High-Resolution Molecular Orbital Imaging Using a p-Wave STM Tip'. In: *Phys. Rev. Lett.* 107 (2011), 086101.

[85] D. M. Cardamone, C. A. Stafford, and S. Mazumdar. 'Controlling Quantum Transport through a Single Molecule'. In: *Nano Lett.* 6 (2006), 2422.

[86] G. Begemann et al. 'All-Electric Spin Control in Interference Single Electron Transistors'. In: *Nano Lett.* 9 (2009), 2897.

[87] A. Donarini, G. Begemann, and M. Grifoni. 'Interference effects in the Coulomb blockade regime: Current blocking and spin preparation in symmetric nanojunctions'. In: *Phys. Rev. B* 82 (2010), 125451.

[88] C. M. Guédon et al. 'Observation of quantum interference in molecular charge transport'. In: *Nat. Nanotechnol.* 7 (2012), 305.

[89] H. Vazquez et al. 'Probing the conductance superposition law in single-molecule circuits with parallel paths'. In: *Nat. Nanotechnol.* 7 (2012), 663.

[90] S. Ballmann et al. 'Experimental Evidence for Quantum Interference and Vibrationally Induced Decoherence in Single-Molecule Junctions'. In: *Phys. Rev. Lett.* 109 (2012), 056801.

[91] J. Xia et al. 'Breakdown of Interference Rules in Azulene, a Non-Alternant Hydrocarbon'. In: *Nano Lett.* 14 (2014), 2941.

[92] A. Zhao et al. 'Controlling the Kondo Effect of an Adsorbed Magnetic Ion Through Its Chemical Bonding'. In: *Science* 309 (2005), 1542.

[93] G. Maruccio et al. 'Correlation Effects in Wave Function Mapping of Molecular Beam Epitaxy Grown Quantum Dots'. In: *Nano Lett.* 7 (2007), 2701.

[94] I. Fernández-Torrente, K. J. Franke, and J. I. Pascual. 'Vibrational Kondo Effect in Pure Organic Charge-Transfer Assemblies'. In: *Phys. Rev. Lett.* 101 (2008), 217203.

[95] K. J. Franke, G. Schulze, and J. I. Pascual. 'Competition of Superconducting Phenomena and Kondo Screening at the Nanoscale'. In: *Science* 332 (2011), 940.

[96] A. Chiesa et al. 'Many-Body Models for Molecular Nanomagnets'. In: *Phys. Rev. Lett.* 110 (2013), 157204.

[97] S. Grothe et al. 'Quantifying Many-Body Effects by High-Resolution Fourier Transform Scanning Tunneling Spectroscopy'. In: *Phys. Rev. Lett.* 111 (2013), 246804.

[98] M. M. Ervasti et al. 'Single-and many-particle description of scanning tunneling spectroscopy'. In: *J. Electron. Spectrosc. Relat. Phenom.* (2016).

[99] G. Begemann et al. 'Symmetry fingerprints of a benzene single-electron transistor: Interplay between Coulomb interaction and orbital symmetry'. In: *Phys. Rev. B* 77 (2008), 201406.

[100] D. Toroz, M. Rontani, and S. Corni. 'Visualizing electron correlation by means of ab initio scanning tunneling spectroscopy images of single molecules'. In: *J. Chem. Phys.* 134 (2011), 024104.

[101] D. Toroz, M. Rontani, and S. Corni. 'Proposed Alteration of Images of Molecular Orbitals Obtained Using a Scanning Tunneling Microscope as a Probe of Electron Correlation'. In: *Phys. Rev. Lett.* 110 (2013), 018305.

[102] F. Schulz et al. 'Many-body transitions in a single molecule visualized by scanning tunnelling microscopy'. In: *Nat. Phys.* 11 (2015), 229.

[103] B. Siegert, A. Donarini, and M. Grifoni. 'Nonequilibrium spin crossover in copper phthalocyanine'. In: *Phys. Rev. B* 93 (2016), 121406(R).

[104] M.-S. Liao and S. Scheiner. 'Electronic structure and bonding in metal phthalocyanines, metal= Fe, Co, Ni, Cu, Zn, Mg'. In: *J. Chem. Phys.* 114 (2001), 9780.

[105] K. A. Nguyen and R. Pachter. 'Jahn–Teller triplet excited state structures and spectra of zinc complexes of porphyrin and phthalocyanine: A density functional theory study'. In: *J. Chem. Phys.* 118 (2003), 5802.

[106] S. W. Wu, N. Ogawa, and W. Ho. 'Atomic-Scale Coupling of Photons to Single-Molecule Junctions'. In: *Science* 312 (2006), 1362.

[107] S. W. Wu et al. 'Conductance Hysteresis and Switching in a Single-Molecule Junction'. In: *J. Phys. Chem. C* 112 (2008), 5241.

[108] C. Uhlmann, I. Swart, and J. Repp. 'Controlling the Orbital Sequence in Individual Cu-Phthalocyanine Molecules'. In: *Nano Lett.* 13 (2013), 777.

[109] J. Repp, P. Liljeroth, and G. Meyer. 'Coherent electron-nuclear coupling in oligothiophene molecular wires'. In: *Nat. Phys.* 6 (2010), 975.

[110] E. Hückel. 'Quantentheoretische Beiträge zum Benzolproblem'. In: *Z. Phys. Chem.* 70 (1931), 204.

[111] W. Barford. *Electronic and optical properties of conjugated polymers*. Oxford University Press, 2013.

[112] F. E. Olsson et al. 'Scanning tunneling microscopy and spectroscopy of sodium-chloride overlayers on the stepped Cu(311) surface: Experimental and theoretical study'. In: *Phys. Rev. B* 71 (2005), 075419.

[113] J. M. Soler et al. 'The SIESTA method for ab initio order-N materials simulation'. In: *J. Phys. Condens. Matter.* 14 (2002), 2745.

[114] S. Koller et al. 'Density-operator approaches to transport through interacting quantum dots: Simplifications in fourth-order perturbation theory'. In: *Phys. Rev. B* 82 (2010), 235307.

[115] S. Sobczyk, A. Donarini, and M. Grifoni. 'Theory of STM junctions for π-conjugated molecules on thin insulating films'. In: *Phys. Rev. B* 85 (2012), 205408.

[116] R. Härtle et al. ‘Decoherence and lead-induced interdot coupling in nonequilibrium electron transport through interacting quantum dots: A hierarchical quantum master equation approach’. In: *Phys. Rev. B* 88 (2013), 235426.

[117] W. J. Feast et al. ‘Synthesis, processing and material properties of conjugated polymers’. In: *Polymer* 37 (1996), 5017.

[118] R. Yamada et al. ‘Electrical Conductance of Oligothiophene Molecular Wires’. In: *Nano Lett.* 8 (2008), 1237.

[119] R. Fitzner et al. ‘Dicyanovinyl–Substituted Oligothiophenes: Structure-Property Relationships and Application in Vacuum-Processed Small Molecule Organic Solar Cells’. In: *Adv. Funct. Mater.* 21 (2011), 897.

[120] D. A. Kislitsyn et al. ‘Oligothiophene wires: impact of torsional conformation on the electronic structure’. In: *Phys. Chem. Chem. Phys.* 18 (2016), 4842.

[121] J. Repp et al. ‘Molecules on Insulating Films: Scanning-Tunneling Microscopy Imaging of Individual Molecular Orbitals’. In: *Phys. Rev. Lett.* 94 (2005), 026803.

[122] F. E. Olsson et al. ‘Multiple Charge States of Ag Atoms on Ultrathin NaCl Films’. In: *Phys. Rev. Lett.* 98 (2007), 176803.

[123] I. Swart, T. Sonnleitner, and J. Repp. ‘Charge State Control of Molecules Reveals Modification of the Tunneling Barrier with Intramolecular Contrast’. In: *Nano Lett.* 11 (2011), 1580.

[124] L. Bogner et al. ‘Electronic structure and excited state dynamics in a dicyanovinyl-substituted oligothiophene on Au(111)’. In: *Phys. Chem. Chem. Phys.* 17 (2015), 27118.

[125] P. O. Gartland, S Berge, and B. J. Slagsvold. ‘Photoelectric Work Function of a Copper Single Crystal for the (100), (110), (111), and (112) Faces’. In: *Phys. Rev. Lett.* 28 (1972), 738.

[126] S. Sadewasser et al. 'New Insights on Atomic-Resolution Frequency-Modulation Kelvin-Probe Force-Microscopy Imaging of Semiconductors'. In: *Phys. Rev. Lett.* 103 (2009), 266103.

[127] F. Mohn et al. 'Imaging the charge distribution within a single molecule'. In: *Nat. Nanotechnol.* 7 (2012), 227.

[128] L. Gross et al. 'Measuring the Charge State of an Adatom with Noncontact Atomic Force Microscopy'. In: *Science* 324 (2009), 1428.

[129] T. Leoni et al. 'Controlling the Charge State of a Single Redox Molecular Switch'. In: *Phys. Rev. Lett.* 106 (2011), 216103.

[130] B. Schuler et al. 'Contrast Formation in Kelvin Probe Force Microscopy of Single π-Conjugated Molecules'. In: *Nano Lett.* 14 (2014), 3342.

[131] J. L. Neff and P. Rahe. 'Insights into Kelvin probe force microscopy data of insulator-supported molecules'. In: *Phys. Rev. B* 91 (2015), 085424.

[132] M. Ikeda et al. 'Work function on dye-adsorbed TiO_2 surfaces measured by using a Kelvin probe force microscope'. In: *J. Phys. Chem. C* 112 (2008), 6961.

[133] K. K. Gomes et al. 'Visualizing pair formation on the atomic scale in the high-T_c superconductor $Bi_2Sr_2CaCu_2O_{8+\delta}$'. In: *Nature* 447 (2007), 569.

[134] D. A. Ryndyk et al. 'Many-body localized molecular orbital approach to molecular transport'. In: *Phys. Rev. B* 88 (2013), 085404.

[135] K. Kaasbjerg and K. Flensberg. 'Strong Polarization-Induced Reduction of Addition Energies in Single-Molecule Nanojunctions'. In: *Nano Lett.* 8 (2008), 3809.

[136] K. Kaasbjerg and K. Flensberg. 'Image charge effects in single-molecule junctions: Breaking of symmetries and negative-differential resistance in a benzene single-electron transistor'. In: *Phys. Rev. B* 84 (2011), 115457.

[137] L. P. Kouwenhoven et al. 'Electron transport in quantum dots'. In: *Mesoscopic Electron Transport*. Springer, 1997, 105.

[138] L. P. Kouwenhoven et al. 'Single electron charging effects in semiconductor quantum dots'. In: *Z. Phys. B* 85 (1991), 367.

[139] F. R. Waugh et al. 'Single-Electron Charging in Double and Triple Quantum Dots with Tunable Coupling'. In: *Phys. Rev. Lett.* 75 (1995), 705.

[140] M. P. V. Kouwen et al. 'Single Electron Charging in Optically Active Nanowire Quantum Dots'. In: *Nano Lett.* 10 (2010), 1817.

[141] J. Park et al. 'Coulomb blockade and the Kondo effect in single-atom transistors'. In: *Nature* 417 (2002), 722.

[142] W. Liang et al. 'Kondo resonance in a single-molecule transistor'. In: *Nature* 417 (2002), 725.

[143] S. Kubatkin et al. 'Single-electron transistor of a single organic molecule with access to several redox states'. In: *Nature* 425 (2003), 698.

[144] J. Repp et al. 'Controlling the Charge State of Individual Gold Adatoms'. In: *Science* 305 (2004), 493.

[145] S. Wu, N. Ogawa, and W. Ho. 'Atomic-scale coupling of photons to single-molecule junctions'. In: *Science* 312 (2006), 1362.

[146] I. Fernández-Torrente, K. J. Franke, and J. I. Pascual. 'Vibrational Kondo Effect in Pure Organic Charge-Transfer Assemblies'. In: *Phys. Rev. Lett.* 101 (2008), 217203.

[147] B. Zaknoon et al. 'Study of Single Silicon Quantum Dots' Band Gap and Single-Electron Charging Energies by Room Temperature Scanning Tunneling Microscopy'. In: *Nano Lett.* 8 (2008), 1689.

[148] M. R. Hummon et al. 'Measuring charge trap occupation and energy level in CdSe/ZnS quantum dots using a scanning tunneling microscope'. In: *Phys. Rev. B* 81 (2010), 115439.

[149] G. V. Nazin, X. H. Qiu, and W. Ho. 'Charging and Interaction of Individual Impurities in a Monolayer Organic Crystal'. In: *Phys. Rev. Lett.* 95 (2005), 166103.

[150] I. Fernández-Torrente et al. 'Gating the Charge State of Single Molecules by Local Electric Fields'. In: *Phys. Rev. Lett.* 108 (2012), 036801.

[151] M. T. Woodside and P. L. McEuen. 'Scanned probe imaging of single-electron charge states in nanotube quantum dots'. In: *Science* 296 (2002), 1098.

[152] C. Schönenberger and S. F. Alvarado. 'Observation of single charge carriers by force microscopy'. In: *Phys. Rev. Lett.* 65 (1990), 3162.

[153] L. J. Klein and C. C. Williams. 'Single electron tunneling detected by electrostatic force'. In: *Appl. Phys. Lett.* 79 (2001), 1828.

[154] E. B. Bussmann, N. Zheng, and C. C. Williams. 'Imaging of Localized Electronic States at a Nonconducting Surface by Single-Electron Tunneling Force Microscopy'. In: *Nano Lett.* 6 (2006), 2577.

[155] R. Stomp et al. 'Detection of Single-Electron Charging in an Individual InAs Quantum Dot by Noncontact Atomic-Force Microscopy'. In: *Phys. Rev. Lett.* 94 (2005), 056802.

[156] J. Zhu, M. Brink, and P. L. McEuen. 'Frequency shift imaging of quantum dots with single-electron resolution'. In: *Appl. Phys. Lett.* 87 (2005), 242102.

[157] Y. Azuma et al. 'Single Electron on a Nanodot in a Double-Barrier Tunneling Structure Observed by Noncontact Atomic-Force Spectroscopy'. In: *Phys. Rev. Lett.* 96 (2006), 016108.

[158] C. Lotze. 'Fundamental Processes in Single Molecule Junctions'. PhD thesis. Freie Universität Berlin, 2013.

[159] S. D. Bennett et al. 'Strong Electromechanical Coupling of an Atomic Force Microscope Cantilever to a Quantum Dot'. In: *Phys. Rev. Lett.* 104 (2010), 017203.

[160] L. Cockins et al. 'Excited-State Spectroscopy on an Individual Quantum Dot Using Atomic Force Microscopy'. In: *Nano Lett.* 12 (2012), 709.

[161] A. Roy-Gobeil, Y. Miyahara, and P. Grütter. 'Revealing Energy Level Structure of Individual Quantum Dots by Tunneling Rate Measured by Single-Electron Sensitive Electrostatic Force Spectroscopy'. In: *Nano Lett.* 15 (2015), 2324.

[162] T. Brietzke et al. 'Mono-and dinuclear ruthenium(II) 1, 6, 7, 12-tetraazaperylene complexes'. In: *Dalton Trans.* 41 (2012), 2788.

[163] N. A. Pradhan et al. 'Atomic Scale Conductance Induced by Single Impurity Charging'. In: *Phys. Rev. Lett.* 94 (2005), 076801.

[164] K. Teichmann et al. 'Controlled Charge Switching on a Single Donor with a Scanning Tunneling Microscope'. In: *Phys. Rev. Lett.* 101 (2008), 076103.

[165] V. W. Brar et al. 'Gate-controlled ionization and screening of cobalt adatoms on a graphene surface'. In: *Nat. Phys.* 7 (2011), 43.

[166] T. König et al. 'Measuring the charge state of point defects on MgO/Ag(001)'. In: *J. Am. Chem. Soc.* 131 (2009), 17544.

[167] F. J. Giessibl. 'A direct method to calculate tip–sample forces from frequency shifts in frequency-modulation atomic force microscopy'. In: *Appl. Phys. Lett.* 78 (2001), 123.

[168] R. Gurney. 'Theory of electrical double layers in adsorbed films'. In: *Phys. Rev.* 47 (1935), 479.

[169] P. W. Anderson. 'Localized magnetic states in metals'. In: *Phys. Rev.* 124 (1961), 41.

[170] D. M. Newns. 'Self-consistent model of hydrogen chemisorption'. In: *Phys. Rev.* 178 (1969), 1123.

[171] T. Grimley. 'The indirect interaction between atoms or molecules adsorbed on metals'. In: *Proc. Phys. Soc. (London)* 90 (1967), 751.

[172] T. Grimley. 'The electron density in a metal near a chemisorbed atom or molecule'. In: *Proc. Phys. Soc. (London)* 92 (1967), 776.

[173] A. Zangwill. *Physics at Surface*. Cambridge University Press, 1988.

[174] A. Gross. *Theoretical Surface Science*. Vol. 1. Springer, 2014.

[175] A. Tekiel et al. 'Room-Temperature Single-Electron Charging Detected by Electrostatic Force Microscopy'. In: *ACS Nano* 7 (2013), 4683.

[176] N. Sasaki and M. Tsukada. 'Effect of microscopic nonconservative process on noncontact atomic force microscopy'. In: *Jpn. J. of Appl. Phys.* 39 (2000), L1334.

[177] L. N. Kantorovich and T. Trevethan. 'General Theory of Microscopic Dynamical Response in Surface Probe Microscopy: From Imaging to Dissipation'. In: *Phys. Rev. Lett.* 93 (2004), 236102.

[178] J. Zhu, M. Brink, and P. L. McEuen. 'Single-Electron Force Readout of Nanoparticle Electrometers Attached to Carbon Nanotubes'. In: *Nano Lett.* 8 (2008), 2399.

[179] L. Cockins et al. ‘Energy levels of few-electron quantum dots imaged and characterized by atomic force microscopy’. In: *PNAS* 107 (2010), 9496.

[180] L. Gross et al. ‘Bond-Order Discrimination by Atomic Force Microscopy’. In: *Science* 337 (2012), 1326.

[181] S. W. Wu et al. ‘Control of Relative Tunneling Rates in Single Molecule Bipolar Electron Transport’. In: *Phys. Rev. Lett.* 93 (2004), 236802.

[182] N. Kocić et al. ‘Periodic Charging of Individual Molecules Coupled to the Motion of an Atomic Force Microscopy Tip’. In: *Nano Lett.* 15 (2015), 4406.

[183] L. Liu et al. ‘Interplay between Energy-Level Position and Charging Effect of Manganese Phthalocyanines on an Atomically Thin Insulator’. In: *ACS Nano* 9 (2015), 10125.

[184] C. Wagner et al. ‘Scanning Quantum Dot Microscopy’. In: *Phys. Rev. Lett.* 115 (2015), 026101.

[185] K. D. Bonin and V. V. Kresin. *Electric-dipole Polarizabilities of Atoms, Molecules, and Clusters*. World Scientific, Singapore, 1997.

[186] R. Hesper, L. Tjeng, and G. Sawatzky. ‘Strongly reduced band gap in a correlated insulator in close proximity to a metal’. In: *EPL* 40 (1997), 177.

[187] G. A. Steele et al. ‘Strong coupling between single-electron tunneling and nanomechanical motion’. In: *Science* 325 (2009), 1103.

[188] F. Santandrea et al. ‘Cooling of nanomechanical resonators by thermally activated single-electron transport’. In: *Phys. Rev. Lett.* 106 (2011), 186803.

[189] M. Gardner. ‘Mathematical games: The fantastic combinations of John Conway’s new solitaire game "life"’. In: *SciAm* 223 (1970), 120.

[190] G. Grössing and A. Zeilinger. 'Quantum cellular automata'. In: *Complex Systems* 2 (1988), 197.

[191] R. P. Feynman. 'Simulating physics with computers'. In: *Int. J. Theor. Phys.* 21 (1982), 467.

[192] J. Watrous. 'On One-Dimensional Quantum Cellular Automata'. In: *Foundations of Computer Science, 1995. Proceedings., 36th Annual Symposium on*. IEEE. 1995, 528.

[193] C. S. Lent et al. 'Quantum cellular automata'. In: *Nanotechnology* 4 (1993), 49.

[194] C. S. Lent and P. D. Tougaw. 'A device architecture for computing with quantum dots'. In: *Proc. IEEE* 85 (1997), 541.

[195] A. Orlov et al. 'Realization of a functional cell for quantum-dot cellular automata'. In: *Science* 277 (1997), 928.

[196] I. Amlani et al. 'Digital logic gate using quantum-dot cellular automata'. In: *Science* 284 (1999), 289.

[197] R. K. Kummamuru et al. 'Operation of a quantum-dot cellular automata (QCA) shift register and analysis of errors'. In: *IEEE Trans. Electron. Dev.* 50 (2003), 1906.

[198] R. P. Cowburn and M. E. Welland. 'Room Temperature Magnetic Quantum Cellular Automata'. In: *Science* 287 (2000), 1466.

[199] A. Imre et al. 'Majority Logic Gate for Magnetic Quantum-Dot Cellular Automata'. In: *Science* 311 (2006), 205.

[200] R. A. Wolkow et al. 'Silicon atomic quantum dots enable beyond-cmos electronics'. In: *Field-Coupled Nanocomputing: Paradigms, Progress, and Perspectives*. Springer, 2014, 33.

[201] W. G. Van der Wiel et al. 'Electron transport through double quantum dots'. In: *Rev. Mod. Phys.* 75 (2002), 1.

[202] T. Hayashi et al. 'Coherent manipulation of electronic states in a double quantum dot'. In: *Phys. Rev. Lett.* 91 (2003), 226804.

[203] J. R. Petta et al. ‘Manipulation of a single charge in a double quantum dot’. In: *Phys. Rev. Lett.* 93 (2004), 186802.

[204] D. P. DiVincenzo. ‘Double Quantum Dot as a Quantum Bit’. In: *Science* 309 (2005), 2173.

[205] L. Gaudreau et al. ‘Stability Diagram of a Few-Electron Triple Dot’. In: *Phys. Rev. Lett.* 97 (2006), 036807.

[206] R. Hanson et al. ‘Spins in few-electron quantum dots’. In: *Rev. Mod. Phys.* 79 (2007), 1217.

[207] F. Marczinowski et al. ‘Effect of charge manipulation on scanning tunneling spectra of single Mn acceptors in InAs’. In: *Phys. Rev. B* 77 (2008), 115318.

[208] K. Teichmann et al. ‘Bistable Charge Configuration of Donor Systems near the GaAs(110) Surfaces’. In: *Nano Lett.* 11 (2011), 3538.

[209] J. Martínez-Blanco et al. ‘Gating a single-molecule transistor with individual atoms’. In: *Nat. Phys.* 11 (2015), 640.

[210] P. Liljeroth, J. Repp, and G. Meyer. ‘Current-induced hydrogen tautomerization and conductance switching of naphthalocyanine molecules’. In: *Science* 317 (2007), 1203.

[211] R. Ohmann, L. Vitali, and K. Kern. ‘Actuated transitory metal-ligand bond as tunable electromechanical switch’. In: *Nano Lett.* 10 (2010), 2995.

[212] W. Auwärter et al. ‘A surface-anchored molecular four-level conductance switch based on single proton transfer’. In: *Nat. Nanotechnol.* 7 (2012), 41.

[213] X. H. Qiu, G. V. Nazin, and W Ho. ‘Mechanisms of reversible conformational transitions in a single molecule’. In: *Phys. Rev. Lett.* 93 (2004), 196806.

[214] M. Alemani et al. ‘Electric Field-Induced Isomerization of Azobenzene by STM’. In: *J. Am. Chem. Soc.* 128 (2006), 14446.

[215] M. J. Comstock et al. 'Determination of Photoswitching Dynamics through Chiral Mapping of Single Molecules Using a Scanning Tunneling Microscope'. In: *Phys. Rev. Lett.* 104 (2010), 178301.

[216] F. Moresco et al. 'Conformational Changes of Single Molecules Induced by Scanning Tunneling Microscopy Manipulation: A Route to Molecular Switching'. In: *Phys. Rev. Lett.* 86 (2001), 672.

[217] S. Yamazaki et al. 'Interplay between Switching Driven by the Tunneling Current and Atomic Force of a Bistable Four-Atom Si Quantum Dot'. In: *Nano Lett.* 15 (2015), 4356.

[218] B.-Y. Choi et al. 'Conformational Molecular Switch of the Azobenzene Molecule: A Scanning Tunneling Microscopy Study'. In: *Phys. Rev. Lett.* 96 (2006), 156106.

[219] T. G. Gopakumar et al. 'Electron-Induced Spin Crossover of Single Molecules in a Bilayer on Gold'. In: *Angew. Chem. Int. Ed.* 51 (2012), 6262.

[220] M. Lastapis et al. 'Picometer-Scale Electronic Control of Molecular Dynamics Inside a Single Molecule'. In: *Science* 308 (2005), 1000.

[221] F. Mohn et al. 'Reversible Bond Formation in a Gold–Atom—Organic–Molecule Complex as a Molecular Switch'. In: *Phys. Rev. Lett.* 105 (2010), 266102.

[222] Y. Wang et al. 'Pushing and Pulling a Sn Ion through an Adsorbed Phthalocyanine Molecule'. In: *J. Am. Chem. Soc.* 131 (2009), 3639.

[223] H. Zhang et al. 'Surface Supported Gold–Organic Hybrids: On-Surface Synthesis and Surface Directed Orientation'. In: *Small* 10 (2014), 1361.

[224] M. J. Comstock et al. 'Reversible Photomechanical Switching of Individual Engineered Molecules at a Surface'. In: *Phys. Rev. Lett.* 99 (2007), 038301.

[225] Y. B. Kim et al. 'Molecular Seesaw: A Three-Way Motion and Motion-Induced Surface Modification'. In: *J. Am. Chem. Soc.* 132 (2010), 12782.

[226] S. Hagen et al. 'Excitation mechanism in the photoisomerization of a surface-bound azobenzene derivative: Role of the metallic substrate'. In: *J. Chem. Phys.* 129 (2008), 164102.

[227] J. Schütte et al. 'Single-molecule switching with non-contact atomic force microscopy'. In: *Nanotechnology* 22 (2011), 245701.

[228] C. Nacci et al. 'Conformational switching of single 1,5- cyclooctadiene molecules on Si(001) induced by inelastic electron tunneling'. In: *Phys. Rev. B* 77 (2008), 121405.

[229] J. L. Pitters and R. A. Wolkow. 'Detailed Studies of Molecular Conductance Using Atomic Resolution Scanning Tunneling Microscopy'. In: *Nano Lett.* 6 (2006), 390.

[230] C. Nacci et al. 'Controlled Switching within an Organic Molecule Deliberately Pinned to a Semiconductor Surface'. In: *ACS Nano* 6 (2012), 4190.

[231] S. Godlewski et al. 'Single-Molecule Rotational Switch on a Dangling Bond Dimer Bearing'. In: *ACS Nano* 10 (2016), 8499.

[232] R. Raval. 'Chiral expression from molecular assemblies at metal surfaces: insights from surface science techniques'. In: *Chem. Soc. Rev.* 38 (2009), 707.

[233] J. Repp et al. 'Ionic films on vicinal metal surfaces: enhanced binding due to charge modulation'. In: *Phys. Rev. Lett.* 86 (2001), 252.

[234] L. Gross et al. 'Organic structure determination using atomic-resolution scanning probe microscopy'. In: *Nat. Chem.* 2 (2010), 821.

[235] N. Pavliček et al. 'Atomic Force Microscopy Reveals Bistable Configurations of Dibenzo[a,h]thianthrene and their Interconversion Pathway'. In: *Phys. Rev. Lett.* 108 (2012), 086101.

[236] T. Sonnleitner et al. 'Molecular Symmetry Governs Surface Diffusion'. In: *Phys. Rev. Lett.* 107 (2011), 186103.

[237] B. Schuler et al. 'Adsorption Geometry Determination of Single Molecules by Atomic Force Microscopy'. In: *Phys. Rev. Lett.* 111 (2013), 106103.

[238] N. J. van der Heijden et al. 'Characteristic Contrast in Δf_{min} Maps of Organic Molecules Using Atomic Force Microscopy'. In: *ACS Nano* 10 (2016), 8517.

[239] W. Steurer et al. 'Toggling the Local Electric Field with an Embedded Adatom Switch'. In: *Nano Lett.* 15 (2015), 5564.

[240] P. Saalfrank. 'Manipulation of adsorbates with electric fields'. In: *J. Chem. Phys.* 113 (2000), 3780.

[241] C. Bolm. 'Cross-Coupling Reactions'. In: *Org. Lett.* 14 (2012), 2925.

[242] P. Rempala, J. Kroulík, and B. T. King. 'Investigation of the Mechanism of the Intramolecular Scholl Reaction of Contiguous Phenylbenzenes'. In: *J. Org. Chem.* 71 (2006), 5067.

[243] J. J. Li. *Name Reactions: A Collection of Detailed Reaction Mechanism.* 2^{nd} ed.; Springer-Verlag: New York, 2003.

[244] A. T. Balaban and C. D. Nenitzescu. *Dehydrogenating Condensations of Aromatics (Scholl and Related reactions).* Vol. 2. Olah, G., Ed.; Wiley: New York, 1964, 979.

[245] B. T. King et al. 'Controlling the Scholl reaction'. In: *J. Org. Chem.* 72 (2007), 2279.

[246] C. D. Simpson et al. 'Synthesis of a Giant 222 Carbon Graphite Sheet'. In: *Chem. Eur. J.* 8 (2002), 1424.

[247] C. D. Simpson et al. 'Nanosized Molecular Propellers by Cyclodehydrogenation of Polyphenylene Dendrimers'. In: *J. Am. Chem. Soc.* 126 (2004), 3139.

[248] J. Wu, W. Pisula, and K. Müllen. 'Graphenes as potential material for electronics'. In: *Chem. Rev.* 107 (2007), 718.

[249] A. Narita et al. 'New advances in nanographene chemistry'. In: *Chem. Soc. Rev.* 44 (2015), 6616.

[250] M. Grzybowski et al. 'Comparison of Oxidative Aromatic Coupling and the Scholl Reaction'. In: *Angew. Chem. Int. Ed.* 52 (2013), 9900.

[251] D. J. Gregg et al. 'Extending the Nitrogen-Heterosuperbenzene Family: The Spectroscopic, Redox, and Photophysical Properties of "Half-Cyclized" N-1/2HSB and Its Ru(II) Complex'. In: *Inorg. Chem.* 44 (2005), 5654.

[252] L. P. Wijesinghe et al. 'Methoxy functionalisation: exerting synthetic control of the supramolecular and electronic structure of nitrogen-doped nanographenes'. In: *Chem. Commun.* 50 (2014), 10637.

[253] T. H. Vo et al. 'Bottom-up solution synthesis of narrow nitrogen-doped graphene nanoribbons'. In: *Chem. Commun.* 50 (2014), 4172.

[254] J. Méndez, M. F. López, and J. A. Martín-Gago. 'On-surface synthesis of cyclic organic molecules'. In: *Chem. Soc. Rev* 40 (2011), 4578.

[255] G. Franc and A. Gourdon. 'Covalent networks through on-surface chemistry in ultra-high vacuum: state-of-the-art and recent developments'. In: *Phys. Chem. Chem. Phys.* 13 (2011), 14283.

[256] M. El Garah, J. M. MacLeod, and F. Rosei. 'Covalently bonded networks through surface-confined polymerization'. In: *Surf. Sci.* 613 (2013), 6.

[257] A. Wiengarten et al. 'Surface-assisted Dehydrogenative Homocoupling of Porphine Molecules'. In: *J. Am. Chem. Soc.* 136 (2014), 9346.

[258] Q. Sun et al. 'On-surface formation of two-dimensional polymer via direct C–H activation of metal phthalocyanine'. In: *Chem. Commun.* 51 (2015), 2836.

[259] L. Dong, P. N. Liu, and N. Lin. 'Surface-Activated Coupling Reactions Confined on a Surface'. In: *Acc. Chem. Res.* 48 (2015), 2765.

[260] Q. Fan, J. M. Gottfried, and J. Zhu. 'Surface-Catalyzed C–C Covalent Coupling Strategies toward the Synthesis of Low-Dimensional Carbon-Based Nanostructures'. In: *Acc. Chem. Res.* 48 (2015), 2484.

[261] J. Cai et al. 'Atomically precise bottom-up fabrication of graphene nanoribbons'. In: *Nature* 466 (2010), 470.

[262] S. Blankenburg et al. 'Intraribbon Heterojunction Formation in Ultranarrow Graphene Nanoribbons'. In: *ACS Nano* 6 (2012), 2020.

[263] H. Huang et al. 'Spatially Resolved Electronic Structures of Atomically Precise Armchair Graphene Nanoribbons'. In: *Sci. Rep.* 2 (2012), 983.

[264] T. Dienel et al. 'Resolving Atomic Connectivity in Graphene Nanostructure Junctions'. In: *Nano Lett.* 15 (2015), 5185.

[265] Y.-C. Chen et al. 'Molecular bandgap engineering of bottom-up synthesized graphene nanoribbon heterojunctions'. In: *Nat. Chem.* 10 (2015), 156.

[266] J. Liu et al. 'Towards Cove-Edged Low Band Gap Graphene Nanoribbons'. In: *J. Am. Chem. Soc.* 137 (2015), 6097.

[267] A. L. Pinardi et al. 'Tailored Formation of N-Doped Nanoarchitectures by Diffusion-Controlled on-Surface (Cyclo)Dehydrogenation of Heteroaromatics'. In: *ACS Nano* 7 (2013), 3676.

[268] A. L. Pinardi et al. 'Sequential formation of N-doped nanohelicenes, nanographenes and nanodomes by surface-assisted chemical (cyclo)dehydrogenation of heteroaromatics'. In: *Chem. Commun.* 50 (2014), 1555.

[269] L. Liang and V. Meunier. 'Atomically Precise Graphene Nanoribbon Heterojunctions for Excitonic Solar Cells'. In: *J. Phys. Chem. C* 119 (2015), 775.

[270] T. Dienel et al. 'Dehalogenation and Coupling of a Polycyclic Hydrocarbon on an Atomically Thin Insulator'. In: *ACS Nano* 8 (2014), 6571.

[271] D. Usachov et al. 'Nitrogen-Doped Graphene: Efficient Growth, Structure, and Electronic Properties'. In: *Nano Lett.* 11 (2011), 5401.

[272] C. Bronner et al. 'Aligning the Band Gap of Graphene Nanoribbons by Monomer Doping'. In: *Angew. Chem. Int. Ed.* 52 (2013), 4422.

[273] A. Wiengarten et al. 'Surface-Assisted Cyclodehydrogenation; Break the Symmetry, Enhance the Selectivity'. In: *Chem. Eur. J.* 21 (2015), 12285.

[274] G. A. Somorjai and J. Y. Park. 'Molecular factors of catalytic selectivity'. In: *Angew. Chem. Int. Ed.* 47 (2008), 9212.

[275] Q. Sun et al. 'On-surface aryl–aryl coupling via selective C–H activation'. In: *Chem. Commun.* 50 (2014), 11825.

[276] J. M. Gottfried. 'Surface chemistry of porphyrins and phthalocyanines'. In: *Surf. Sci. Rep.* 70 (2015), 259.

[277] L. Lafferentz et al. 'Controlling on-surface polymerization by hierarchical and substrate-directed growth'. In: *Nat. Chem.* 4 (2012), 215.

[278] J. Björk, S. Stafström, and F. Hanke. 'Zipping Up: Cooperativity Drives the Synthesis of Graphene Nanoribbons'. In: *J. Am. Chem. Soc.* 133 (2011), 14884.

[279] K. Ø. Hanssen et al. 'A Combined Atomic Force Microscopy and Computational Approach for the Structural Elucidation of Breitfussin A and B: Highly Modified Halogenated Dipeptides from Thuiaria breitfussi'. In: *Angew. Chem. Int. Ed.* 124 (2012), 12238.

[280] F. Albrecht et al. 'Formation and Characterization of a Molecule–Metal–Molecule Bridge in Real Space'. In: *J. Am. Chem. Soc.* 135 (2013), 9200.

[281] F. Albrecht et al. 'Characterization of a Surface Reaction by means of Atomic Force Microscopy'. In: *J. Am. Chem. Soc.* 137 (2015), 7424.

[282] A. Riss et al. 'Local Electronic and Chemical Structure of Oligo-Acetylene Derivatives Formed Through Radical Cyclizations at a Surface'. In: *Nano Lett.* 14 (2014).

[283] S.-W. Hla et al. 'Inducing All Steps of a Chemical Reaction with the Scanning Tunneling Microscope Tip: Towards Single Molecule Engineering'. In: *Phys. Rev. Lett.* 85 (2000), 2777.

[284] D. G. de Oteyza et al. 'Direct Imaging of Covalent Bond Structure in Single-Molecule Chemical Reactions'. In: *Science* 340 (2013), 1434.

[285] J. Bergkamp, S. Decurtins, and S.-X. Liu. 'Current advances in fused tetrathiafulvalene donor–acceptor systems'. In: *Chem. Soc. Rev.* 44 (2015), 863.

[286] B. Liu et al. 'A Scanning Probe Microscopy Study of Annulated Redox-Active Molecules at a Liquid/Solid Interface: The Overruling of the Alkyl Chain Paradigm'. In: *Chem. Eur. J.* 16 (2010), 5008.

[287] C. Jia et al. 'A redox-active tri-star molecule: merging of TTF and HAT chemistry'. In: *Chem. Commun.* 17 (2006), 1878.

[288] J. Wu et al. 'Imidazole-Annulated Tetrathiafulvalenes Exhibiting pH-Tuneable Intramolecular Charge Transfer and Redox Properties'. In: *Chem. Asian J.* 4 (2009), 392.

[289] C. Abeywickrama and A. D. Baker. 'Efficient Synthesis of 1,4,5,-12-Tetraazatriphenylene and Derivatives'. In: *J. Org. Chem.* 69 (2004), 7741.

[290] Y. Fuchs et al. 'Spectroscopic and electrochemical properties of dimeric Ruthenium(II)diimine complexes and determination of their excited state redox properties'. In: *J. Am. Chem. Soc.* 109 (1987), 2691.

[291] H. Grove et al. 'Syntheses, crystal structures and magnetic properties of one- and two-dimensional pap-containing copper(II) complexes (pap = pyrazino[2,3- *f*][4,7] phenanthroline)'. In: *J. Chem. Soc., Dalton Trans.* (2001), 259.

[292] H. Grove and J. Sletten. 'Crystal structures of 4,7-phenanthrolino-5,6:5,6'-pyrazine tetrahydrate and 1,4,5,8,9,12-hexaazatriphenylene dihydrate'. In: *J. Chem. Crystallogr.* 30 (2000), 123.

[293] I. González et al. 'A comparative study of Ir(III) complexes with pyrazino[2,3-*f*][1,10]phenanthroline and pyrazino[2,3-*f*]-[4,7]phenanthroline ligands in light-emitting electrochemical cells (LECs)'. In: *Dalton Trans.* 44 (2015), 14771.

[294] V. Blum et al. 'Ab initio molecular simulations with numeric atom-centered orbitals'. In: *Comput. Phys. Commun.* 180 (2009), 2175.

[295] A. Tkatchenko and M. Scheffler. 'Accurate Molecular Van Der Waals Interactions from Ground-State Electron Density and Free-Atom Reference Data'. In: *Phys. Rev. Lett.* 102 (2009), 073005.

[296] P. Hapala et al. 'Mechanism of high-resolution STM/AFM imaging with functionalized tips'. In: *Phys. Rev. B* 90 (2014), 085421.

[297] P. Hapala et al. 'Origin of High-Resolution IETS-STM Images of Organic Molecules with Functionalized Tips'. In: *Phys. Rev. Lett.* 113 (2014), 226101.

[298] S. Kawai et al. 'Atomically controlled substitutional boron-doping of graphene nanoribbons'. In: *Nat. Commun.* 6 (2015), 8098.

[299] N. Moll et al. 'Image Distortions of a Partially Fluorinated Hydrocarbon Molecule in Atomic Force Microscopy with Carbon Monoxide Terminated Tips'. In: *Nano Lett.* 14 (2014), 6127.

[300] Z. Shi and N. Lin. 'Porphyrin-Based Two-Dimensional Coordination Kagome Lattice Self-Assembled on a Au(111) Surface'. In: *J. Am. Chem. Soc.* 131 (2009), 5376.

[301] P. Maksymovych, D. C. Sorescu, and J. T. Yates Jr. 'Gold-Adatom-Mediated Bonding in Self-Assembled Short-Chain Alkanethiolate Species on the Au(111) Surface'. In: *Phys. Rev. Lett.* 97 (2006), 146103.

[302] S. Stepanow et al. 'Surface-Assisted Assembly of 2D Metal–Organic Networks That Exhibit Unusual Threefold Coordination Symmetry'. In: *Angew. Chem. Int. Ed.* 119 (2007), 724.

[303] G. Pawin et al. 'A Surface Coordination Network Based on Substrate-Derived Metal Adatoms with Local Charge Excess'. In: *Angew. Chem. Int. Ed.* 47 (2008), 8442.

[304] J. Mielke et al. 'Adatoms underneath Single Porphyrin Molecules on Au(111)'. In: *J. Am. Chem. Soc* 137 (2015), 1844.

[305] Z. Yang et al. 'Orbital Redistribution in Molecular Nanostructures Mediated by Metal–Organic Bonds'. In: *ACS Nano* 8 (2014), 10715.

[306] S. K. Hämäläinen et al. 'Intermolecular Contrast in Atomic Force Microscopy Images without Intermolecular Bonds'. In: *Phys. Rev. Lett.* 113 (2014), 186102.

[307] J. van der Lit et al. 'Submolecular Resolution Imaging of Molecules by Atomic Force Microscopy: The Influence of the Electrostatic Force'. In: *Phys. Rev. Lett.* 116 (2016), 096102.

[308] Y.-F. Ran et al. 'Exploratory studies on coordination chemistry of a redox-active bridging ligand: synthesis, properties and solid state structures of the complexes'. In: *Dalton Trans.* 40 (2011), 8193.

[309] A. M. Sweetman et al. 'Mapping the force field of a hydrogen-bonded assembly'. In: *Nat. Commun.* 5 (2014), 3931.

[310] N. Pavliček et al. 'High-resolution scanning tunneling and atomic force microscopy of stereochemically resolved dibenzo[a,h]thianthrene molecules'. In: *phys. stat. sol. (b)* 250 (2013), 2424.

Acknowledgements

I am indebted to many people for their help and encouragement during my research program.

I would like to express my sincere gratitude to my supervisor, Prof. Dr. Jascha Repp, for the opportunity to perform this thesis in his group and his outstanding support and guidance. He allowed me the freedom to pursue my own scientific interests, always offering his help and expertise to learn from along the way. I thank him for critical evaluation of the theoretical and experimental procedures and our publications.

Prof. Dr. Christian Schüller has my gratitude as a co-referee of this thesis.

I would like to thank my former and present office and lab mates as well as other colleagues at University of Regensburg for all the discussions, help, and a great atmosphere. In particular, I want to thank Dr. Gerhard Münnich, Dr. Florian Albrecht, Dr. David Gohlke, Tobias Preis, Philipp Scheuerer and Fabian Queck.

Many thanks to Eng. Andreas Pöllmann for the technical support.

Special thanks go to Prof. Dr. Silvio Decurtins and his group at University of Bern with whom we had a fruitful collaboration; Dr. Shi-Xia Liu, Xunshan Liu, Stephan Keller and Songjie Chen for the creative supply of molecules. I thank them for their enthusiasm and willingness to share their knowledge.

I would like to thank Dr. Pavel Jelínek and Ondřej Krejčí from the Institute of Physics of the Czech Academy of Science, Prague, for being eager to complement our work on regioselectivity from the theory side.

Many thanks to Dr. Andrea Donarini and Dr. Benjamin Siegert for their theoretical support on our work on oligothiphene molecules. I thank Dr. Ping Yu and David Kasipović for a collaboration on the same project.

I owe thanks to Dr. Nicolas Lorente and Dr. Paula Abufager for performing DFT calculations of molecular islands and vacancies.

I am grateful to Prof. Dr. J. M. van Ruitenbeek and Saša Vrbica from the Leiden University for proposing the electromigration experiment.

This work was possible due to financial support by the German Research Foundation (DFG) through the projects of RTG 1570 and SFB 689.